

**FACULTY
OF MATHEMATICS
AND PHYSICS**
Charles University

DOCTORAL THESIS

Kristina Vlášková

**Magnetic properties of rare-earth
 $A_2\text{Ir}_2\text{O}_7$ pyrochlore iridates**

Department of Condensed Matter Physics

Supervisor of the doctoral thesis: RNDr. Milan Klicpera, Ph.D.

Study programme: Physics of Condensed Matter and
Materials Research

Study branch: P4F3

Prague 2022

I declare that I carried out this doctoral thesis independently, and only with the cited sources, literature and other professional sources. It has not been used to obtain another or the same degree.

I understand that my work relates to the rights and obligations under the Act No. 121/2000 Sb., the Copyright Act, as amended, in particular the fact that the Charles University has the right to conclude a license agreement on the use of this work as a school work pursuant to Section 60 subsection 1 of the Copyright Act.

In date

Author's signature

At this point, I want to thank the people who helped and supported me during my doctoral study. First, I would like to express my gratitude to my supervisor, RNDr. Milan Klicpera, Ph.D., for all his supervision, continuous support and patient guidance during my work. Sincere thanks belongs also to Dr. Ross Harvey Colman for inspiring discussions, help with advanced experiments and fresh insight into the problematics. I also wish to thank to prof. Mgr. Pavel Javorský, Dr and prof. RNDr. Vladimír Sechovský, DrSc. for motivation and support during my study.

During my work in the lab Mgr. Petr Proschek, Ing. Barbora Vondráčková, Ing. Martin Žáček, RNDr. Jan Prokleška, Ph.D. and RNDr. Jiří Pospíšil, Ph.D., were always willing to help me and answer my questions. Special thanks belong to doc. RNDr Martin Diviš, CSc., for his theoretical calculations. I gratefully acknowledge my colleagues Mgr. Jiří Volný and RNDr. Petr Doležal, Ph.D. for whom none of my problems were too minor.

Finally, this work could not have come into being without the support of my family and friends, who have supported me in every conceivable way.

Title: Magnetic properties of rare-earth $A_2\text{Ir}_2\text{O}_7$ pyrochlore iridates

Author: Kristina Vlášková

Department: Department of Condensed Matter Physics

Supervisor: RNDr. Milan Klicpera, Ph.D., Department of Condensed Matter Physics

Abstract: The present thesis is focused on the synthesis, characterisation and magnetic properties of $A_2\text{Ir}_2\text{O}_7$ pyrochlore iridates with A standing for Dy - Lu. The geometrically frustrated pyrochlore lattice affects the interactions between magnetic moments of both A^{3+} and Ir^{4+} , frequently leading to complex low-temperature states. Moreover, an interplay between spin-orbit coupling and electron correlations, inherent to iridium ions, has been proposed/observed to significantly affect the conductive properties of pyrochlores. The $A_2\text{Ir}_2\text{O}_7$ iridates were synthesized, and respective synthesis routes optimized, by CsCl flux method. Thoroughly characterised samples, including previously unprepared $A = \text{Tm}$ analogue, were investigated by means of standard bulk methods, as well as techniques of neutron scattering and muon spin resonance. An evolution of magnetic ordering of the iridium sublattice was followed for heavy rare-earth part of the series, allowing to finalize the respective phase diagram. An emergence of oscillations in muon spin rotation spectra unambiguously proved the existence of long-range iridium ordering in studied members. The dynamical AC susceptibility response was discussed in the frame of the model considering weakly bounded spins at the anti-ferromagnetic domain walls in the material, which appears to be universal within the $A_2\text{Ir}_2\text{O}_7$ family. The influence of the iridium magnetism on the A^{3+} single ion properties was found to be weak. A standard crystal field model for respective A^{3+} was used to describe dispersion-less magnetic excitations in inelastic neutron scattering spectra of $\text{Er}_2\text{Ir}_2\text{O}_7$ and $\text{Tm}_2\text{Ir}_2\text{O}_7$.

Keywords: pyrochlore iridates, synthesis from flux, magnetization, specific heat, neutron scattering, muon spin rotation, all-in-all-out structure, crystal field excitations

Název: Magnetické vlastnosti vzácnozeminných $A_2\text{Ir}_2\text{O}_7$ pyrochlorových iridátů

Autor: Kristina Vlášková

Katedra: Katedra fyziky kondenzovaných látek

Vedoucí disertační práce: RNDr. Milan Klicpera, Ph.D., Katedra fyziky kondenzovaných látek

Abstrakt: Tato disertační práce je zaměřena na syntézu, charakterizaci a magnetické vlastnosti pyrochlorových iridátů $A_2\text{Ir}_2\text{O}_7$, kde A je Dy - Lu. Geometrická frustrace pyrochlorové mřížky ovlivňuje interakce mezi magnetickými momenty A^{3+} i Ir^{4+} iontů a podílí se na jejich komplexním nízkoteplotním uspořádání. Souhra spin-orbitální vazby a elektronových interakcí, vlastní iridiovým iontům, také značně ovlivňuje vodivostní vlastnosti pyrochlorů. Iridáty $A_2\text{Ir}_2\text{O}_7$ byly syntetizovány, a syntéza optimalizována, metodou růstu z CsCl fluxu. Důkladně charakterizované vzorky, včetně dříve nepřipraveného $A = \text{Tm}$ analogu, byly studovány jak objemovými metodami, tak mikroskopickými technikami neutronového rozptylu a muonové spinové resonance. Vývoj magnetického uspořádání iridiové podmříže byl sledován u všech těžkovzácnozeminných sloučenin. Příslušný fázový diagram pro $A_2\text{Ir}_2\text{O}_7$ byl dokončen. Oscilace ve spektru muonové rotační spektroskopie jednoznačně prokázaly existenci dalekodosahového uspořádání iridiových momentů ve studovaných oxidech. Dynamická odezva sloučenin studována AC susceptibilitou byla diskutována v rámci modelu založeném na volně vázaných iridiových momentech ve stěnách antiferromagnetických domén, jejichž existence se zdá být společná pro všechny $A_2\text{Ir}_2\text{O}_7$. Vliv iridiového magnetismu na chování A^{3+} iontů se ukázal být slabý. Standartní model krystalového pole pro dané A^{3+} ionty byl použit pro popis nedisperzních magnetických excitací ve spektrech nepružného neutronového rozptylu iridátů $\text{Er}_2\text{Ir}_2\text{O}_7$ a $\text{Tm}_2\text{Ir}_2\text{O}_7$.

Klíčová slova: pyrochlorové iridáty, syntéza z fluxu, magnetizace, měrné teplo, neutronový rozptyl, muonová spinová rotace, struktura all-in-all-out, krystalopolní excitace

Contents

Introduction	3
1 Theoretical background	5
1.1 Single ion magnetism	5
1.2 Spin-orbit coupling, the case of Ir^{4+}	6
1.3 Crystal field	8
1.4 Frustration of magnetic moments	10
1.5 Thermodynamics of the crystal growth	12
2 Experimental methods	15
2.1 Preparation techniques	15
2.1.1 Solid state reaction	15
2.1.2 Flux growth	15
2.1.3 Hydrothermal synthesis	16
2.2 X-ray and neutron diffraction	17
2.3 Electron microscopy	19
2.4 Specific heat	20
2.5 Magnetization measurement	21
2.6 Inelastic neutron scattering	23
2.7 AC-sucseptibility	25
2.8 Muon spin resonance	27
3 Previous results	29
3.1 Crystal structure of $A_2\text{Ir}_2\text{O}_7$	29
3.2 Electronic states in $A_2\text{Ir}_2\text{O}_7$	30
4 Experimental results	33
4.1 Synthesis and characterisation of $A_2\text{Ir}_2\text{O}_7$	33
4.1.1 Solid-state synthesis of $\text{Er}_2\text{Ir}_2\text{O}_7$	33
4.1.2 Synthesis of $A_2\text{Ir}_2\text{O}_7$ by CsCl flux method	39
4.1.3 Hydrothermal synthesis	44
4.2 Magnetization and specific heat of $A_2\text{Ir}_2\text{O}_7$	45
4.2.1 $\text{Lu}_2\text{Ir}_2\text{O}_7$	45
4.2.2 $A_2\text{Ir}_2\text{O}_7$ with $A = \text{Dy}, \text{Er}, \text{Tm}$ and Yb	49
4.3 Inelastic neutron scattering on $\text{Er}_2\text{Ir}_2\text{O}_7$ and $\text{Tm}_2\text{Ir}_2\text{O}_7$	58
4.3.1 Crystal field scheme of $\text{Er}_2\text{Ir}_2\text{O}_7$	58
4.3.2 Lattice and magnetic excitations in $\text{Tm}_2\text{Ir}_2\text{O}_7$	62
4.3.3 Mean field calculations	67
4.4 Powder neutron diffraction of $\text{Tm}_2\text{Ir}_2\text{O}_7$	70
4.5 μSR spectroscopy of $\text{Er}_2\text{Ir}_2\text{O}_7$ and $\text{Tm}_2\text{Ir}_2\text{O}_7$	72
4.6 Dynamic response of $A_2\text{Ir}_2\text{O}_7$	76
4.6.1 AC magnetic susceptibility	76
4.6.2 Isothermal magnetization of $A_2\text{Ir}_2\text{O}_7$	82
5 Discussion and conclusions	87

Bibliography	103
List of Figures	103
List of Tables	104
List of Symbols and Abbreviations	105
List of publications	108

Introduction

Scientific interest in $A_2\text{Ir}_2\text{O}_7$ compounds, with A being a rare-earth ion, is motivated by the emergence of complex electronic properties originating in the spin-orbit coupling, frustration of magnetic moments on both A and Ir sublattice and their entanglement. $A_2\text{Ir}_2\text{O}_7$ iridates crystallize in the cubic $F d \bar{3} m$ structure [1]. Both A^{3+} and Ir^{4+} ions reside on two separate sublattices of interpenetrating corner-sharing tetrahedra; a canonical example of a three-dimensional frustrated lattice. Magnetic moments on geometrically frustrated lattice order in frequently exotic magnetic structures or remain dynamic in a correlated spin-liquid regime [2]. Moreover, the interplay between spin-orbit coupling and electron correlations in $A_2\text{Ir}_2\text{O}_7$ can result in topologically non-trivial electron states such as Weyl semimetals or axion insulators [3, 4].

$A_2\text{Ir}_2\text{O}_7$ pyrochlores reveal a change in electrical conductivity depending on the rare-earth: compounds with $A = \text{Pr}$ and Nd being metallic [5, 6], over semi-metallic $A = \text{Sm}$, Eu [7] to non-metal heavy rare-earth end of $A_2\text{Ir}_2\text{O}_7$ series [8]. Decreasing the temperature, metal-to-insulator transition concomitant with the iridium sublattice magnetic ordering is detected in $A_2\text{Ir}_2\text{O}_7$ [8, 9, 10] with exception of $\text{Pr}_2\text{Ir}_2\text{O}_7$, which remains metallic down to low temperatures. Magnetic structure of $A_2\text{Ir}_2\text{O}_7$ iridium moments was identified as all-in-all-out antiferromagnetic structure (AIAO) where the Ir moments at the four vertices of each corner-sharing tetrahedron point along a local $\langle 111 \rangle$, either inward or outward in an alternating manner.

Low-temperature state of pyrochlore iridates, connected to the A sublattice, remains enigmatic. Significant scientific effort was devoted to the study of light rare-earth $A_2\text{Ir}_2\text{O}_7$. $\text{Pr}_2\text{Ir}_2\text{O}_7$ shows spin-liquid behaviour with partial freezing of magnetic moments [11]. Metal-to-insulator transition in $\text{Nd}_2\text{Ir}_2\text{O}_7$ is accompanied by a huge increase of magnetoresistance effect [6]. Based on the optical measurements, the Weyl semimetal state was suggested to appear in the case of $\text{Eu}_2\text{Ir}_2\text{O}_7$ [12].

Present work is focused on the heavy rare-earth part of $A_2\text{Ir}_2\text{O}_7$ series, where the Ir moments are supposed to enter the AIAO ordering at higher temperatures (120 - 140 K [13, 14, 15]), whereas the correlations between the rare-earth moments are manifested at much lower temperatures, depending on the particular rare-earth. The iridium exchange field, entanglement of iridium and rare-earth magnetism, the single-ion magnetism of the rare-earth and the type of magnetic correlations dictate the ground state of $A_2\text{Ir}_2\text{O}_7$. Investigation of $\text{Tb}_2\text{Ir}_2\text{O}_7$ revealed the concurrent ordering of Ir and Tb moments at 140 K (ordering of Tb moments likely induced by Ir molecular field) followed by the additional magnetic component of Tb moments below 10 K [16]. Recent studies on $A_2\text{Ir}_2\text{O}_7$ with $A = \text{Dy}$ and Ho suggested the realization of the fragmented monopole crystal state with A moments divided into an AIAO structure and dynamically correlated moments in Coulomb phase [14, 15]. Ferromagnetic interaction between ytterbium ions in $\text{Yb}_2\text{Ir}_2\text{O}_7$ competes with a coupling to antiferromagnetic Ir sublattice, leading to a moment suppression well below the saturated value of Yb^{3+} [13]. The results of heavy rare-earth $A_2\text{Ir}_2\text{O}_7$ studies indicate a complexity of mutual Ir and rare-earth interactions, where, for most of them, comprehensive and

microscopical studies are desired.

A thesis is organised as follows: Chapter 1 introduces the theory of single-ion magnetism, magnetically frustrated systems, and fundamentals of crystal growth thermodynamics. Chapter 2 provides an overview of experimental techniques employed for preparation, characterisation, and microscopic properties measurements on $A_2\text{Ir}_7\text{O}_7$ compounds, together with a technical description of individual experiments. The state-of-the-art is briefly reviewed in Chapter 3. Chapter 4 consists of sections focused on sample synthesis, characterisation, magnetization, specific heat analysis, crystal field scheme determination, and dynamical properties investigations.

Most of the results of the present Ph.D. study have been published in peer-reviewed journals; the respective publications are listed in the attached documents. In addition to $A_2\text{Ir}_2\text{O}_7$, considerable attention was paid to zirconium counterparts $A_2\text{Zr}_2\text{O}_7$. The related results are not presented in this Ph.D. thesis to maintain a reasonable length and coherence of the text. The results of $A_2\text{Zr}_2\text{O}_7$ were partly published (see the List of publications), and most of the results are still to be submitted to scientific journals.

1. Theoretical background

1.1 Single ion magnetism

Behaviour of magnetic moments is frequently described using quantum mechanics formalism. Magnetic moment carried by an electron of mass m_e and charge e component is defined by two contributions: orbital and spin contributions [17]

$$\begin{aligned}\hat{\boldsymbol{\mu}}_l &= -\mu_B \hat{\boldsymbol{l}}, \\ \hat{\boldsymbol{\mu}}_s &= -\mu_B g_0 \hat{\boldsymbol{s}},\end{aligned}\tag{1.1}$$

where μ_B is the Bohr magneton; $\hat{\boldsymbol{l}}$ and $\hat{\boldsymbol{s}}$ are the operators of the electron orbital and spin moments, respectively; $g_0 = 2.0023$ [17] denotes the gyromagnetic ratio of the electron. Assuming the external magnetic field along the z-direction, the component of $\boldsymbol{\mu}$ parallel to the external field will have the form

$$\begin{aligned}\mu_{lz} &= -m_l \mu_B, \\ \mu_{sz} &= -g_0 m_s \mu_B.\end{aligned}\tag{1.2}$$

Besides the integer value of the orbital quantum number m_l , the spin quantum number m_s can reach the eigenvalues $s_z = \pm 1/2$ for a spin aligned parallel or antiparallel to z-axis/field direction.

The field acting on the electron can also be induced by the orbital motion of the electron itself; in that case, the spin-orbit coupling (SOC) is to be taken into account. The degeneracy of the electron energy level is lifted by the spin-orbit coupling, $\boldsymbol{l} \cdot \boldsymbol{s}$ (see also the following section).

The energy U_B of the magnetic moment placed in the magnetic field of induction \boldsymbol{B} is determined by the relation

$$U_B = -\boldsymbol{\mu} \cdot \boldsymbol{B}.\tag{1.3}$$

A system containing n electrons with weak spin-orbit coupling can be characterised by the total spin \boldsymbol{S} and orbital angular momentum \boldsymbol{L}

$$\begin{aligned}\boldsymbol{S} &= \sum_i^n \boldsymbol{S}_i, \\ \boldsymbol{L} &= \sum_i^n \boldsymbol{L}_i.\end{aligned}\tag{1.4}$$

The sum of \boldsymbol{S} and \boldsymbol{L} represents the total momentum $\boldsymbol{J} = \boldsymbol{S} + \boldsymbol{L}$ and takes the following values: $|L - S|$, $|L - S + 1|$, ..., $L + S - 1$, $L + S$.

Hamiltonian operator describing an atom of n electrons under an external field (intensity \boldsymbol{H}) is expressed as

$$\hat{H} = \hat{H}^0 + \mu_B \boldsymbol{H} (\hat{\boldsymbol{L}} + g_0 \hat{\boldsymbol{S}}) + \frac{e^2}{8m_e c^2} \sum_j (\hat{\boldsymbol{x}}^2 + \hat{\boldsymbol{y}}^2).\tag{1.5}$$

\hat{H}^0 denotes an atomic Hamiltonian without external field, $\hat{\mathbf{x}}$ and $\hat{\mathbf{y}}$ represent a quantum mechanical operator of the electron positions x and y , c is the velocity of light in vacuum.

Under the assumption of the small value of field \mathbf{H} , the second-order perturbation theory [18] applied to the Hamiltonian 1.5 leads to the energy correction towards the $\langle n|$ state

$$\begin{aligned} \Delta E_n = & \mu_B \mathbf{H} \langle n | \hat{\mathbf{L}} + g_0 \hat{\mathbf{S}} | n \rangle + \frac{e^2}{8m_e c^2} H^2 \langle n | \sum_j (\hat{\mathbf{x}}^2 + \hat{\mathbf{y}}^2) | n \rangle \\ & + \sum_{m \neq n} \frac{|\mu_B \mathbf{H} \langle n | \hat{\mathbf{L}} + g_0 \hat{\mathbf{S}} | m \rangle|^2}{E_n - E_m}. \end{aligned} \quad (1.6)$$

The first expression of 1.6, linear in \mathbf{H} , is responsible for the paramagnetic behaviour. The magnetic moment of the partially occupied electron shell is then equal to

$$\boldsymbol{\mu} = \mu_B (\mathbf{L} + g_0 \mathbf{S}), \quad (1.7)$$

whereas is zero in the case of the fully occupied shell. The second expression in 1.6 has a quadratic dependence on the field magnitude and non-zero value for the partially filled electron shell. It is connected with the diamagnetic response of the system and is called Larmor diamagnetism. The third term of the 1.6, Van Vleck paramagnetic term, is non-zero for neutral atoms and charged ions.

1.2 Spin-orbit coupling, the case of Ir^{4+}

Spin-orbit coupling (SOC) or spin-orbit effect is a relativistic interaction between the spin of an electron and its motion inside the potential of the ion. The ion radial electrostatic potential $V(r)$ scales with the $\frac{Z}{r}$, where Z denotes the nucleus charge, and r is the magnitude of the electron radial vector. Considering the electron characterised by quantum numbers n , l and s the spin-orbit interaction is expressed up to order $(\frac{v}{c})^2$ after the expansion of the Dirac equation [18] as

$$\hat{H}_{\text{SOC}} = \frac{e}{(mc)^2} \frac{1}{r} \frac{\partial V(r)}{\partial r} \mathbf{s} \cdot \mathbf{l}. \quad (1.8)$$

In the case of weak spin-orbit coupling, the interaction in the electron shell is expressed under the Russel-Sanders approximation

$$\hat{H}_{\text{SOC}} = \Lambda \mathbf{S} \cdot \mathbf{L}, \quad (1.9)$$

where the SOC interaction is characterised by the constant Λ proportional to $\frac{Z^4}{n^3}$ [17] and the scalar product of the total orbital and spin angular momenta of electron, see section 1.1.

The strength of SOC in transition metal systems reveals a universal increase from $3d$ (~ 0.01 eV) over $4d$ (~ 0.1 eV) to $5d$ electron compounds (~ 1 eV) [19]. The localised $4f$ electrons of heavy rare-earth are exposed to the spin-orbit splitting of several eVs.

Focusing on the subject of our interest, that is, the compounds containing Ir^{4+} ion, a $5d$ element with the strong spin-orbit coupling, the following scheme

is drawn. The behaviour of Ir^{4+} electrons with $J_{eff} = 1/2$ is determined by the interaction of the free ion projected into the t_{2g} manifold and the kinetic terms of the t_{2g} electrons. Under the simplifying assumption of the well-separated $J_{eff} = 1/2$ and $J_{eff} = 3/2$ bands, Ir^{4+} electrons can be described by Hubbard repulsion of electrons, kinetic energy, and spin-orbit interaction as summarized in the expression [3]

$$\hat{H} = -t \sum_{i,j} \sum_{\sigma} (c_{i\sigma}^{\dagger} c_{j\sigma} + c_{i\sigma} c_{j\sigma}^{\dagger}) + \hat{V}_{SOC} + U \sum_i n_{i\uparrow} n_{i\downarrow}, \quad (1.10)$$

where t represents the hopping integral, σ denotes the electron spin state, $c_{i\sigma}$ and $c_{i\sigma}^{\dagger}$ are the annihilation and creation fermionic operators, respectively. Electron repulsion between the on-site electrons is expressed by the constant U and the number operator of the on-site electrons $n_{i\sigma} = c_{i\sigma}^{\dagger} c_{i\sigma}$. The kinetic term favours the delocalization of the electrons, whereas the Hubbard repulsion pushes the system towards the local moment formation [3]. The spin-orbit interaction reduces the electron bandwidth, and even a moderate Hubbard repulsion can open an insulating gap. The model Hamiltonian 1.10 does not have an exact solution; however, a schematic phase diagram of possible electron states can be plotted as a function of the relative strength of Λ/t and U/t renormalized to the kinetic energy t .

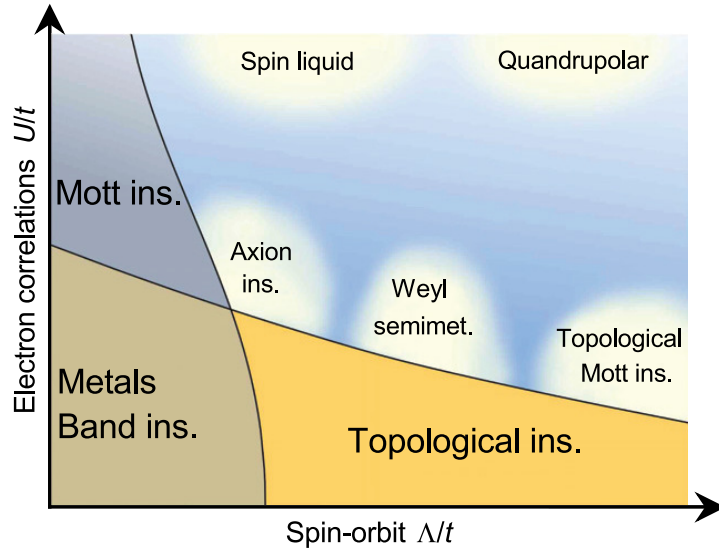


Figure 1.1. *Generic phase diagram of electron states in $A_2\text{Ir}_2\text{O}_7$.* Schematic phase diagram of electronic states dependent on the relative strength of spin-orbit coupling Λ and electron-electron correlation U normalized to the kinetic energy hopping t . The figure was adopted from [3].

For simplicity, both electron correlation and spin-orbit coupling can be divided into strong and weak interaction regimes, which generate four quadrants in the phase diagram 1.1. In the weak SOC and weak electron correlation regime (bottom left part of the phase diagram 1.1) the conventional metallic or band insulator states emerge. Moving up in the phase diagram, i.e. increasing the electron correlation with preserving the weak SOC, electrons are pushed to be localized, and the Mott insulating phase is identified. It is a typical case of $3d$ transition metal oxides with narrow electron bands and strong correlations.

On the other hand, an increase of the spin-orbit coupling in the weak electron correlation regime leads to the emergence of topological insulating states (right bottom part of the Figure 1.1).

The coexistence of spin-orbit coupling and electron correlations gives rise to unusual electronic states; examples are listed in the centre part of the phase diagram 1.1. Spin-orbit coupling of electrons causes the narrowing of electron bands and makes them more sensitive to electron correlations. Vice versa, considering the correlation effect first, the preferential localization of the electrons decreases their kinetic energy and enhances the one-site spin-orbit coupling effect [3]. The cooperation of the correlation and spin-orbit coupling effects is denoted by the shift of the vertical and horizontal boundaries that separate the weak correlation regimes towards lower $\langle \hat{V}_{SOC} \rangle$ and U with increasing U and $\langle \hat{V}_{SOC} \rangle$. Such a situation is sometimes called a correlated spin-orbit coupling regime.

Regarding the experimental realization of the correlated topological states, studies of Ir^{4+} compounds appear to be crucial. To list a few, the study of the layered perovskite family $\text{Sr}_{n+1}\text{Ir}_n\text{O}_{3n+1}$ revealed a correlated metallic state [20]. SrIrO_3 ferromagnet was identified to have $J_{eff} = 1/2$ Mott insulating ground state driven by spin-orbit coupling [21]. The presence of the metal-insulator transition in the case of the cubic $A_2\text{Ir}_2\text{O}_7$ together with the significant spin-orbit coupling put the iridium based pyrochlores on the forefront of scientific interest; the details of the electronic structures will be discussed later in Chapter 3.

1.3 Crystal field

Magnetic ion placed in the crystal lattice is surrounded by the nearest neighbour ligands. The number of ligands and their geometrical arrangement depend on the crystal lattice symmetry. The crystal charge density creates a crystal field (CF), which acts upon the electrons from the unfilled shell of the magnetic ion. The spherical symmetry of an isolated ion is reduced to the point symmetry of the crystal lattice site occupied by the magnetic ion. As a result of the reduction in symmetry and the influence of the CF, the (free) magnetic ion multiplets are split into a number of sublevels, the splitting pattern completely determined by the properties of the crystal field.

The influence of the CF is represented by the crystal field Hamiltonian [19]

$$\hat{H}_{CF} = \sum_{l,m} B_l^m \hat{O}_l^m, \quad (1.11)$$

where the summation goes over the quantum numbers $l = 0, 1, \dots, l$ and $m = l, l-1, \dots, -l+1, -l$. The \hat{O}_l^m are the Steven's operators representing the radial matrix elements of crystal field interactions in terms of angular momentum operators and B_l^m stand for crystal field parameters, the number of which is strongly restricted by magnetic ion point symmetry. The results of CF energy splitting depend on the electronic nature and position of the ligands and on the type of magnetic ions; however, some generalizations can be found for individual categories of magnetic ions.

In $3d$ -transition metal compounds, electron orbitals have small direct overlap and experience an efficient Coulomb repulsion, making the electron bands neither

extremely wide nor narrow. Due to the significant overlap with ligand wave functions, CF splitting energy (~ 1 eV) is larger than the SOC ($\lesssim 0.1$ eV) and are comparable with electrostatic interactions [19]. An increased density of $4d$ and $5d$ electrons near the nucleus and the higher atomic number Z of compounds amplifies the SOC ($\gtrsim 0.1$ eV); however, it is dominated by a larger CF splitting (~ 1 eV) [22].

The proximity of $4f$ electrons to the nucleus and an increased charge of nucleus Z leads to the significant SOC (~ 1 eV), which couples the spin S and angular momentum L to the total angular momentum J . Since the bonding effects are expected to be very small/negligible for heavy rare-earth $4f$ electrons (CF strength $\lesssim 0.1$ eV), the interaction with the ligands is treated as a perturbation. Any non-spherical potential reduces the rotational symmetry and causes magnetocrystalline anisotropy in rare-earth compounds. The rare-earth multiplets are labelled by $^{2S+1}L_J$, where L represents the orbital angular momentum of the orbital term and S being the total spin number. The individual ion contributions to the magnetic properties of the rare-earth are determined by the total angular momentum J , see section 1.1. The ground-state multiplet is characterised by $J = |L - S|$ and $J = |L + S|$ for less or more than half - occupied electron shell according to *Hund's rules*.

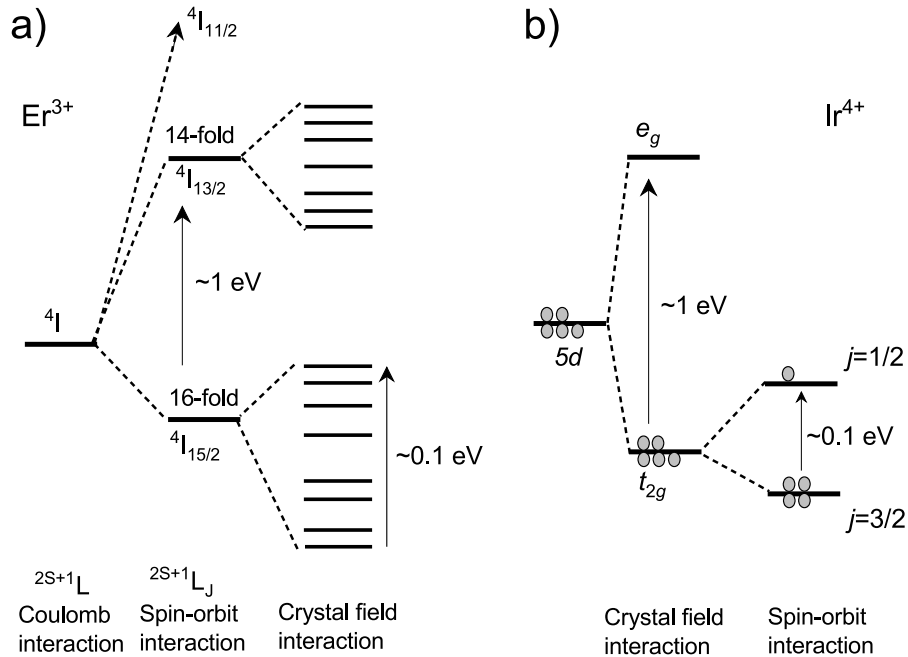


Figure 1.2. Splitting of electron energy levels in $4f$ and $5d$ compounds. a) The effect of SOC and CF splitting of the rare-earth energy levels (represented by erbium ion with doublets as final states) and b) iridium levels with electrons represented by grey circles.

A successive effect of SOC and CF on $4f$ and $5d$ ions represented by Er^{3+} and Ir^{4+} is illustrated in Figure 1.2. The $[\text{Xe}]4f^n5d^16s^2$ and excited $[\text{Xe}]4f^{n-1}5d^26s^2$ electron states of erbium ion are separated by the energy barrier of ~ 10 eV [23], the SOC in the rare-earth ions splits the energy levels by ~ 1 eV [23]. The CF affects the ground state J -multiplet splitting it by energies of order 0.1 eV

(see Figure 1.2 a).

Electron levels of Ir^{4+} ions with $5d^5$ configuration under the crystal field will split into the lower-lying t_{2g} and empty e_g manifolds separated by 10^3 meV energy gap (Figure 1.2b). Electrons in the t_{2g} state with spin $S = 1/2$ are the subject of the SOC; the eigenstates can be described by an effective total angular momentum, $J_{eff} = L \pm S$. The lower-lying quartet with $J_{eff} = 3/2$ and higher-lying $J_{eff} = 1/2$ doublet are then separated by 100 meV with the latter being half occupied [3].

1.4 Frustration of magnetic moments

In crystalline materials, magnetic ions are correlated via magnetic interactions. To list a few, the *direct exchange* interaction between neighbouring magnetic moments is realized in the case of *s*- or *p*-metal based compounds with sufficient overlap of their wave functions. The *superexchange* interaction between the next-to-nearest-neighbour magnetic moments is realized through the non-magnetic ions present in the lattice. The rare-earth moments in metallic compounds with a small wave function overlap interact via conducting electrons and polarization of their spins (Ruderman–Kittel–Kasuya–Yosida, RKKY interaction). A spontaneous ordering of magnetic moments into the periodic structure can appear as a result of minimization of interacting energy (generally at low temperature). At sufficiently high temperatures, thermal fluctuations of magnetic moments prevent the magnetic ordering, and the material is found to be in a paramagnetic state, where the magnetic moments are oriented randomly. The paramagnetic macroscopic net magnetization is zero, and the positive magnetic susceptibility response to the external magnetic field is detected.

Certain types of structural arrangement of magnetic moments cause the magnetic interactions to compete; thereby, the magnetic ordering is suppressed down to a strongly correlated regime at low temperatures. The phenomenon of magnetic frustration is one of the crucial chapters in the study of unusual magnetic states. The concept of geometrical frustration has been deeply studied since the 1950s when the system of Ising spins with antiferromagnetic interaction residing on the triangular lattice revealed a different behaviour from isostructural ferromagnets or bi-partite antiferromagnets [24].

Geometrical frustration of magnetic moments arises when the magnetic moments' arrangement on a lattice precludes satisfying all interactions simultaneously. Three antiferromagnetically coupled Ising moments residing on the equilateral triangular lattice represent a simple 2D example. Once two moments are antiparallely aligned, the third moment cannot fulfill the condition of the AF coupling with both arranged moments. The 2D crystal structure based on the triangular motif can be formed by corner-sharing (kagomé) or edge-sharing triangles, driving the frustration in the layered compounds. Not only the triangular geometry but also the square lattice with two kinds of antiferromagnetic interactions give rise to magnetic frustration. Considering the 3D systems, canonical examples of frustrated lattices are the pyrochlore and hyperkagomé structures. Magnetic moments of the pyrochlore compounds are arranged in the sublattice of corner-sharing tetrahedra. The system can exhibit frustration in both the isotropic Heisenberg antiferromagnet and the Ising limit. The prevailing antifer-

romagnetic interactions between Ising-like moments lead to the doubly degenerated ground state with all spins pointing out or all spins pointing in of respective tetrahedra (AOAI structure, Figure 1.3 a). The ferromagnetic interaction pushes the system to the ground state determined by *ice rules* discussed below. Similarly in the hyperkagomé lattice, which consists of corner-sharing triangles of magnetic moments derived from different faces of the tetrahedra with 1/4 depletion of magnetic moments [25].

Experimental signatures of frustration are demonstrated in the development of the inverse magnetic susceptibility $\chi^{-1} \sim T - \Theta_{CW}$ with temperature, where Θ_{CW} denotes a Curie-Weiss constant. The plus/minus sign of Θ_{CW} indicates the prevailing ferromagnetic or antiferromagnetic interactions, respectively. A frustrated system does not reveal a magnetic ordering at the temperature scale given by the strength of interaction Θ_{CW} . Instead, the paramagnetic state prevails down to temperatures well below $|\Theta_{CW}|$. Magnetic moments can order or freeze at temperature T_C . The ratio f defined as T_C/Θ_{CW} denotes the strength of frustration and serves for classification of the frustrated state [26]. The key to understanding the magnetic behaviour in the strongly correlated regime $T \ll \Theta_{CW}$ is the description of the ground state. The geometrical frustration inhibits the formation of the magnetic structure and causes the ground state degeneracy. The number of frustrated sites is $\sim N_A$; therefore, the ground state degeneracy is experimentally observable in the thermodynamic properties.

Further focusing on the pyrochlore lattice, it is useful to recall the so-called *ice rule* in water-ice system [27]. In water ice, the arrangement of the hydrogen-oxygen pairs is governed by strong local interactions known as *ice rules*. Two hydrogens are near the oxygen; the hydrogen-oxygen bonds point towards the other two of the four nearest neighbour oxygens formed in the tetrahedra. The configuration of water molecules restricted by the *ice rules* in the crystal lattice can be realized by six energetically equivalent possibilities. The residual entropy at zero temperature is quantified as $R \ln(3/2)$ per mole [28].

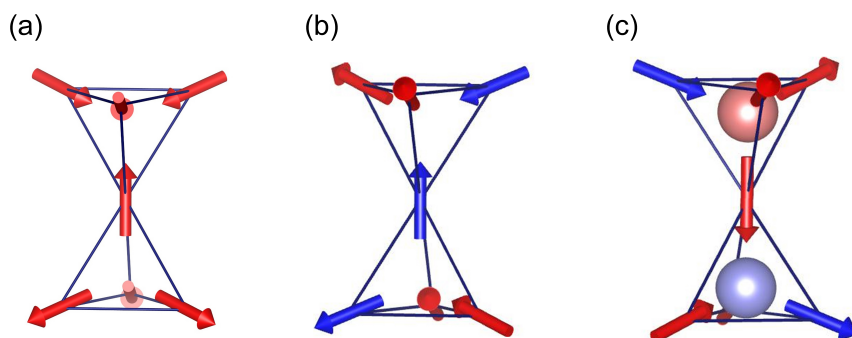


Figure 1.3. *Arrangement of magnetic moments on pyrochlore lattice.* a) All-in-all-out antiferromagnetic structure on the pyrochlore lattice, b) 2-in-2-out structure (spin-ice structure), c) three-in-one-out spin arrangement excited from the spin-ice state by spin-flip. Blue and red spheres denote the magnetic monopoles with a negative and positive charge, respectively.

Ferromagnetic interactions between magnetic moments on the pyrochlore lattice lead to the state governed by similar ice rules. The moments form the so-called 2-in-2-out structure, spin ice, see Figure 1.3 b). The magnetic structure consisting of two spins pointing in and two out of any given tetrahedron minimizes the energy of ferromagnetic interaction between spins analogously to the hydrogen ordering in water ice with a similar configuration entropy of $R \ln(3/2)$ per mole tetrahedron. Good examples are the classical spin ice compounds $\text{Dy}_2\text{Ti}_2\text{O}_7$ and $\text{Ho}_2\text{Ti}_2\text{O}_7$ with large $\langle 111 \rangle$ Ising-like magnetic moments [29, 30] and extensive ground state degeneracy. The application of the external magnetic field on the spin-ice state can lift the degeneracy as a result of easy-axis rotation and cause/allow the magnetic ordering on the pyrochlore lattice without breaking of symmetry during the first-order transition [2].

In spin-ice systems, the spin configurations tunnel among themselves via thermal or quantum fluctuations and form classical or quantum spin liquid candidates [31]. The spin system without symmetry-breaking magnetic order down to zero temperature is proposed to consist of spins singlets with the resonance on the lattice, further extended to the model of valence bonds for all length scales with a macroscopically quantum entangled ground state [32]. Strongly correlated phases give rise to unusual excitations of fractionalized quasiparticles. As an example, a Coulomb phase observed in the case of $\text{Ho}_2\text{Ti}_2\text{O}_7$ in which the spin flips deviating from *ice rules* (see Figure 1.3 c) create mobile magnetic monopoles with half of the dipole moment interacting via classical magnetostatics [33]. Contrary to the case of large Dy^{3+} and Ho^{3+} moments ($10 \mu_B$), the behaviour of pyrochlore compounds with effective $S = 1/2$ moments is significantly influenced by the quantum fluctuations [34].

1.5 Thermodynamics of the crystal growth

Synthesis of high-quality samples is necessary for reliable physical measurements and the unambiguous interpretation of the physical properties. The existence of parasitic phases, structural defects, or uncontrolled grain boundaries is minimized in a sample with chemical homogeneity and good crystallinity. Therefore, optimization of the sample preparation process is an integral part of physical research. To gain insight into the sample synthesis, the fundamental relations between the thermodynamic quantities during the phase formation are introduced.

Thermodynamical systems can be divided according to the number of constituting phases into single- or multi-component. A single-component system consists of one pure chemical characterised by intensive variables: temperature T , volume V , and pressure p . The multi-component system is additionally described by the number of moles of each component n_i [35].

The system is described by respective thermodynamical potentials. For a multi-component system, it is convenient to define the Gibbs free energy [36]

$$dG = -SdT + Vdp + \sum_{i=1}^{\nu} \mu_i dN_i \quad (1.12)$$

in the form of total differential, where S denotes the entropy of the system and μ_i stands for the chemical potential of the substance i . The Gibbs energy of the

system in thermodynamical equilibrium at constant pressure and temperature tends to its minimum, and its differential acquires zero value [36]. Under constant temperature and pressure, the equation 1.12 for thermodynamical equilibrium is simplified into

$$0 = \sum_{i=1}^{\nu} \mu_i dN_i. \quad (1.13)$$

A driving force of the phase transition is the difference between the chemical potentials of individual phases. If the individual chemical potentials are equal, no phase transition occurs. This work is focused on solid forms of matter with a high degree of particle ordering: single-crystalline and polycrystalline samples with the periodical arrangement of building blocks in the whole sample volume (single crystals) or individual grains with different orientations (polycrystals).

The crystal growth can be regarded as a first-order phase transition into the solid-state from the solid, liquid, or vapour phase. It implies the coexistence of two distinct uniform phases stable at the equilibrium point, separated by a phase boundary. The equilibrium state between the crystal and its parent phase is characterised by a minimum value of G [37]. To start a crystal growth, the equilibrium has to be disturbed by an appropriate change of the system parameters such as temperature, pressure, chemical potential, etc. From the microscopic point of view, the emergence of chemical bonds between crystal constituents decreases the G of the system, and the phase transition into the solid phase is energetically favourable.

Crystal growth can be divided into three steps: (1) achievement of supersaturated conditions (supersaturation or supercooling), (2) nucleation of the crystal grain, and (3) growth of the crystal [35]. By nucleation, the system reaches equilibrium and the supersaturation conditions vanish; therefore, the maintenance of supersaturation is crucial for stable crystal growth. The formation of small clusters of crystal phase with critical size is a prerequisite for the macroscopic crystal development [38]. The emergence of nucleation centres can occur spontaneously or may be artificially induced. The choice of parent phase, supersaturated conditions, and nucleation manner leads to the variety of sample growth techniques which is introduced in section 2.1.

2. Experimental methods

2.1 Preparation techniques

A large variety of sample preparation techniques are available, reflecting the richness of chemical reactions combined with a number of technical realizations. We restrict ourselves to give a brief overview of the techniques relevant for the synthesis of Ir-based pyrochlore oxides we employed in the preparation of further studied compounds. Solid state reaction, flux growth, and hydrothermal synthesis techniques are introduced.

2.1.1 Solid state reaction

One of the most straightforward techniques of sample preparation is solid state synthesis [39]. During the reactant heating, the formation of the product phase between neighbouring particles occurs spontaneously if the total G decreases thereby. The reaction process is realized by diffusion of the atoms or ions of type i with a charge z_i driven by the gradient of the chemical or electrochemical potentials. The inhomogeneity of incoming products and the temperature gradient drive the diffusion of particles. Also, the morphology of reacting particles plays an important role: a migration of the particles from the area of high curvature to the lower one causes a decrease of the surface energy and contributes to the minimization of G .

Solid state reaction is one of the principal preparation techniques for ceramics and high-temperature melting materials. Reaction is conducted in the solid phase, below the melting temperature of reactants, as well as the product. However, the solid state synthesis is usually performed at elevated temperatures (above 1000°C) to obtain the reaction time scales close to hours/days. Tammann's rule suggests a temperature of two-thirds of the melting point of reactants to obtain a reasonable reaction time [40]. The small particle size of the reactants maximizes the contact area, and repetitive grinding of the products ensures a fresh contact surface which speeds up the reaction. The product typically has the form of polycrystalline material, but also single-crystalline samples can be produced using the solid state reaction by seeding the single crystals into the sintered polycrystalline material [41].

2.1.2 Flux growth

Sample synthesis using the flux method covers a wide variety of growth parameters and provides a route for the incongruently- or high-melting, volatile, or unstable compound preparation. Flux growth method belongs to techniques of crystal growth from high-temperature solution and is widely used for the preparation of complex and multicomponent systems [42]. A significant advantage of the flux method is the growth of the desired compound below its melting temperature. If the compound melts incongruently, i.e., exhibits a phase transition below the melting point, decomposes before melting, or has high vapor pressure during melting, sample preparation should be conducted below the upper mentioned

phase transitions. However, the disadvantage of the flux method is connected with the lower growth rates compared with the growth from melt (e.g. Czochralski, Bridgman or floating-zone method) and the possible presence of impurities of flux ions in the resulting sample.

The basic requirement for flux growth is the proper choice of the chemically compatible flux material and temperature range of reaction. The flux is heated to its melting temperature; the initial reactants are dissolved in the flux, they diffuse through the melt, and after the critical concentration is reached, the nucleation of the crystals begins. For further growth of the crystals, the critical concentration should be maintained by an appropriate change of the growth conditions. One of the typical ways to induce crystal growth is by decreasing the reaction temperature. By lowering the temperature, the critical saturation of the reactants decreases, and further growth of the solid phase is needed to reach the equilibrium. A similar effect is to reduce the fraction of the flux by its evaporation.

2.1.3 Hydrothermal synthesis

Another route of sample preparation without melting the constituent reactants is the method of hydrothermal synthesis. The term *hydrothermal* refers to any heterogeneous reaction in the aqueous solvents above ambient pressure and temperature [43]. The hydrothermal synthesis is performed inside a closed inert environment with the aqueous solution that aids the dissolution of the incoming reactants. The low-temperature process can allow the growth of materials that are difficult to melt or reveal chemical instabilities at elevated temperatures. As an aqueous solution, a mineralizer can be used in a wide variety of chemicals such as acids, bases, or inorganic salts. The closed vessel is heated above the boiling point of the water, which results in a dramatic increase in pressure. Aqueous solutions under supercritical conditions, that is, at critical temperature and pressure, differ strongly from those under ambient conditions. The solubility of non-polar reactants increases with the simultaneous increase of particle mobility due to the decrease of solution viscosity and H_2O dissociation into H_3O^+ and OH^- . The aqueous solvent behaves as an ionic solution [44].

Kinetics and crystal formation in the hydrothermal process are also determined by the solubility of reactants, their mobility in the solution, and the redox potential of the medium, ensuring the ions of the required valence [45]. Hundreds of different chemicals and their combinations can be utilized as a mineralizer. Variation of reaction pressures and temperatures makes hydrothermal synthesis a versatile sample preparation technique.

Hydrothermal synthesis was performed in a standard polytetrafluorethylene (PTFE) liner in a stainless steel autoclave reactor (Parr Instrument Deutschland) which was filled and heated within a laboratory oven. According to the reactor dimensions and inner content 23 and 45 ml [46], the autogenous pressure was estimated to vary between 1 and 3 MPa, depending on the exact volumes of individual reactants and solution.

2.2 X-ray and neutron diffraction

The analysis of the sample structure is a crucial part of material science and should complement the thermodynamical and other microscopic measurements. The microscopical structure of crystalline materials can be described within the basic concepts of crystallography. A crystal is defined as a structure built from identical units periodically filling the space. The periodicity is represented by a lattice, which is a periodic array of points such that each point has an identical environment [47]. A three-dimensional lattice is usually described by a position vector \mathbf{l}

$$\mathbf{l} = n_1\mathbf{a}_1 + n_2\mathbf{a}_2 + n_3\mathbf{a}_3, \quad (2.1)$$

where \mathbf{a}_i are non-complanar primitive lattice vectors and n_i are integers. The lattice is populated by the basis, a motif consisting of atoms, molecules or a system of molecules. The building block of the crystal is a unit cell. Each particle in the crystal can be described by the vector \mathbf{j} which is a sum of the lattice position vector \mathbf{l} and the relative particle position in the unit cell \mathbf{d} . The smallest unit cell that corresponds to just one lattice point is called a primitive unit cell.

The space group of a crystal lattice is characterised by a set of symmetry operations (translation, rotation, reflection, inversion, glide, and screw operations) under which the crystal lattice remains unchanged.

Besides the real-space lattice, it is convenient to introduce so-called reciprocal-space lattice. Reciprocal lattice is obtained by the Fourier transform of the crystal lattice. The reciprocal vectors \mathbf{a}_i^* are defined by the relations $\mathbf{a}_i \cdot \mathbf{a}_j^* = 2\pi\delta_{ij}$ (δ_{ij} stands for Kronecker's delta). Consequently, any point of the reciprocal lattice is expressed by its point vector $\mathbf{G} = b_1\mathbf{a}_1^* + b_2\mathbf{a}_2^* + b_3\mathbf{a}_3^*$. The crystalline material is generally advantageous to view as a set of planes labelled with the Miller indices (hkl) . These (hkl) planes in the real space then correspond to the orthogonal $\mathbf{G}_{hkl} = h\mathbf{a}_1^* + k\mathbf{a}_2^* + l\mathbf{a}_3^*$ vectors of the reciprocal lattice. The smallest distance between (hkl) planes is denoted as d_{hkl} and is calculated as $d = 2\pi/|\mathbf{G}_{hkl}|$.

Within the kinematical theory, the diffraction of x-ray radiation or neutrons with the wavelength λ on the system of crystal planes (hkl) reveals a constructive interference under Bragg's condition [47]

$$n\lambda = 2d_{hkl} \sin(\theta_B), \quad (2.2)$$

where an integer number n determines the order of diffraction, and θ_B stands for the angle between the incident beam and the (hkl) crystal planes. The conditions for constructive interference can also be expressed using the reciprocal space vectors. Introducing the scattering vector \mathbf{Q} as a difference between the incident and scattered wavevectors $\Delta\mathbf{k}$. A constructive interference of scattered radiation is realized when

$$\mathbf{Q} = \mathbf{G}, \quad (2.3)$$

known as Laue diffraction conditions.

X-ray scattering is based on the electromagnetic interaction with the electron clouds surrounding the ions in the crystal lattice. Neutrons are scattered by the ions' nuclei as well as electrons from unfilled atomic orbitals, that is, by magnetic moments, further details of neutron scattering are discussed in 2.6. The x-ray

diffraction experiment acts as a Fourier transform of the periodic electron density. Elastic neutron scattering is the Fourier transform of the ions' scattering lengths, which depend on the element and its isotope state, that is, on the potential of the nuclei. The observed intensity I of the radiation scattered by the (hkl) plane is proportional to the square of the structure factor. The structure factor for the x-ray scattering is defined as [47]

$$F_{hkl}^x = \sum_{j=1}^n f_j e^{2\pi i(\mathbf{Q} \cdot \mathbf{d})} = \sum_{j=1}^n f_j e^{2\pi i(hx_j + ky_j + lz_j)}, \quad (2.4)$$

and the analogous expression holds for the neutron nuclear structure factor [48]

$$F_{hkl}^n = \sum_{j=1}^n \bar{b}_j e^{2\pi i(hx_j + ky_j + lz_j)}. \quad (2.5)$$

The summation in both expressions goes over n atoms with the fractional coordinates x_j, y_j, z_j . f_j denotes the x-ray atomic structure factor and \bar{b}_j stands for the coherent neutron scattering length of the j ion.

Symmetry properties of the structure can cause amplification or extinction of the scattered amplitude for particular (hkl) planes. The intensity of the scattered radiation is also dependent on radiation polarisation, thermal vibrations in the sample, the irradiated volume or size of the crystal, but the only parameter containing the structure information is the x-ray and neutron structure factor. However, the phase of F_{hkl}^x/F_{hkl}^n is lost since the measured intensity is proportional to the square of the absolute value of the form factor. Different approaches can be chosen to solve this so-called phase problem. If there is initial knowledge of the probable structure, then the actual structure corresponding to the diffraction pattern is determined by data refinement [49]. Alternatively, the self-convolution of the electron density, *Patterson function*, produces the density map of the interatomic vectors and the actual positions of constituting atoms are determined [49]. However, the information obtained by Patterson maps analysis is strongly influenced by atomic form factors/scattering lengths of respective elements and their ratio.

One of the common uses of x-ray and neutron scattering is the diffraction of monochromatic radiation on the polycrystalline sample, powder diffraction. We restrict ourselves to powder diffraction as all presented data were measured on polycrystals. The polycrystals consist of small single crystalline grains with random crystallographic orientation; therefore, a statistically significant number of all crystallographic planes are in the diffraction condition. The diffraction pattern of the polycrystalline sample can be analyzed using the *Rietveld analysis* [50], which is based on the comparison between the diffraction pattern and the model one. The least squares method is applied to minimize the difference between the measured and calculated intensities. Diffraction peaks are approximated by simple analytical functions and the positions of the diffraction maxima are determined from lattice parameters.

Powder x-ray diffraction experiments were performed using Bruker D8 advance device with symmetric Bragg-Brentano geometry with copper K_α doublet wavelengths (1.5406 and 1.5445 Å). Elastic neutron scattering experiments on $\text{Er}_2\text{Ir}_2\text{O}_7$ and $\text{Tm}_2\text{Ir}_2\text{O}_7$ at temperatures down to 0.1 K were realized employing

E6 diffractometer at Helmholtz Zentrum Berlin (HZB; $\lambda = 2.436 \text{ \AA}$, sample mass of 4 g, copper container and methanol-ethanol mixture) and Institut Laue-Langevin (ILL; $\lambda = 2.528 \text{ \AA}$, sample mass of 3.5 g, copper container), respectively.

2.3 Electron microscopy

Electron microscopy covers various experimental techniques that offer unique insights into the material's structure, topology, morphology, and composition. The wealth of information obtained by various methods originates from the multitude of signals that arise when electrons interact with a sample [51]. For the purpose of this work, the attention is focused on the electron interactions on which the sample characterisation was based.

In terms of energy transfer, the interactions can be divided into elastic and inelastic. Elastic signal emerges from the Coulomb deflection of electrons on positively charged nuclei or non-interacting electrons passing through a sample. An elastic signal is exploited in transition electron microscopy (TEM), electron diffraction methods, and surface imaging using back-scattered electrons (BSE) [52]. The elastic scattering by Coulomb interaction of electrons with atoms explains the contrast mechanisms in electron microscopy [51]. The probability that an electron deviates from its direct path by an interaction with an atom increases with the atom charge. Therefore, heavier elements represent more powerful scattering centers than light ones. That is, due to the increase of the Coulomb force with increasing atomic number, the measured intensity is higher for heavy atoms.

Inelastically scattered electrons excite various types of signals from the sample such as inner-shell electron ionization, braking radiation, secondary electrons, phonons, plasmons, etc. The excited inner-shell electrons give rise to x-ray radiation during deexcitation with the characteristic wavelength for each chemical element. Electrons passing through atoms are decelerated by Coulomb force which generates braking x-ray radiation, also called 'Bremsstrahlung'. Braking radiation increases the background, and its intensity decreases with the incoming electrons' energy. Electrons located in the valence or conduction orbitals absorb a smaller amount of energy and are ejected from the shell, so-called secondary electrons (SE). SE originate from the surface layers of the sample; therefore, the SE electrons are useful for imaging surface morphology.

Electron microscopy was performed using the TESCAN, Mira I LMH. Electrons produced by the Schottky field emission gun are accelerated by an application of the high voltage (up to 30 kV); the path and diameter of an electron beam are adjusted by the system of electromagnetic lenses. A microscope is equipped with the SE and BSE detectors, which collect information on the topography and atomic contrast of the sample [51]. X-rays emitted during the relaxation of electrons from the inner shells unambiguously identify the chemical elements, and the intensity of respective peaks shows their relative content in the sample. To analyse the characteristic x-ray radiation from the sample, the energy dispersive Bruker AXS x-ray detector (EDX), which transfers incoming photons to an electrical current-voltage signal, is installed. The EDX signal is collected and processed using Esprit software [53].

2.4 Specific heat

Thermodynamical properties of the sample can be effectively studied using specific heat measurements. Specific heat is defined as the amount of heat Q supplied to the unit mass of the sample in order to increase the temperature of the sample by 1 K. The character of the thermodynamical process of the increase in temperature can be described by the parameter that remains constant. In the case of constant specific volume V , the expression for specific heat C_V is written as

$$C_V = \left(\frac{\delta^2 F}{\delta T^2} \right) = T \left(\frac{dS}{dT} \right)_V, \quad (2.6)$$

where F stands for the Helmholtz free energy, and dS denotes the entropy of the system. The derivative of F and S is performed under constant volume V . The standard specific heat measurement is performed under constant pressure, and the isobaric specific heat C_p is obtained. The difference between C_p and C_V can be expressed as $C_p - C_V = \frac{9\alpha^2 TV_m}{\kappa}$, where κ is the isothermal compressibility, α stands for an isobaric thermal expansivity and V_m denotes the molar volume at constant pressure. Generally, C_V is taken for a good approximation of C_p , especially below 100 K (see [54]).

Specific heat consists of conduction electrons, lattice, magnetic and nuclear contributions. The contributions dominating the higher temperatures are the lattice vibrations, phonons. In the condensed matter system consisting of n different atoms, phonon modes can be divided into three linearly k -dispersing acoustic and $3n-3$ optical phonon branches. The Einstein model of optical phonons supposes the vibration of the lattice as a set of harmonic oscillators contrary to the Debye model of acoustic phonons, which considers the sample as a continuous vibrating elastic body with a maximum number of vibration modes represented by the Debye frequency ω_D and Debye temperature Θ_D connected via the relation $\Theta_D = \frac{\hbar\omega_D}{k_B}$. The low-temperature specific heat has a cubic dependence on temperature and can be consistently described by the Debye model: $C_{ph} = \beta T^3$, where $\beta = \frac{1944.3}{\Theta_D}$ [55]. At high temperatures, the value of specific heat based on 1 mole of matter tends to reach the Dulong-Petite limit of $3nR$, reflecting the number of moles n and the universal gas constant R .

Free electrons are considered to interact with a periodically arranged lattice of positively charged ions. Since the electrons are fermions, the electrons occupy energies from the lowest to the highest, Fermi energy E_F . The Fermi energy is connected to the Fermi temperature T_F defined as $E_F = k_B T_F$ [55]. Increasing temperature the electrons near Fermi edge are excited in the ratio proportional to T/T_F and C_{el} can be described as $\frac{1}{2}\pi^2 N k_B^2 \frac{T}{T_F} = \gamma T$, where the Sommerfeld coefficient γ reflects the density of the electrons on the Fermi surface.

In materials containing ions with a magnetic moment, the magnetic specific heat C_{mag} reflects the ordering of magnetic ions in the lattice and CEF contributions. With increasing temperature, the population of higher energetic levels is reflected in the increase of magnetic specific heat described by the Schottky contribution, C_{Schott} . The analytical expression for C_{Schott} was derived as follows:

$$C_{Schott} = k_B N_A \left(\frac{\sum_{i=1}^l \left(\frac{E_i}{k_B T} \right)^2 e^{-\frac{E_i}{k_B T}}}{\sum_{i=1}^l e^{-\frac{E_i}{k_B T}}} - \left(\frac{\sum_{i=1}^l \frac{E_i}{k_B T} e^{-\frac{E_i}{k_B T}}}{\sum_{i=1}^l e^{-\frac{E_i}{k_B T}}} \right)^2 \right), \quad (2.7)$$

where the summation goes over the number of magnetic ion energy levels l with energy E_i . The change in entropy ΔS connected to the population of energy levels is derived as

$$\Delta S = R \ln(l) \quad (2.8)$$

for 1 mole of matter.

Determining C_{mag} allows us to calculate the magnetic entropy $S_{mag}(T)$ via a relation

$$S_{mag}(T) = \int_0^T \frac{C_{mag}(T')}{T'} dT' + S_0, \quad (2.9)$$

where S_0 is a constant with the entropy value at $T = 0$ K and according to the third law of thermodynamics is zero.

The experimental realization of the specific heat measurement was done using the Physical Properties Measurement System (PPMS), Quantum Design. For thermodynamic measurements $A_2Ir_2O_7$ polycrystals were cold-pressed into the solid pellets. Apiezon grease was employed to maintain good thermal contact between the sample and measurement device (so-called puck, where the sample is installed on the measuring platform) [56]. The heater supplies a specific amount of heat while the thermometer monitors the actual temperature development during the heating and cooling process. The accessible experimental temperatures range from 330 to 0.4 K. While temperatures down to 1.8 K are achieved using ^4He gas, the use of He^3 option with ^3He isotope enables the sample to cool to 0.4 K. The measurement is performed under high vacuum condition; therefore, the thermalization of the prevailing system is conducted through thin wires connecting the platform and the thermal bath; for the measurement, the time-relaxation method was employed.

2.5 Magnetization measurement

Magnetic properties of the sample can be effectively investigated by magnetization measurement, which is defined as a total magnetic moment per unit volume \mathbf{M} . To measure the magnetic response, an external magnetic field of induction \mathbf{B} is applied. Magnetic induction is connected to the magnetic field intensity \mathbf{H} through the relation $\mathbf{B} = \mu_0 \mathbf{H}$ where μ_0 is the permeability of the vacuum. Assuming the linear response of the system, the magnetic susceptibility $\overset{\leftrightarrow}{\chi}$ is defined as [55]

$$\mathbf{B} = \mu_0(\mathbf{H} + \mathbf{M}) = \overset{\leftrightarrow}{\chi} \mathbf{H}. \quad (2.10)$$

Considering the expressions from the section 1.1, the magnetic properties can be derived under some simplifying assumptions. In the system of magnetic moments in thermal equilibrium with the reservoir at temperature T , magnetization can be expressed as a function of field and temperature

$$M(H, T) = \frac{N}{V} g \mu_B J B_J \left(\frac{g \mu_B J H}{k_B T} \right), \quad (2.11)$$

where the $B_J(x)$ stands for *Brillouin function* and is defined as $\frac{2J+1}{2J} \cotgh\left(\frac{2J+1}{2J}x\right) - \frac{1}{2J} \cotgh\left(\frac{1}{2J}x\right)$. Combining the definition of susceptibility 2.10

and the relation for the magnetization 2.11 the susceptibility of non-interacting system is written as

$$\chi = \frac{M}{H} = \frac{g^2 \mu_B^2 J(J+1) N}{3k_B T} \frac{N}{V} = \frac{\mu_{\text{eff}}^2 N}{k_B T V} \equiv \frac{C}{T}. \quad (2.12)$$

The relation defines a Curie constant C and the effective magnetic moment $\mu_{\text{eff}} = g\mu_B \sqrt{J(J+1)}$. The paramagnetic susceptibility 2.12 is positive and field-independent. It decreases with increasing temperature as the thermally driven disorder of magnetic moments grows.

A simple approach to model a system with magnetic interactions is the *mean field theory* also known as *molecular field approximation* [57]. The idea of this approach is to approximate the two-ion interaction by the effective single-ion therm. The expression for the magnetization is enriched by the additional term H^{Eff} reflecting the effective field

$$M_{MF} = \frac{g^2 \mu_B^2 J(J+1) N}{3k_B T} \frac{N}{V} (H + H^{\text{Eff}}). \quad (2.13)$$

The magnetic susceptibility of the system described by the relation 2.13 is written as

$$\chi_{MF} = \frac{g^2 \mu_B^2 J(J+1) N}{3k_B T} \frac{N}{V} \left[1 - \frac{J(J+1) \mathcal{J}(\mathbf{q})^{\text{ex}}}{3k_B T} \right]^{-1} \equiv \frac{C}{T - \Theta_p}, \quad (2.14)$$

which is called the Curie-Weiss law. $\mathcal{J}(\mathbf{q})^{\text{ex}}$ denotes the sum of the exchange integrals $\sum_{i,j} J_{ij}^{\text{ex}} e^{-i\mathbf{q} \cdot (\mathbf{R}_i - \mathbf{R}_j)}$ over the i, j moment couple. Due to the magnetic interactions below Θ_p , a Curie temperature, the spontaneous magnetic ordering is expected. The system with ferromagnetic interactions is characterised by the positive value of Θ_p and the divergence of χ when approaching Θ_p . Antiferromagnetic interactions are characterised by the negative value of Θ_p and the paramagnetic susceptibility of the form

$$\chi_{MF} = \frac{C}{T + |\Theta_p|}. \quad (2.15)$$

Θ_p derived for the antiferromagnetic Néel sublattice is connected with the maximum value of the exchange integral $\mathcal{J}(\mathbf{q})^{\text{ex}}$ and its negative value prevents the paramagnetic χ_{MF} to diverge at Θ_p . The use of the mean field analysis for compounds with a localized character of magnetic ions, such as rare-earth-based compounds, is relevant and gives the information of prevailing magnetic correlations and ordering temperatures.

Experimental realization of the $M(H, T)$ measurement was performed using the Magnetic Properties Measurement System, Quantum Design (MPMS7) [58]. The fundamental unit in the MPMS machine is the superconducting quantum interference device (SQUID) [59]. The sample moves through a system of superconducting detection coils, which are connected to the SQUID with superconducting wires. The magnetic moment of the moving sample induces an electric current in the detection coils, which is converted to the sample magnetization signal.

In order to study magnetic moments on the AIAO iridium domain walls (see section 4.6), the isothermal magnetization $M(H)$ was measured under three different cooling protocols: i) zero-field cooled measurement (ZFC) where the

sample is cooled in zero external field from 200 K (well above any magnetic transition in $A_2\text{Ir}_2\text{O}_7$) down to the target temperature, the $M(H)$ loop is measured from 0 T to 7 T, down to -7 T and up to 0 T. ii) 7 T field cooled measurement (7 T FC), characterised by an application of 7 T field at 200 K and cooling of the sample down to target temperature. Measurement is done in the same way as for ZFC regime. iii) -7 T field-cooled loop (-7 T FC) is the same as ii), but the field of -7 T is applied at 200 K.

2.6 Inelastic neutron scattering

Neutron scattering was proven to be a valuable technique for the study of structure, dynamics, and also magnetism in condensed matter systems. Neutrons are characterised by the zero electric charge and magnetic moment of $1.0419 \cdot 10^{-3} \mu_B$ [60]. Neutron radiation is scattered directly by the sample nuclei, which is governed by strong interaction as an acting force. The magnetic moments of neutrons reflect the magnetic moments of sample electrons via dipole-dipole interaction; thus, crystallographic and also magnetic structures can be revealed. The wavelength of neutron radiation is determined by its energy. For thermal neutrons ($\sim 10^2$ meV [48]), the wavelength reaches $\sim 10^{-10}$ m, which fits perfectly with the interatomic distances in condensed matter systems.

According to the energy transfer in the experiment, two kinds of neutron scattering techniques can be distinguished. Once the kinetic energy of incoming and outgoing neutrons is equal, the experiment is called elastic scattering. The elastic events provide information about both crystallographic and magnetic structures, and short-range correlations can also be identified. While neutrons have no excitable degrees of freedom and the sample target is massive in comparison with individual neutrons, the conservation of neutron kinetic energy also implies the conservation of target kinetic energy. In the case of energy transfer between neutrons and the studied sample, a variety of excitation processes in the target can be studied.

Neutron is characterised by its wave vector \mathbf{k} and spin state σ , which can be omitted in the case of an unpolarized neutron beam. The neutron energy is given by the relation $E = \frac{\hbar^2 k^2}{2m_n} = \frac{m_n v^2}{2}$, where m_n is the neutron mass and v its velocity. Neutron scattering on the sample involves the transfer of energy and momentum between the neutron and the target, and it is governed by the energy and momentum conservation rules [48]:

$$\hbar\omega = E_i - E_f = \frac{\hbar^2}{2m_n} (k_i^2 - k_f^2) \quad (2.16)$$

and

$$\mathbf{Q} = \mathbf{k}_i - \mathbf{k}_f. \quad (2.17)$$

A difference between wave-vectors of the incoming neutron \mathbf{k}_i and scattered neutron \mathbf{k}_f is known as a scattering vector \mathbf{Q} .

Interaction of the neutrons and the target can be treated within the perturbation theory [18] considering the stationary interaction of a neutron with the nucleus and with an electromagnetic field. The interaction potential causes the change of the neutron wave vector; however, the potential is considered to be

weak; thus, the final state of the neutron+target does not differ from the initial state (first Born approximation, [18]).

Neutron scattering experiments can be analyzed by introducing the cross-section σ . A total cross-section is the probability of the neutrons being scattered by the target irrespective of any direction and energy changes. In the case of scattering by the particular nucleus, σ equals to πb^2 , where b denotes the scattering length characteristic for a given isotope (tabulated values can be found in [61]). The experimental conditions restrict the detection of a neutron scattered in the given direction, which is expressed by a solid angle Ω , the scattering can then be described by the differential cross-section $\frac{d\sigma}{d\Omega}$. Also, the energy of the scattered neutrons should be considered; the differentiation of the cross-section with respect to energy leads to the general formula for the partial differential cross-section [48]

$$\frac{d^2\sigma}{d\Omega d\omega} = \frac{k_f}{k_i} \overline{b^2} S(\mathbf{Q}, \omega), \quad (2.18)$$

which expresses the probability that a neutron will be scattered into the solid angle $d\Omega$ within the energy interval dE (the equivalence of the neutron energy E and the frequency ω is used, 2.16). In the equation 2.18 the scattering event is divided into the part dependent on the particular neutron wavelength (the $\frac{k_f}{k_i}$ factor) and the part dependent only on the physical properties of the system under study $S(\mathbf{Q}, \omega)$, the scattering function. It is useful to describe the differential cross-section for certain important experimental cases. The coherent neutron scattering events without energy transfer represent neutron diffraction as described in the previous section 2.2.

Besides the investigation of the crystal structure, neutron diffraction also offers a possibility to study magnetic structures. Neutron magnetic scattering is governed by the dipole-dipole interaction; two terms can describe the interacting potential: the interaction between the neutron magnetic field and the electron current produced by the orbital motion of electrons and the interaction of the neutron magnetic moments with a spin of electrons. The magnetic scattering event is characterised by the magnetic differential cross-section [48]

$$\frac{d^2\sigma}{d\Omega d\omega} = \frac{k_f}{k_i} (\xi r_0)^2 S_{mag}(\mathbf{Q}, \omega), \quad (2.19)$$

where (ξr_0) expresses the strength of a dipolar interaction and equals 1.384 fm. The magnetic structure factor $S_{mag}(Q, \omega)$ can be obtained as [48]

$$S_{mag}(Q, \omega) = \frac{1}{2\pi} \int_{-\infty}^{\infty} dt e^{-i\omega t} \langle \mathbf{M}_{\perp}^*(-\mathbf{Q}, 0) \cdot \mathbf{M}_{\perp}(\mathbf{Q}, t) \rangle. \quad (2.20)$$

Magnetic interaction operator $\mathbf{M}(\mathbf{Q}, t)$ is the Fourier transform of the total (spin and orbital) magnetic density, due to the character of the interaction just the magnetic moments perpendicular to the wave vector transfer \mathbf{Q} contribute to the scattering, which is expressed by the index \perp .

Neutron scattering is an irreplaceable tool for the investigation of sample excitation spectra. The excitations of the single-site lattice particle are successfully treated by inelastic neutron scattering. Those excitations are, for example, crystal field excitations, lattice vibrations or spin-orbit transitions. The use of the

perturbation theory, considering the expression 2.20 and matrix element of the crystal field acting on a magnetic ion multiplet, the inelastic magnetic scattering cross-section reads [48]

$$\frac{d^2\sigma}{d\Omega d\omega} = \frac{k_f}{k_i} (\xi r_0)^2 f^2(\mathbf{Q}) e^{-2W} \sum_{m,n,\alpha} p_n \left(1 - \left(\frac{Q_\alpha}{Q} \right)^2 \right) \cdot |\langle \Gamma_n | \widehat{J}^\alpha | \Gamma_m \rangle|^2 \delta(\hbar\omega + E_n - E_m). \quad (2.21)$$

Magnetic scattering form factor $f(\mathbf{Q})$ is the Fourier transform of the normalized magnetic density; it decreases with increasing modulus of the scattering vector \mathbf{Q} . The polarization factor $1 - \left(\frac{Q_\alpha}{Q} \right)^2$ indicates that just the component of the magnetic fluctuations perpendicular to scattering vector \mathbf{Q} are detected. In the case that ω is a positive quantity, neutrons lose energy during the scattering process, and the system is excited from the initial state Γ_n to the final state Γ_m . The difference between Γ_m energy E_m and the Γ_n energy E_n equals to $\hbar\omega$ and the probability of the initial state thermal population is denoted by p_n . The measurement of the inelastic neutron scattering thus provides a possibility to unambiguously determine the crystal field potential with the proper use of the magnetic ion wave function Γ_n .

Inelastic neutron scattering experiments were performed using the MARI time-of-flight spectrometer at Rutherford Appleton Laboratory (ISIS) [62]. The experiment on $\text{Er}_2\text{Ir}_2\text{O}_7$ carried out on ~ 6 g samples with incident neutron energies, E_i , of 10, 30, 120, and 180 meV at temperatures 5, 60, 100, and 200 K. INS on $\text{Tm}_7\text{Ir}_2\text{O}_7$ and $\text{Lu}_7\text{Ir}_2\text{O}_7$ were performed on samples with a mass of ~ 6 g at temperatures of 5 and 100 K with incident energies of 30 and 180 meV. With E_i of 120 meV, temperatures of 5, 100, and 200 K were measured. Samples were packed in aluminum foil in an annular geometry, and placed inside an aluminum cylindrical sample holder with a diameter of 4 cm. Auxiliary measurements of an empty container and vanadium for calibration purposes were performed. Data were corrected for container scattering, absorption and selfshielding, detector efficiency variation, and energy dependence. Normalization to a vanadium standard allowed calculation of the dynamic structure factor $S(Q, \omega)$ in absolute units, employing the software package MANTIDPLOT [63].

2.7 AC-susceptibility

Applying a DC magnetic field and subsequent measurement of the sample response provide information on the equilibria sample magnetization. The dynamical properties of the magnetic moments can be investigated by measurement of the response to an external AC magnetic field. Generally, the external magnetic field has the form

$$H = H_{DC} + H_{AC} \cos(\omega t) \quad (2.22)$$

which contains both a static component H_{DC} and time-dependent field with the amplitude H_{AC} and frequency $\omega = 2\pi f$, the static external field is zero. The AC susceptibility then probes the ground state magnetic excitations due to the typically low value of the H_{AC} amplitude. Under the assumption of the

linear response of the system, the oscillating response χ_{AC} is defined analogously to the χ in the previous section 2.5 as

$$\chi_{AC} = \frac{M_{AC}}{H_{AC}}. \quad (2.23)$$

Magnetic moments in the sample are excited by the applied oscillating field, the thermodynamic equilibrium of the moments is restored after the relaxation time τ . The sensitivity of the χ_{AC} measurement to the magnetic relaxation is determined by the relation between the frequency of the external field ω and relaxation of the system τ .

First, the case of $\omega \gg 1/\tau$ characterises the regime of the DC susceptibility limit in which the system responds instantaneously to the AC field. Moments have enough time to exchange their energy with the lattice and the *isothermal* susceptibility χ_T is measured [64]. The opposite limit case $\omega \ll 1/\tau$ describes the situation when the perturbation field oscillates too quickly for the magnetic moments to respond. The exchange with the lattice does not thermalize the excited moments, and the detected susceptibility is called *adiabatic*, χ_S .

The comparable values of the oscillating magnetic field ω and the relaxation time of the system $1/\tau$ enable to detect a more complex response. In the intermediate regime, the χ_{AC} response consists of two components: the real χ'_{AC} and the imaginary χ''_{AC} parts. The χ_{AC} is then a complex number

$$\chi_{AC} = \chi'_{AC} + i\chi''_{AC}. \quad (2.24)$$

χ'_{AC} stands for the in-phase response to the perturbation, whereas the off-phase χ''_{AC} results from the difference between the frequency of the perturbation field and the relaxation frequency of the system.

The general relation for the system with the linear response to the external perturbation connects the real and imaginary parts of the response function χ_{AC} by the Kramers-Kronig relations [65]

$$\chi'_{AC} = \frac{1}{\pi} P \int_{-\infty}^{\infty} \frac{\chi''_{AC}(\omega')}{\omega' - \omega} d\omega', \quad (2.25)$$

$$\chi''_{AC} = -\frac{1}{\pi} P \int_{-\infty}^{\infty} \frac{\chi'_{AC}(\omega')}{\omega' - \omega} d\omega', \quad (2.26)$$

where P denotes a Cauchy principal value of the integral in order to avoid the singularity. In the limiting cases of $\omega = 0$ and $\omega = \infty$ the χ''_{AC} vanishes, and χ_{AC} reaches its isothermal and adiabatic value, respectively.

The experimental realization of the AC susceptibility measurement was performed using the homemade extension of the PPMS device with the ACMS option. The puck for measurement consists of the primary coil, which generates the alternating magnetic field; a signal from the sample is detected as a change of the secondary coil voltage. For better measurement precision, the secondary coil is split into two parts with opposite windings and a sample placed in the centre of one part. The frequencies from 1 to 10^5 Hz can be measured and the device can be used with the He³ option.

2.8 Muon spin resonance

Muon spin resonance (μ SR) technique is a powerful microscopic tool for the investigation of various aspects of magnetism. Positively charged muons are implanted into the matter; interaction with the local magnetic field is reflected in the change of the muon spin direction. Therefore, a character of the spatial distribution and dynamics of the magnetic field present in the sample can be detected by muon decay measurement.

A positively charged muon μ^+ is an elementary particle which belongs to the second generation of leptons with a mass of $1.88 \cdot 10^{-28}$ kg, electric charge of e , spin of $1/2$ and the lifetime τ_μ of 2.1969 s [60]. Although μ^+ are produced in a variety of high energy collisions of particles, μ SR experiments require muons that will stop at the studied sample. The low-energy muons are the products of the decay of pions π^+ with a lifetime of $26 \cdot 10^{-9}$ s [60], which are the results of proton collisions with the target made of light elements (carbon or beryllium). The products of the weak pion decay are μ^+ and muon neutrino. Due to the parity violation in the weak interaction, the muon spin is polarized oppositely to its momentum; thus, the muon beam arriving at the sample is 100% polarized.

Muon decay is accompanied by the emergence of muon neutrino ν_μ , positron neutrino ν_{e^+} and positron e^+ . The quantitative treatment of muon decay is based on the measurement of the probability of positron emission per unit of time as a function of solid angle and energy. Considering the preferential positron emission in the direction of the muon spin and the weak interaction which governs the decay, the angular distribution of the emitted positrons $d\Gamma$ into the solid angle $\Omega = \sin(\Theta)d\Theta d\phi$ is written as [66]

$$d\Gamma = \frac{1}{4\pi\tau_\mu} \left(1 + \frac{1}{3} \cos(\Theta) \right) d\Omega. \quad (2.27)$$

The number of positrons $N_{e^+}(t)$ emitted at time t during the decay of $N_\mu(0)$ muons in the interval dt detected over the full solid angle $d\Omega$ is expressed as

$$N_{e^+}(t) = \Gamma N_\mu(t) = -\frac{dN_\mu}{dt} = \frac{1}{\tau_\mu} N_\mu(0) e^{-\frac{t}{\tau_\mu}}. \quad (2.28)$$

Introducing the average beam polarization $\mathbf{P}(t)$ and the position vector \mathbf{n} of the positron detector together with the combination of equations 2.27 and 2.28 leads to the expression of the detected positrons

$$N_{e^+}(t) = B + N_0 (1 + A_0 \mathbf{P}(t) \cdot \mathbf{n}), \quad (2.29)$$

where B stands for the background contribution, the starting intensity of positrons N_0 accounts for the energetical effectivity of detectors. A_0 represents the asymmetry term of the positron emission which can be lower than the theoretical limit of $\frac{1}{3}$. The time evolution of the scalar product of $\mathbf{P}(t)$ and \mathbf{n} contains information about the interaction between muons and the investigated material.

In basic time-differential measurement, the time between muon implantation and positron production is measured. The opposite backward and forward detectors with position vectors \mathbf{n}_B and \mathbf{n}_F are installed around the sample. Considering the equation 2.29, both detectors contain the same information except for

the antiparallel vectors \mathbf{n}_B and \mathbf{n}_F . Therefore, the μ SR signal can be obtained combining the backward and forward raw signals as follows:

$$A_0P(t) = \frac{N_B(t) - N_F(t)}{N_B(t) + N_F(t)}. \quad (2.30)$$

The resulting histogram consists of the positron counts versus the time spent by the muons in the sample. Decay of the average positron counts is caused by a finite muon lifetime; an anisotropy of the muon decay is reflected by the shortage or excess of events on the opposite detectors. The key to understanding the properties of the sample is the analysis of the muon relaxation function.

An important parameter of the μ SR experiment is the character of the muon source. The muon sources for the condensed matter experiment can be divided into two categories according to the time structure of the particle accelerator: pulsed and continuous.

The μ SR experiment was performed using a MUSR spectrometer at Rutherford Appleton Laboratory (RAL, ISIS), Didcot [67]. The synchrotron source at ISIS produces a pulsed muon beam with a structure of 100 ns, and a repetition rate of 50 Hz [68]. When the muons arrive at the sample in the group, the individual detection of the muons is not possible. However, the measurement of all decayed positrons at once permits higher measurement statistics. The time resolution of the experiment in the pulsed beam is restricted by the width of the pulse. Zero-field and longitudinal-field (up to 3 kG) were performed on ~ 2.5 g of polycrystalline sample packed in a standard μ SR Ag plate sample holder with a small amount of dilute GE-varnish for improved thermalisation and covered with an Ag foil. Measurements in the range $2.5 \text{ K} < T < 240.0 \text{ K}$ were performed in a Variox, He exchange cryostat, while a ^3He sorption cryostat was used for measurements in the range $0.3 \text{ K} < T < 20.0 \text{ K}$. The asymmetry was corrected for detector efficiencies and sample-environment attenuation using a high-temperature TF20 (transverse field, 20 G) measurement, separately for each cryostat setup.

Muon spectroscopy was also conducted on the GPS spectrometer at the Paul Scherrer Institute, Switzerland, with the continuous muon beam produced by the cyclotron [69]. The beam time microstructure is determined by the electrical field switching of the frequency 50 MHz. The bunch of muons is produced every 20 ns; however, considering the pion lifetime (26 ns [60]), the muon rate on the beamline can be considered as continuous. The time resolution of the experiment is given by the quality of the detectors and electronics and is significantly higher than in the case of the pulsed beam experiment. The background contribution to the measurement is $\sim 1\%$ of the signal within the time window of 10 μs contrary to the pulsed beam experiments, which are essentially background free in the 20 μs time window.

3. Previous results

3.1 Crystal structure of $A_2\text{Ir}_2\text{O}_7$

$A_2\text{Ir}_2\text{O}_7$ family of compounds, where A stands for the rare-earth ion, is part of a broad family of mixed oxides $A_2B_2\text{O}_7$ with B being the p - or d - element. The crystal structure of most of $A_2B_2\text{O}_7$ was identified as cubic and described with the space group n. 227, $F d \bar{3} m$, the structure of mineral pyrochlore [1]. The stability of the pyrochlore structure, however, strongly depends on the ratio between the A and B ionic radii. The $A_2B_2\text{O}_7$ compounds with $r_A/r_B < 1.48$, that is compounds with $A = \text{Dy} - \text{Yb}$ and $B = \text{Zr}, \text{Hf}$ or Pb , have been found to crystallize in a defect fluorite structure (n. 225, $F m \bar{3} m$), combination of heavy rare-earth ions and $B = \text{Zr}, \text{Hf}$ or Pb , while the counterparts with $r_A/r_B > 1.78$ adopt the layered perovskite structure $P 2_1$ ($B = \text{Ti}, \text{V}$ or Ge). Moreover, the preparation conditions play a significant role and can lead to structure polymorphism as described in the case of, e.g., $\text{Gd}_2\text{Zr}_2\text{O}_7$ [70] or $\text{A}_2\text{Hf}_2\text{O}_7$ [71]. Focusing on the subject of present thesis, all $A_2\text{Ir}_2\text{O}_7$ compounds crystallize in the $F d \bar{3} m$ structure, which is illustrated in Figure 3.1.

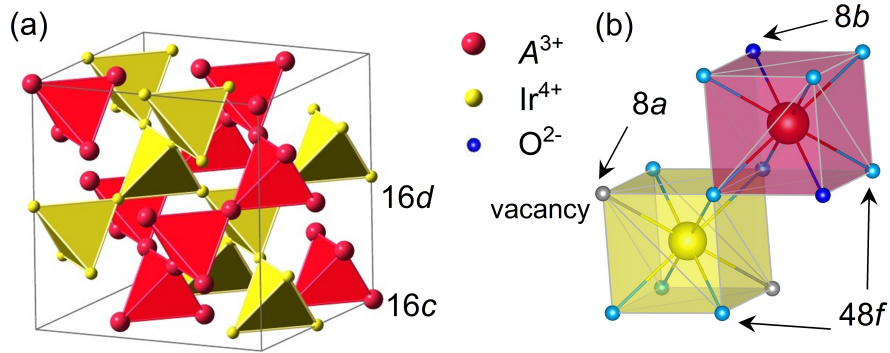


Figure 3.1. Crystal structure of $A_2\text{Ir}_2\text{O}_7$ compounds. a) The rare-earth (red) and iridium (yellow) sublattices arranged in the corner-sharing tetrahedra sublattices, oxygen ions are not shown for better clarity. b) The oxygen surrounding of the rare-earth and iridium ions. Two crystallographic positions of the oxygen ions are denoted as dark (8b) and light (48f) blue, the virtual oxygen vacancy site 8a is depicted as well (grey symbols).

A and Ir cations are ordered parallel to the $\langle 110 \rangle$ direction separated by $(\frac{1}{2}\frac{1}{2}\frac{1}{2})$ with respect to the origin. For the space group $F d \bar{3} m$ and origin choice 2, A and Ir ions occupy (000) 16c and $(\frac{1}{2}\frac{1}{2}\frac{1}{2})$ 16d Wyckoff positions, both forming the net of corner-sharing tetrahedra and both having the $3m$ site symmetry. The rare-earth ions are surrounded by oxygen anions on $(\frac{3}{8}\frac{3}{8}\frac{3}{8})$ 8b and $(x, \frac{1}{8}\frac{1}{8})$ 48f positions, forming cubic cages around A . The octahedral surrounding of the Ir ions consists of six 48f oxygens. The virtual oxygen 8a position is displayed for completeness as it well demonstrates one of the main differences between $F m \bar{3} m$ and $F d \bar{3} m$ structures. Cubic and octagonal oxygen cages are generally not perfect as the free parameter x of the 48f oxygen site differs from the ideal value of 0.375. It is supposed to have a crucial impact on the physical properties of $A_2\text{Ir}_2\text{O}_7$

materials. The fraction coordinate x characterises the distortion of the local Ir environment; the elongation ($x < x_{id}$) or compression ($x > x_{id}$) of the octahedron along $\langle 111 \rangle$. However, the trigonal symmetry of the iridium surrounding is preserved. All $A_2\text{Ir}_2\text{O}_7$ reveal the compression of the oxygen octahedra around the iridium (x ranges from 0.33 to 0.35). The lattice parameter a ranges from 10.1 to 10.4 Å depending on the rare-earth element [1, 72, 73]. A weak evolution of a and x within the $A_2\text{Ir}_2\text{O}_7$ series, that is, the crystal structure and related symmetries are preserved, allows to systematically investigate electronic and magnetic properties of pyrochlore iridates dependent primarily on the A^{3+} ion.

An inherent frustration of both A and Ir tetrahedrons' sublattices has a significant impact on the magnetic properties, as described in section 1.4. The frustration of magnetic moments can suppress the magnetic ordering down to low temperature, which could lead to strongly correlated spin-liquid states or frozen spin-ice states with possible fractionalization of magnetic moments. The competition of the frustration and magnetic correlations predicts the emergence of exotic electronic states in the pyrochlore iridate family, which are briefly introduced in the following section.

3.2 Electronic states in $A_2\text{Ir}_2\text{O}_7$

In $A_2\text{Ir}_2\text{O}_7$ pyrochlores, coexistence of geometrical frustration of both A and Ir magnetic sublattices, the effect of SOC, exchange, and dipolar interaction give rise to a plethora of exotic electronic phenomena. The competition between the spin-orbit coupling and Coulomb correlations generates topologically nontrivial states [74] as was introduced in the section 1.2. The exchange between A - Ir spins could drive an unusual magnetic order of A moments or significantly affect electrical properties of compounds. The coexistence of the listed physical phenomena puts the investigation of iridate pyrochlores at the forefront of scientific interest, resulting in dozens of publications.

High-temperature electronic properties of $A_2\text{Ir}_2\text{O}_7$ range from the metallic behaviour of light rare-earth ($A = \text{Pr} - \text{Sm}$) over weakly metallic ($A = \text{Eu} - \text{Tb}$) to a non-metal state of heavy rare-earth members. With decreasing temperature an abrupt increase in resistivity is observed below T_{Ir} with the exception of $\text{Pr}_2\text{Ir}_2\text{O}_7$, which remains metallic down to the lowest temperatures [11]. T_{Ir} increases steeply from 30 K for $\text{Nd}_2\text{Ir}_2\text{O}_7$ to 120 K in the case of $\text{Eu}_2\text{Ir}_2\text{O}_7$ [8]. A weak increase of T_{Ir} is found in the heavy rare-earth end of the $A_2\text{Ir}_2\text{O}_7$ series [9, 10, 75].

Observed increase of resistivity below T_{Ir} is accompanied by a characteristic feature in the magnetization data, where the zero field-cooled and field-cooled magnetization curves bifurcate [8, 9, 10, 75]. The ferromagnetic nature of correlations between Ir moments is disproved by the absence of the magnetic hysteresis, pointing rather to the antiferromagnetic type of ordering. The emergence of magnetic ordering in $A_2\text{Ir}_2\text{O}_7$ was also suggested by the μSR experiments for $A = \text{Nd}$ [76], Eu [77], Sm [76] and Yb [10].

Presence of iridium magnetic ordering below T_{Ir} was proven by neutron scattering experiments in the case of $A = \text{Lu}$ and Yb [13], $\text{Tb}_2\text{Ir}_2\text{O}_7$ [16], $\text{Eu}_2\text{Ir}_2\text{O}_7$ [78] and $\text{Nd}_2\text{Ir}_2\text{O}_7$ [79]. Magnetic structure was described by $\mathbf{k} = (0, 0, 0)$ propagation vector and all-in-all-out (AIAO) antiferromagnetic ordering. Ordered magnetic

moments of iridium ions point all in or all out from the tetrahedra along a local $\langle 111 \rangle$ axis, (Figure 1.3 in section 1.4). A reduced value of the ordered Ir moment ($\sim 0.5 \mu_B$ for $\text{Yb}_2\text{Ir}_2\text{O}_7$ [13]) was ascribed to additional short-range correlations between iridium moments. A presence of short-range correlations was further supported by the analysis of the entropy related to the iridium transition for $A = \text{Nd}, \text{Sm},$ and Eu , which showed a significantly reduced value in comparison with the expectation for $S = 1/2$ state [8].

A phenomenon closely related to the arrangement of iridium moments concerns the behaviour of domain walls. Ordering of iridium ions on the pyrochlore lattice can be realized by the AIOA or AOAI domains. Topology-based considerations predict the domain interface to host a nontrivial conducting state [80]. Indeed, an experimental study of local magnetometry on $\text{Nd}_2\text{Ir}_2\text{O}_7$ confirmed the presence of metallic domain walls coexisting with the insulating bulk state [81]. The magnetization and resistivity studies of $\text{Eu}_2\text{Ir}_2\text{O}_7$ and $\text{Lu}_2\text{Ir}_2\text{O}_7$ showed a small vertical shift of isothermal magnetization and resistivity curves below the T_{Ir} depending on the sign of an applied field [75, 82]; the emergence of the ferromagnetically coupled spin layer on the AIAO/AOAI domain boundaries was suggested to explain an asymmetric magnetic behaviour.

Introduction of magnetic ions on A sublattice increases the complexity of the $A_2\text{Ir}_2\text{O}_7$ magnetic structure with possible $A - \text{Ir}$ coupling. Neutron study of $\text{Nd}_2\text{Ir}_2\text{O}_7$ found an AIAO ordering of Nd ions below 10 K [79], which was also supported by the μSR experiment revealing a ferromagnetic interaction between Ir-Nd [76]. The ordered moment of Nd ion was found to be reduced to $\sim 1/2$ with respect to the expected value, which was ascribed to the quantum fluctuations of Kramer's doublet ground state. Based on the μSR study of $\text{Sm}_2\text{Ir}_2\text{O}_7$, the development of the long-range ordering of Sm moments was identified below 10 K, and an antiferromagnetic coupling between Sm and Ir ions was inferred [76]. The entanglement of the rare-earth and iridium sublattices was further documented in the case of $\text{Tb}_2\text{Ir}_2\text{O}_7$ with Ir moments ordered into AIAO with concomitant AIAO ordering of Tb moments at 125 K and a second XY component of Tb moment ordering at 10 K [16]. It indicates that the ordering of the Ir sublattice is not influenced by the Tb sublattice at around T_{Ir} , but rather the opposite.

Low-temperature properties of $A_2\text{Ir}_2\text{O}_7$ reflect the interactions between rare-earth ions and also the influence of $A - \text{Ir}$ coupling. The exceptional case of spin-liquid candidate $\text{Pr}_2\text{Ir}_2\text{O}_7$ does not reveal any sign of magnetic ordering down to 70 mK [11], the iridium electrons remain conducting and the Ising-like Pr moments partially freeze at 120 mK due to the strong frustration. The ground state of $\text{Yb}_2\text{Ir}_2\text{O}_7$ results from competing interactions between magnetic ions and strong planar single-ion anisotropy of Yb, leading to the partially ordered ferromagnetic state with the reduced magnetic moments of Yb ions [13]. The iridium analogues of the titanium-based spin ice compounds $\text{Dy}_2\text{Ir}_2\text{O}_7$ and $\text{Ho}_2\text{Ir}_2\text{O}_7$ reveal a fragmented monopole crystal state consisting of the partially ordered Dy and Ho moments in the AIAO structure and other component of magnetic moments remaining dynamic in the 2-in-2-out Coulomb phase [14, 15].

4. Experimental results

4.1 Synthesis and characterisation of $A_2\text{Ir}_2\text{O}_7$

In this section, the preparation of $A_2\text{Ir}_2\text{O}_7$ iridate is illustrated on the case of $\text{Er}_2\text{Ir}_2\text{O}_7$, the representative of a heavy rare-earth member of the series. Preparation routes of solid-state reaction, hydrothermal synthesis, and flux growth were employed. Products were characterised using x-ray diffraction, electron microscopy and analysis of characteristic radiation spectra, for details see sections 2.2 and 2.3. The optimized synthesis process was successfully used for the preparation of other heavy rare-earth $A_2\text{Ir}_2\text{O}_7$ polycrystals. The results of this chapter were recently published in papers [83, 84].

4.1.1 Solid-state synthesis of $\text{Er}_2\text{Ir}_2\text{O}_7$

Based on previous studies (see e.g. [8, 85, 86]), $\text{Er}_2\text{Ir}_2\text{O}_7$ has initially been prepared by a standard solid state reaction. The starting materials, Er_2O_3 and IrO_2 powders (AlfaAesar, declared purity of 99.99%) were dried separately under active vacuum at a temperature of 200°C to remove moisture. The starting oxides were then weighted to obtain the molar ratio $\text{Er}_2\text{O}_3:\text{IrO}_2 = 1:2$, and subsequently mixed in an agate mortar and inserted into a platinum crucible, which was placed into the resistance super-kanthal furnace. The free surface of the mixture in the platinum crucible was in direct contact with air.

The initial reaction of 5 g sample was conducted in the air for 12 hours at temperatures ranging from 300 to 1200°C with a step of 100°C. The reacted sample was reground to better homogenize the products and reactants and improve the reaction conditions in the next step. A portion of the sample was separated for analysis by x-ray diffraction at each stage. The analysed sample was subsequently mixed again with the rest of the reactants and treated at a higher temperature. Repeating this process, ten diffraction patterns were collected. The diffraction patterns and fits to the model structure(s) are presented in Figure 4.1.

Patterns measured at 300°C consist solely of contributions from the initial oxides (and Ir). High intensity peaks corresponding to Er_2O_3 (space group $Ia\bar{3}$, n. 206, $a = 10.559(1)$ Å) are clearly pronounced. On the other hand, the patterns of the iridium oxide have a rather amorphous character; the broadness of the observed peaks reflects the size of grains of the IrO_2 nano-powder. Moreover, already at such a low temperature as 300°C, a decomposition of IrO_2 (space group $P4_2/m\bar{2}m$, n. 136, $a = 4.499(3)$ Å, $c = 3.155(1)$ Å) to Ir and O_2 (and/or other volatile iridates) is observed – the reflections corresponding to elemental iridium ($Fm\bar{3}m$, n. 225, $a = 3.8409$ Å) are observed at a number of 2θ positions (41.0°, 47.2° or 69.0°). The sum of mole fractions of Ir and IrO_2 in the sample is 65(3)%, nearly the expected value for the initially stoichiometric sample.

When increasing the temperature to 400°C, broad peaks of the IrO_2 phase become more pronounced (see Figure 4.1a), while the rest of the peaks change negligibly. IrO_2 peaks gradually sharpen as the temperature increases to 900°C. Following the development of IrO_2 reflections at 28, 34 and 69°, and using the Scherrer formula for crystallite size [87], the evolution of IrO_2 grains is followed:

4.6(2), 5.5(2), 15.2(7), 38(2), 46(2), 50(3) and 64(5) nm for 300, 400, 500, 600, 700, 800 and 900°C. Although the specific numbers represent only a lower bound to crystallite size, as the formula does not account for a wide range of defects or mechanisms that can broaden reflections, the trend of increasing the coherently scattering grain size with increasing-temperature thermal treatments is clearly evident.

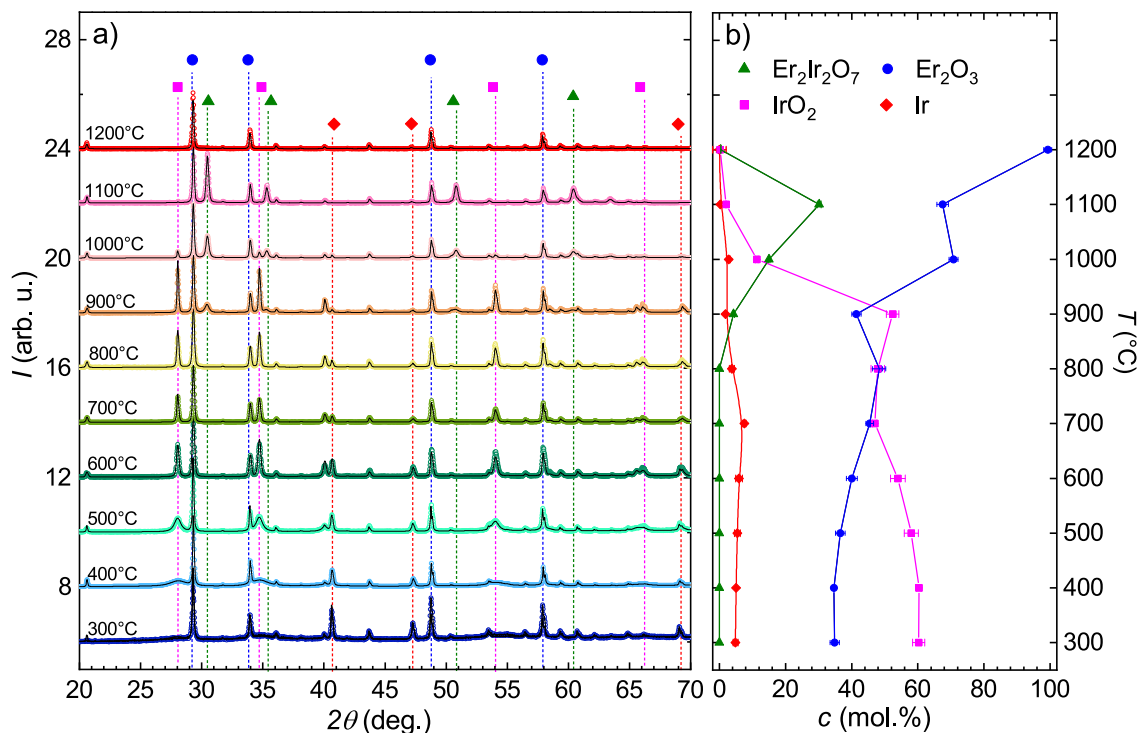
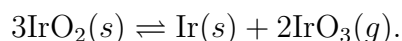


Figure 4.1. Synthesis of $\text{Er}_2\text{Ir}_2\text{O}_7$ by solid state reaction. a) x-ray diffraction patterns collected after each solid state reaction cycle at given temperature and corresponding Rietveld fits (black lines). Individual phases are marked by symbols: $\text{Er}_2\text{Ir}_2\text{O}_7$ (green triangle), IrO_2 (purple square), Er_2O_3 (blue circle) and Ir (red diamond). The guiding lines of respective colours are provided as well. b) relative phase composition, c , derived by Rietveld fitting of x-ray diffraction patterns. The lines connecting individual concentration points are guide to eye.

The mole fraction of iridium oxide decreases slightly when comparing the sample at 500°C and 600°C (see Figure 4.1b). As the fraction of Er_2O_3 increases while no $\text{Er}_2\text{Ir}_2\text{O}_7$ phase is formed, the loss of $\text{IrO}_2(s)$ can be attributed to the known disproportionation and the loss of volatile iridium oxides ([88]) according to the relation



(s) and (g) symbols denote the solid and gaseous phases, respectively. The mole-fraction sum of iridium and iridium dioxide decreases only slowly ($0.03\% \text{ hr}^{-1}$), relative to Er_2O_3 , suggesting that the iridium loss is mainly from the surface layer of the sample (within the Pt crucible). Further increase of temperature leads to a stronger loss of IrO_2 ($2.8\% \text{ hr}^{-1}$). At temperatures above 600°C, the mole-fraction of Ir is seen to decrease and is no longer observable at 1100°C. The decrease is likely due to faster formation of volatile iridium oxides ($\text{IrO}_3(g)$) as well

as through the reaction with $\text{Er}_2\text{O}_3(\text{s})$ to form the $\text{Er}_2\text{Ir}_2\text{O}_7(\text{s})$ product at higher temperatures. At 900°C , the pyrochlore $\text{Er}_2\text{Ir}_2\text{O}_7$ phase is formed and its mole-fraction in the sample is 4.3(3)%, after the 12 hour reaction time. Simultaneously, we did not observe any significant change of IrO_2 patterns, while the Ir peaks became much less intense. A further increase of temperature causes a strong increase of the fraction of $\text{Er}_2\text{Ir}_2\text{O}_7$, and simultaneously an abrupt decrease of IrO_2 in the sample. The reaction is almost completed at 1100°C , when the amount of both IrO_2 and Ir in the sample is 2.3(5)% (Figure 4.1b).

Here, we mention the apparently increasing molar fraction of Er_2O_3 in the sample starting from 34(1) mol.% at 300°C , increasing to 48(2) mol.% at 800°C , just before the $\text{Er}_2\text{Ir}_2\text{O}_7$ phase is formed and then due to the decomposition and evaporation of volatile iridium oxides a final increase to 100% at 1200°C . Such observation, together with knowledge of the high melting temperature and stability of $\text{Er}_2\text{O}_3(\text{s})$ (melting point 2344°C [89]), evidences an equilibrium state between pyrochlore (ternary oxide) and precursory binary oxides, with continuous evaporation of Ir as volatile oxides, even at 1000°C . Finally, at 1200°C the increasing evaporation of the volatile iridium oxides, which are in equilibrium with $\text{Er}_2\text{Ir}_2\text{O}_7(\text{s})$ and $\text{Er}_2\text{O}_3(\text{s})$ causes the eventual complete conversion of $\text{Er}_2\text{Ir}_2\text{O}_7(\text{s})$ back into $\text{Er}_2\text{O}_3(\text{s})$ (and evaporated $\text{IrO}_x(\text{g})$) to maintain the equilibrium condition. Alternatively, one can speculate about the potential evaporation of $\text{Er}_2\text{Ir}_2\text{O}_7$. However, such a scenario is ruled out by the final sample weight: the mass of Er_2O_3 in the initial mixture was, within the error, identical with the mass of resulting 1200°C product.

Besides the phase analysis of incoming and resulting products, $\text{Er}_2\text{Ir}_2\text{O}_7$ pyrochlore phase and its temperature development reflected in the diffraction pattern was investigated. The comparison between pyrochlore peaks formed at 900°C (blue triangles), 1000°C (green circles), and 1100°C (red squares) at various 2θ positions was performed, the (222) and (400) peaks are shown in Figure 4.2a, d). The subtraction of the background and the normalization of the intensity were done to follow the respective peak shape development. For comparison of the pyrochlore phase crystallinity, the model peaks based on the shape parameters refined from LaB_6 x-ray diffraction pattern (black lines) are used. The width of pyrochlore peaks is significantly larger than the standard one leading to the suggestion of a smaller coherently scattering size of $\text{Er}_2\text{Ir}_2\text{O}_7$ crystallites. Using the Debye-Scherrer formula described above, the pyrochlore phase crystallite size can be estimated as follows: 40 nm for the products of 900°C reactions and 50 nm for 1000 and 1100°C .

Another remarkable feature of pyrochlore reflections is their asymmetry. A pseudo-Voigt function or any other symmetric peak shape function cannot successfully model $\text{Er}_2\text{Ir}_2\text{O}_7$ peaks. The difference curves of refined peak shape profile function and measured data of (222) and (400) reflections at various temperatures can be found in Figure 4.2b, e) (blue, green, and red colour correspond to a reaction temperature of 900, 1000 and 1100°C). It should be noted that none of the other phases (Er_2O_3 , IrO_2 or Ir) has any reflection within the investigated 2θ region, and hence the apparent broadening cannot be ascribed to the presence of reflections from those phases. The difference curves are asymmetric with respect to the centre of each peak determined as the maxima intensity 2θ position and shifted to 0 degrees for better comparison. To further analyse the

asymmetric behaviour, the pyrochlore peaks were divided into lower and higher angle parts with the centre determined as a 2θ position with the highest intensity. Then, the right side was fitted by the Lorentz peak shape function (dashed lines of corresponding colours in Figure 4.2e,f), the difference between measured data and the symmetrized peak profile can be found in the bottom parts of Figure 4.2 c), f). An enhanced signal centred at a lower 2θ position can be detected for each reaction temperature. The asymmetry appears in the whole 2θ range; therefore, the effect of axial divergence can be ruled out. Additionally, the intensity of the asymmetric broadening appears to be lowered between 900 and 1000°C but remains constant after the thermal treatment at 1100°C - both evidence suggesting an appearance of additional, pyrochlore-like phase with possible larger lattice constant a . Due to the low intensity of the pyrochlore phase, the additional asymmetric broadening signal statistic does not allow one to estimate the precise value of its lattice constant.

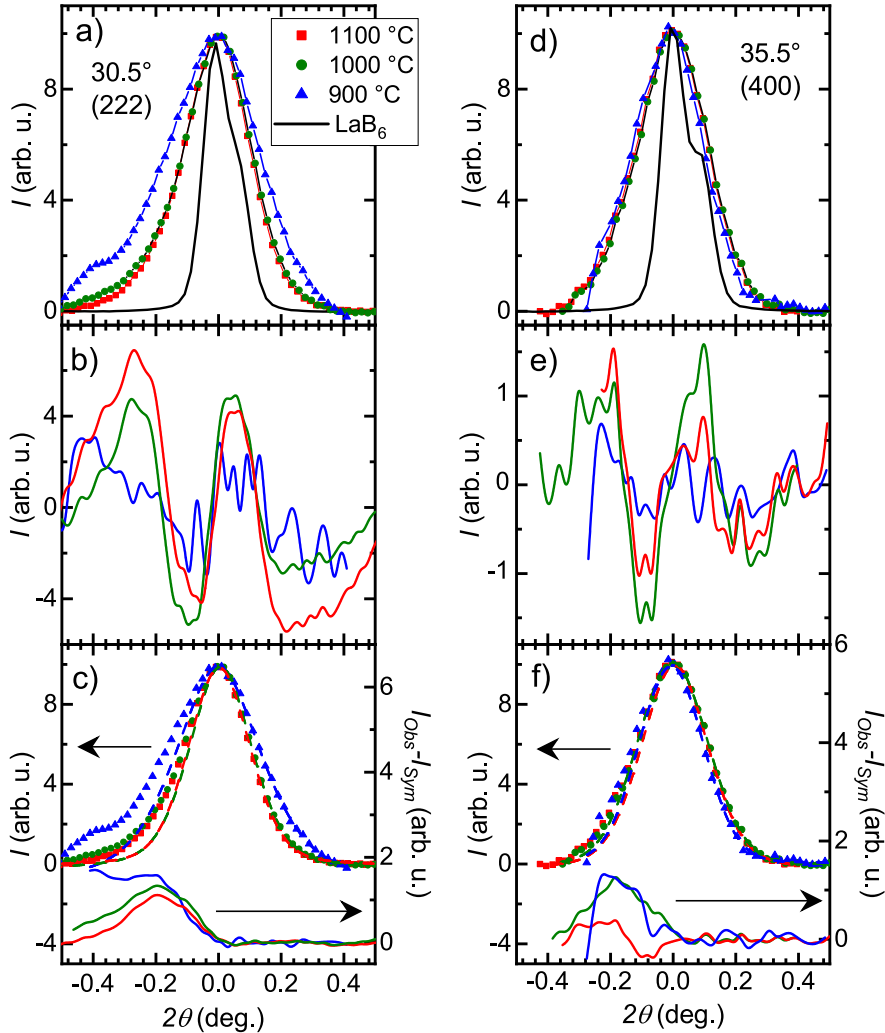


Figure 4.2. *Analysis of diffraction pattern peaks of $Er_2Ir_2O_7$.* (222) and (400) reflections of $Er_2Ir_2O_7$ phase synthesized at 900°C (blue triangles), 1000°C (green circles) and 1100°C (red squares) (a, d). The black lines represent a LaB_6 model peak at respective position. The difference curves ($Er_2Ir_2O_7 - LaB_6$ peaks) are presented in panels b) and e). panels c) and f) contain the symmetrization of the pyrochlore peaks (left axis), which leads to the low-angle tails (right axis).

To explain the low-angle tail of the pyrochlore reflections, a possible higher erbium content in $\text{Er}_2\text{Ir}_2\text{O}_7$ is proposed: Doping of ideal stoichiometric $A_2B_2O_7$ pyrochlore materials by A element addition to $A_{2+x}B_{2-x}O_7$ pyrochlores with partial A occupation of B position is known to be possible (e.g. $\text{Eu}_2\text{Ir}_2\text{O}_7$ [90]). Preparation of single crystalline materials with non-stoichiometric A/B ratio has also previously been established [91]. The possible random occupation of erbium ions of the iridium crystallographic position would lead to an increase of lattice parameter whilst preserving the symmetry of the original $\text{Er}_2\text{Ir}_2\text{O}_7$ pyrochlore lattice. Taking into account the high loss rate of IrO_2 by evaporation of volatile oxides, the distribution of $\text{Er}_{2+x}\text{Ir}_{2-x}\text{O}_7$ compositions is expected to be erbium rich (asymmetric composition variation), rather than a normal distribution about the ideal 2-2-7 composition, resulting in an asymmetric lattice parameter distribution skewed towards larger a . The observation of low-angle pyrochlore tail is in agreement with this scenario.

Utilizing the acquired experience on the solid state reaction, i.e. phase(s) development, $\text{Er}_2\text{Ir}_2\text{O}_7$ formation, IrO_2 decomposition and evaporation, we attempted to optimise the synthesis process. Excess IrO_2 was added to the starting material, and the non-stoichiometric mixture was reacted at 1000°C – the temperature, at which $\text{Er}_2\text{Ir}_2\text{O}_7$ is formed and the decomposition of $\text{Er}_2\text{Ir}_2\text{O}_7$ is reasonable low. A mixture of IrO_2 and Er_2O_3 in the 2.1:0.9 molar ratio was repeatedly reacted for 12 hours in air. After each reactive cycle, the sample was thoroughly mixed by grinding, and the x-ray diffraction patterns were collected.

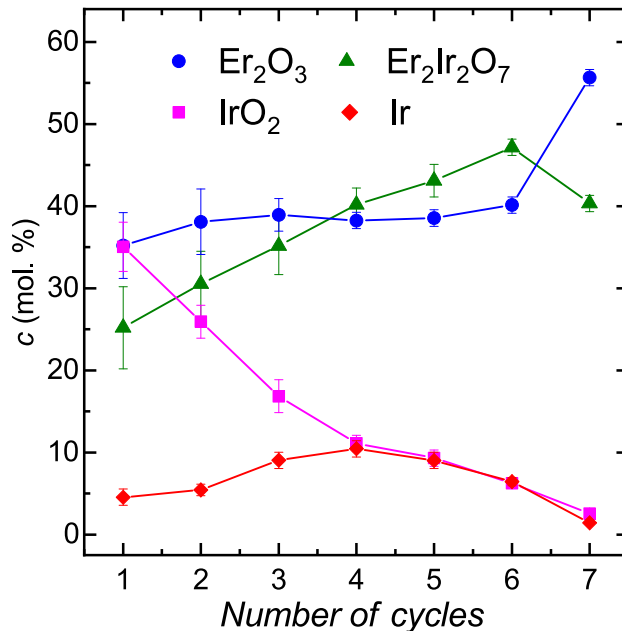


Figure 4.3. *Products of solid state reaction with excess of IrO_2 .* The development of the relative phase concentration c of the mixture of initial oxides Er_2O_3 and IrO_2 with their molar ratio 0.9 : 1.1 repeatedly reacted at 1000°C . $\text{Er}_2\text{Ir}_2\text{O}_7$, Er_2O_3 , IrO_2 and Ir are labelled with green triangles, blue circles, purple squares and red diamonds, respectively.

The pyrochlore phase was already formed during the first cycle with 25(3) mol.% (see Figure 4.3). Besides the formation of the pyrochlore phase,

partial decomposition of IrO_2 is also followed in the diffraction patterns. Further thermal cycling led to an increase of the $\text{Er}_2\text{Ir}_2\text{O}_7$ mole fraction, and further decomposition and reduction of IrO_2 . By cycle 6, almost all the IrO_2 oxide was reacted/decomposed, and the $\text{Er}_2\text{Ir}_2\text{O}_7$ fraction was maximal (48.2(7) mol.%). Additional thermal cycles did not improve the sample, but instead a decomposition of the previously prepared $\text{Er}_2\text{Ir}_2\text{O}_7$ is evidenced by the relative increase of the Er_2O_3 fraction in the sample. Turning attention again to the peak shapes (representative (222) and (400) reflections shown in Figure 4.4), the observed asymmetry is pronounced and similar to the results seen with stoichiometric solid state reaction (Figure 4.2). A subtle development of the low-angle tail is followed through a number of thermal cycles.

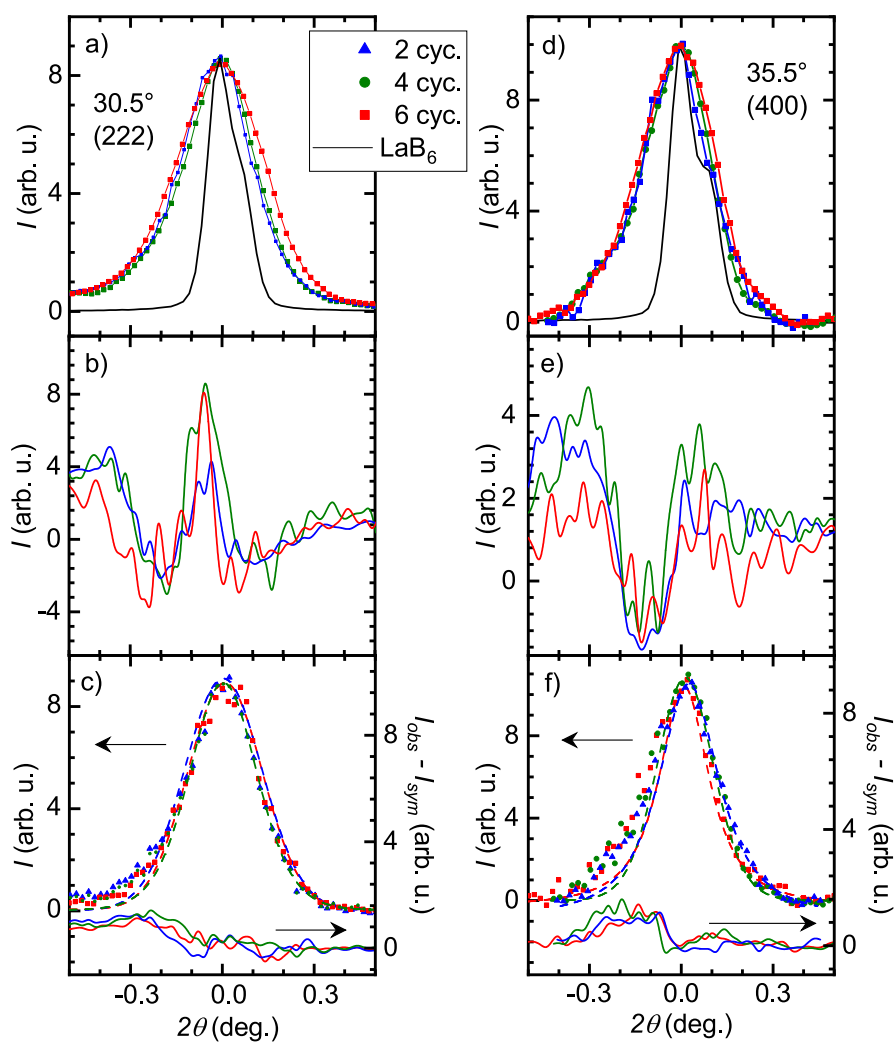


Figure 4.4. *Diffraction peaks of $\text{Er}_2\text{Ir}_2\text{O}_7$ prepared with excess of IrO_2 .* a) (222) and d) (400) reflections of $\text{Er}_2\text{Ir}_2\text{O}_7$ phase synthesized by solid state reaction at 1000°C after 2 (blue triangles), 4 (green circles) and 6 (red squares) reaction cycles. The black lines represents a LaB_6 standard peak shape. Panels b) and e) show the difference curves from the Rietveld refinement between the data (colours consistent with symbols) and the fitted profile of (222) and (400) peaks. Panels e) and f) contain the symmetrization of the pyrochlore peaks (left y-axis) which leads to the low-angle tails (right y-axis).

The results of solid state synthesis, both through the use of stoichiometric and non-stoichiometric starting mixtures, suggest that phase pure $\text{Er}_2\text{Ir}_2\text{O}_7$ cannot be prepared by this method. Additional IrO_2 in the initial mixture, fine control of reaction temperature and time, careful analysis of the reacted sample, all significantly improved the quality of the final material. However, decomposition of IrO_2 cannot be prevented and the Ir product (although very minor) remains stable up to the temperature at which $\text{Er}_2\text{Ir}_2\text{O}_7$ itself decomposes. Instead of further variations of the conditions for the solid state synthesis, we now turn to its modification – the flux method, as an alternative approach.

4.1.2 Synthesis of $A_2\text{Ir}_2\text{O}_7$ by CsCl flux method

Facing the fact that the solid state reaction of the initial Er_2O_3 and IrO_2 oxides, in both stoichiometric and non-stoichiometric initial mixtures, does not allow a preparation of phase pure $\text{Er}_2\text{Ir}_2\text{O}_7$, a different approach using an inorganic salt as a flux was chosen [9, 92]. The flux mediates the formation of the pyrochlore phase and simultaneously protects the initial/reacted oxides from evaporation. In the previous section it was shown that the solid state reaction of constituting oxides is most efficient at 1000°C , the flux method allows to partially dissolve individual reactants, their diffusion through the flux, nucleation, and subsequent growth of the pyrochlore phase at lower temperature.

To properly map the synthesis, we started again with a stoichiometric mixture of Er_2O_3 and IrO_2 initial oxides and CsCl flux in a 1:2:50 ratio, respectively. The mixture was placed into an open platinum crucible. The reaction time was 12 hours and the temperature for individual reaction cycles increased from 700°C to 1000°C . After each reaction cycle, the CsCl salt was cleared from the sample by dissolution in water and the powder was collected by centrifuging.

At 700°C , the mixture of initial oxides was converted into a matt black powder containing relatively large ($\sim\text{mm}$) shiny pieces (see inset II of Figure 4.5). The EDX analysis revealed no traces of erbium signal in these large crystals, only Ir and O were detected. Indeed, single crystal x-ray diffraction confirmed the crystal structure to be tetragonal, with respective lattice parameters corresponding to IrO_2 phase ($a = 4.497(5) \text{ \AA}$, $c = 3.152(2) \text{ \AA}$). To unambiguously confirm the synthesized single crystals are purely IrO_2 , the sample was divided into two parts depending on particle size (using a $40 \mu\text{m}$ sieve), and investigated by powder x-ray diffraction. The analysis showed a high amount of IrO_2 with good crystallinity in the courser part. The finer portion contained a significantly lower amount of iridium dioxide and the diffraction patterns were dominated by $\text{Er}_2\text{Ir}_2\text{O}_7$ and Er_2O_3 contributions. A small amount of Ir (from IrO_2 decomposition) was also observed.

The reaction cycle at 800°C did not improve the pyrochlore phase content in the sample, see Figure 4.6. The ratio between the mole fraction of Er_2O_3 and IrO_2 remained unchanged with increasing temperature. Further increase of reaction temperature significantly reduced the amount of initial oxides. However, besides the single $\text{Er}_2\text{Ir}_2\text{O}_7$ phase, another cubic phase with slightly larger lattice parameter was observed (open symbols in Figure 4.6). Although an asymmetric peak shape in solid state reaction suggests a continuous composition variation (see discussion above for SSR samples 4.1.1), by high-temperature flux a new, dis-

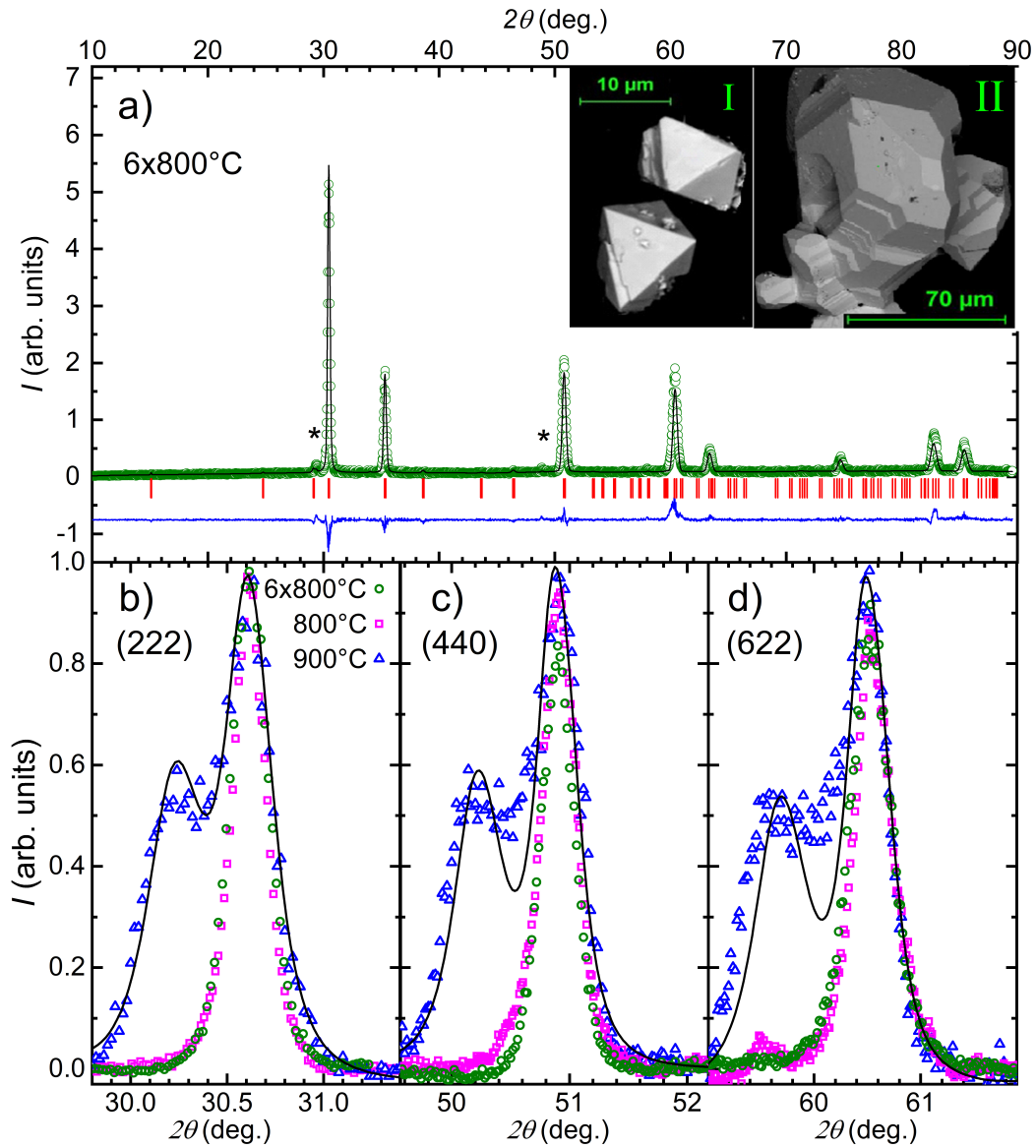


Figure 4.5. $Er_2Ir_2O_7$ prepared by *CsCl flux*. a) the powder x-ray diffraction pattern of $Er_2Ir_2O_7$ prepared by CsCl flux method after six reaction cycles at 800°C , asterisks indicate traces of unreacted Er_2O_3 . The insets I and II comprise BSE images of the pyrochlore phase prepared at 800°C and the crystal of IrO_2 grown at 700°C , respectively. Panels b - d) contain zoomed in pyrochlore diffraction peaks (222), (440) and (622) measured on samples reacted at 800°C , 900°C and 6-times at 800°C , black line represents the Rietveld refinement of sample reacted at 900°C considering two pyrochlore phases with different lattice parameter a .

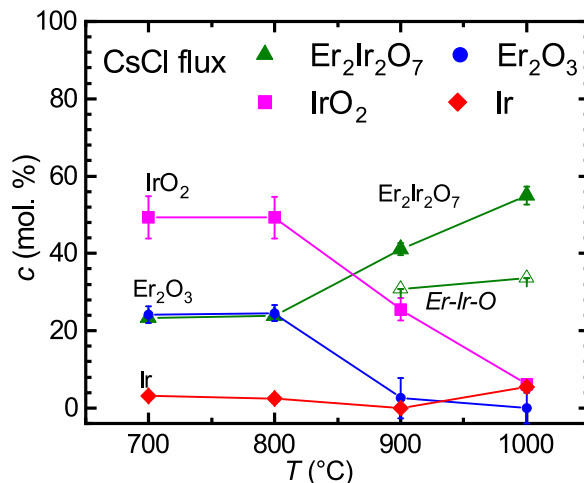


Figure 4.6. Products of $Er_2Ir_2O_7$ CsCl flux growth. Development of relative mole fraction, c , of individual phases reacted in CsCl flux depending on temperature.

tinct set of reflections indicates a discrete secondary *Er-Ir-O* phase (or stabilised x -range in the $Er_{2+x}Ir_{2-x}O_{7+y}$, general formula).

The flux growth at 900°C provided better conditions for the formation of this secondary phase (see Figure 4.5), which can be described by the pyrochlore structure model with broader peaks and larger unit cell ($a = 10.315(5)$ Å). The amount of both the $Er_2Ir_2O_7$ phases reached 72(2) mol.%, while the secondary phase content was 30.8(5) mol.%. It further increased to 33.2(5) mol.% when reacting at 1000°C, while the total amount of $Er_2Ir_2O_7$ reached 90(3) mol.% (see Figure 4.6).

Data quality does not allow refinement of site atomic occupation in this secondary phase; however, a rough estimate of stoichiometry can be obtained using Vegard’s law-type arguments for the $Er_{2+x}Ir_{2-x}O_{7-y}$ series. Using the lattice parameters of $Er_2Ir_2O_7$ ($x = 0$, $a_{Er_2Ir_2O_7} = 10.162(2)$ Å) and Er_2O_3 ($x = 1$, $a_{Er_2O_3} = 10.559(2)$ Å) as series end-members, the estimated stoichiometry of the *Er-Ir-O* phase ($a_{Er-Ir-O} = 10.302(4)$ Å) can be calculated as

$$x_{ErIrO} = \frac{a_{ErIrO} - a_{Er_2Ir_2O_7}}{a_{Er_2O_3} - a_{Er_2Ir_2O_7}} = 0.35,$$

corresponding to an approximate formula $Er_{2.71}Ir_{1.29}O_{6.64}$.

To avoid the formation of the off-stoichiometry secondary pyrochlore phase, the new sample was reacted at 800°C several times. A number of heating and regrinding cycles led to an improvement in the pyrochlore phase content without any traces of the secondary phase. Finally, after six cycles, the pyrochlore phase content reached 94(3) mol.%(see Figure 4.7). The shape of the pyrochlore peaks was also significantly improved (Figure 4.5b-d), as well as the crystallite size: from the initial 20(3) nm increases to 60(3) nm for the last cycle. The amount of Er_2O_3 in the sample was reduced to 6(1) mol.%, and no IrO_2 or Ir was detected in the diffraction patterns (Figure 4.7).

With further heating cycles, the pyrochlore phase content began to decrease, presumably due to the same mechanism seen in the high-temperature solid state

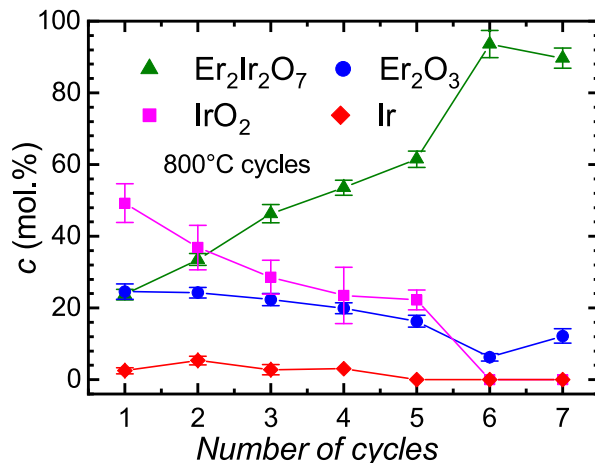


Figure 4.7. *Er₂Ir₂O₇ CsCl flux growth at 800 °C.* Development of relative mole fraction, c , of individual phases reacted in CsCl flux depending on a number of reaction cycles at 800°C.

reaction: a decomposition of the pyrochlore into constituting oxides, with the more volatile iridium oxides evaporated from the surface of the flux, leading to an apparent increase in the fraction of Er₂O₃.

Contrary to the solid state reaction method, with careful control of reaction conditions, the flux method allows preparation of Er₂Ir₂O₇ sample of good crystallinity. A lower temperature of pyrochlore phase formation in CsCl flux greatly reduces the evaporation of IrO₂ and maintains the stoichiometric conditions during crystallization. Also, the flux growth increases the mobility of a reacting particle which improves the homogeneity of the products demonstrated as narrower pyrochlore reflections. Furthermore, the quality of the products was confirmed by EDX analysis, which showed Er:Ir = 1:1 stoichiometry (see Table 4.1).

The chemical behaviour of the other heavy rare-earth A₂O₃ is supposed to be similar to that of erbium oxide. Indeed, our trials to synthesize various A₂Ir₂O₇ employing solid-state reaction did not lead to phase pure samples. On the other hand, the CsCl flux method showed to be successfully used for the preparation of these pyrochlore iridates. Therefore, following the found recipe, initial A₂O₃ and IrO₂ were mixed with CsCl in the molar ratio 1:2:50, inserted into the platinum crucible and flux growth was conducted at 800°C. Repeating the reaction cycles completed the formation of the pyrochlore phase, a small amount (up to 3%) of unreacted A₂O₃ was traced in diffraction patterns (due to the high volatility of IrO₂), see Figure 4.8. We emphasize the synthesis of Tm₂Ir₂O₇, so far unreported member of the series.

X-ray diffraction patterns were fitted to a model pyrochlore structure. Resulting lattice parameters a and free position parameters x (of oxygen, 48*f* Wyckoff position, $(x, 1/8, 1/8)$) for individual A₂Ir₂O₇ are listed in Table 4.1. A development of a and x with A atomic radius is followed: The lattice parameter decreases with increasing atomic number of A , according to expectations (lanthanide contraction of atomic/ionic radius). A substitution of A simultaneously influences interatomic distances, bond-lengths and angles (see section 3). Deformation of oxygen cages is represented by fraction coordinate x slightly increasing in A₂Ir₂O₇

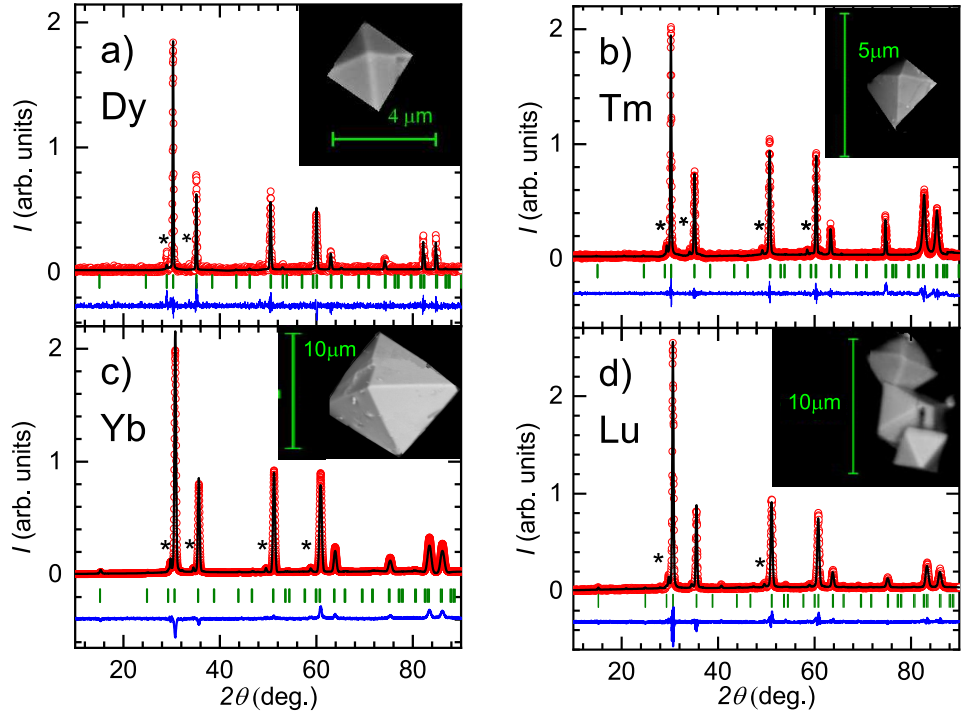


Figure 4.8. *X-ray diffraction patterns of $A_2Ir_2O_7$ prepared by $CsCl$ flux.* Asterisks mark peaks of respective unreacted A_2O_3 oxides. The BSE images of $A_2Ir_2O_7$ crystallites of μm size reveal a typical octahedral shape expected for pyrochlore structure.

with atomic number of A , see Table 4.1; however, x remains significantly lower than x_{id} ($= \frac{3}{8}$ for all investigated analogues. Refined parameters are well in agreement with previously published data on $A_2Ir_2O_7$: $A = Dy$ [14], Ho [8], Er [9], Yb [13] and Lu [75]. $Tm_2Ir_2O_7$ structural parameters fit perfectly into the trend given by the other $A_2Ir_2O_7$ compounds.

Electron scanning microscopy of the prepared samples revealed that the pyrochlore phase consists of μm size single crystals with typical octahedral shape (see BSE images in insets of Figure 4.8). EDX analysis of several single crystalline pieces showed the sample composition to be $A : Ir = 1:1$ within the error of the EDX measurement, similarly to the case of $Er_2Ir_2O_7$ (see Table 4.1). Due to the low sensitivity of the EDX to oxygen, its content could not be determined.

Table 4.1. *Structural parameters and stoichiometry of $A_2Ir_2O_7$.* Structural parameters determined from x-ray diffraction and EDX analysis: crystallographic parameters a and x of $Fd\bar{3}m$ space group (n. 227). Composition ratio $A : Ir$ determined from EDX measurements.

$A_2Ir_2O_7$	Dy	Ho	Er	Tm	Yb	Lu
$a(\text{\AA})$	10.192(1)	10.184(1)	10.162(1)	10.135(1)	10.108(2)	10.104(1)
x	0.334(2)	0.335(2)	0.334(2)	0.337(2)	0.336(2)	0.340(3)
$A:Ir$	50(2):50(2)	50(2):50(2)	50(2):50(2)	50(2):50(2)	51(2):49(2)	51(2):49(2)

4.1.3 Hydrothermal synthesis

Solid state synthesis and flux growth of $A_2Ir_2O_7$ was followed by hydrothermal synthesis technique. Hydrothermal synthesis was introduced in the section 2.1.3, a mixture of initial oxides - together with an aqueous mineralization agent(s) - is closed within a hermetically sealed reaction vessel and thermally treated.

As there is currently no hydrothermal protocol known for the successful hydrothermal synthesis of these iridate pyrochlores, several of the most common mineralizing agents were trialled in both low and high concentrations. These included alkaline solution sources of OH^- (NaOH, KOH), salt sources of F^- and Cl^- (CsCl, NaF, KF), as well as acidic sources of Cl^- , NO_3^- and H^+ (HCl, HNO_3). The maximum available reaction temperature is limited by the softening temperature of PTFE (220°C). As the autoclave isolates the mixture from the outer environment, no loss of constituent elements is expected, compared to the open reaction vessels used in both solid state and flux growth processes. Elevated temperature and pressure in the aqueous environment are expected to increase ion mobility and aid reaction and recrystallization.

A stoichiometric mixture of initial oxides in individual mineralizing agents was reacted at 220°C for 12 days; also, the influence of mineralization process on pre-reacted precursor was used (initial oxides were pre-reacted by CsCl flux at 800°C for 24 hours, as described in the previous section). Although our investigations tested a number of mineralizing agents and a significant amount of time was dedicated to fully uncover the potential of hydrothermal synthesis in the preparation of $A_2Ir_2O_7$, the results (summarized below) do not indicate any direct path to a single $A_2Ir_2O_7$ phase preparation using the tested mineralizing agents.

The first attempt of sample preparation was realized using distilled water without any additional mineralizing agents. The resulting product did not show any trace of the pyrochlore phase, constituting oxides were present, and 16(2) mol.% of additional $Er(OH)_3$ phase was formed. Subsequently, potassium and sodium hydroxides, KOH and NaOH, being the traditional basic mineralizing agents, were attempted. The aqueous solution of the hydroxides with concentrations 1, 4, and 12 M was prepared and introduced into the reaction vessel together with the partially reacted sample. Investigating the x-ray diffraction patterns of the reaction products revealed no improvement in the phase content of $Er_2Ir_2O_7$, but also the presence of $Er(OH)_3$ as an unwanted side product was detected. Its amount increased from 50(2) to 54(2) and finally 56(3) mol.% for 1, 4, and 12 M of KOH, respectively. The situation was similar in the case of NaOH, where no increase of pyrochlore phase was detected in any of NaOH concentrations, the amount of $Er(OH)_3$ was determined to be 42(2), 48(2) and 50(3) mol.% for 1, 4 and 12 M of NaOH.

Based on the successful preparation of pyrochlore iridate using CsCl as a flux, hydrothermal synthesis was also attempted using inorganic salt solutions as the mineralizing agent, trialling cesium chloride (CsCl), sodium fluoride (NaF), and potassium fluoride (KF). Partially reacted initial oxides were sealed in vessels with aqueous solutions of CsCl in concentrations 0.2, 1.0, and 4.0 M, the pyrochlore phase increased by 4(2), 4(2), and 7(3)% with respect to the original phase composition. The reaction with NaF and KF concentrations 1.0 and 4.0 M had a more promising impact, with 20(2) and 25(4)% increase of pyrochlore phase content in the case of KF and 6(2) and 8(2)% for the NaF as a mineralizing agent.

The efficiency of the NaF agent is lower due to the formation of $\text{Er}(\text{OH})_3$, which is present in 6(1), resp. 8(2) mol.% for 1 and 4 M of NaF. However, additional cycles did not lead to any significant reinforcement of the pyrochlore phase content. Finally, we attempted the reaction employing inorganic acids HNO_3 and HCl as mineralizing agents in aqueous solutions: 1, 2 and 4 M with pre-reacted precursor. A slight improvement of 8(1), 10(2) and 10(2)% of the pyrochlore content with respect to precursor phase composition was observed in the case of 1, 2, and 4 M of HNO_3 , and a smaller impact of HCl reaction with 4(1), 6(2) and 7(2)% pyrochlore phase increase for 1, 2 and 4 M of HCl . However, despite a slight increase of pyrochlore phase and partial dissolution of Er_2O_3 oxide, the IrO_2 oxide remained in the sample with the smallest concentration of 20 mol% in the case of 4 M of HNO_3 .

While the initial positive results achieved when using fluoride salts as mineralizing agents for hydrothermal synthesis suggest promise for the method, additional modifications or repeated reaction cycles did not provide a route to a suitably pure sample. However, the reaction of 4 M HNO_3 led to the most significant reduction of the Er_2O_3 parasitic phase; further modification of an acidic mineralizer hydrothermal synthesis may provide a route for the reduction of the high-melting stable erbium oxide which can complement the high-temperature flux growth technique. More extensive reagent and condition testing are necessary for an optimised route to pyrochlore iridates hydrothermal synthesis.

After a variety of preparation experiments with varying degrees of success, the CsCl flux growth method was found to be the most suitable preparation method. Further experiments presented in this work were performed on polycrystals prepared by this route.

4.2 Magnetization and specific heat of $A_2\text{Ir}_2\text{O}_7$

Systematic investigation of a heavy rare-earth part of the $A_2\text{Ir}_2\text{O}_7$ series with $A = \text{Dy}, \text{Er}, \text{Tm}, \text{Yb}, \text{and Lu}$ was performed by means of standard magnetization and specific heat measurements in the temperature range of 0.35 - 300 K. Measurement techniques and equipment are described in sections 2.4 and 2.5. $A_2\text{Ir}_2\text{O}_7$ polycrystals, prepared as described above (section 4.1.2), were cold-pressed and measurements were performed on ~ 10 mg and ~ 1 mg pellets employing He^4 and He^3 options, respectively. Data presented in this section were recently published in [84, 93, 94, 95].

4.2.1 $\text{Lu}_2\text{Ir}_2\text{O}_7$

Magnetic properties of $A_2\text{Ir}_2\text{O}_7$ are determined by the magnetism of Ir and A ions and their possible coupling. To study the development of physical properties within the $A_2\text{Ir}_2\text{O}_7$ series, it is highly advantageous to study Lu analogue first. Lu^{3+} ion does not bear a magnetic moment, and therefore the magnetic properties of $\text{Lu}_2\text{Ir}_2\text{O}_7$ are dictated by Ir^{4+} only. $\text{Lu}_2\text{Ir}_2\text{O}_7$ data can be subsequently used as a 'non-magnetic' counterpart to other $A_2\text{Ir}_2\text{O}_7$ data. Although the properties emerging from the coupling between A^{3+} and Ir^{4+} sublattices cannot be screened, the subtracted data give a solid view on magnetic properties of A - sublattice in other members of the series.

Temperature evolution of magnetization under external magnetic fields of 0.01, 0.05, and 1 T is shown in Figure 4.9. A linear evolution from 300 - 200 K is followed by the bifurcation between zero-field cooled (open symbols) and field cooled (filled symbols) curves at 140 K. A kink in the ZFC data below 140 K (inset of Figure 4.9) together with a change in the slope of the FC curve below the ZFC/FC splitting evidence the iridium sublattice ordering well in agreement with Ref. [72]. A broader maximum in ZFC curves shifts towards lower temperatures with increasing external field, which further supports the antiferromagnetic nature of iridium ordering. The ZFC magnetization between 120 K and 20 K evolves almost linearly contrary to a steep increase of FC magnetization response in the same temperature interval. Below 10 K, both ZFC and FC curves show a strong enhancement of magnetization.

Inverse magnetic susceptibility H/M under an external field of 1 T with the fit to Curie-Weiss law in the temperature interval 200 K - 300 K (black line) is presented in Figure 4.9b). A fit to the Curie-Weiss law leads to a determination of the effective magnetic moment of $\mu_{eff} = 0.88(4) \mu_B$ and the paramagnetic Weiss temperature $\Theta_p = -217(3)$ K. The large negative value of Θ_p strongly supports the antiferromagnetic correlations in the material. Effective moment value is considerably reduced from the expected value of free Ir^{4+} ion ($1.73 \mu_B$) with an effective moment $J_{eff} = 1/2$ and will be discussed below. Isothermal magnetization measurement above and below the magnetic transition showed only a particular increase of magnetic moment in 7 T (see the inset of Figure 4.9b) far below the saturated value of $J_{eff} = 1/2$ state.

Magnetic transition of the iridium sublattice is demonstrated as a broad anomaly in specific heat C_p/T vs. T in Figure 4.10 with an onset at 140 K concomitant with the bifurcation between zero-field and field cooled curves (see Figure 4.9). The position or shape of the anomaly is not affected by an application of the external magnetic field up to 4 T. We note that the previous studies of $\text{Lu}_2\text{Ir}_2\text{O}_7$ [72][75] did not report any kind of specific heat anomalies, which can be explained by the different sample preparation methods. The analysis of the specific heat anomaly by means of the magnetic entropy is presented in the right inset of Figure 4.10. To estimate the magnetic contribution, the data below and above the anomaly were fitted with a polynomial (pink curve) and the subtracted data was integrated. The entropy value $S = 0.57 \text{ J.K}^{-1}\text{mol}^{-1}$ is comparable to the estimated entropy for $\text{Nd}_2\text{Ir}_2\text{O}_7$ ($0.47 \text{ J.K}^{-1}\text{mol}^{-1}$) and is lower than entropy of $\text{Sm}_2\text{Ir}_2\text{O}_7$ ($2.00 \text{ J.K}^{-1}\text{mol}^{-1}$) and $\text{Eu}_2\text{Ir}_2\text{O}_7$ ($1.40 \text{ J.K}^{-1}\text{mol}^{-1}$) [8]. The calculated entropy is much smaller than the value expected for $J_{eff} = 1/2$, $R \ln(2)$, where R stands for an universal gas constant. The $\text{Lu}_2\text{Ir}_2\text{O}_7$ entropy change can be considered to originate purely from electronic contribution to specific heat, the estimation of the parameter $\gamma_{\text{Ir}} = \frac{S}{T_{\text{Ir}}}$ ($T_{\text{Ir}} \sim 140$ K) leads to $\sim 4.1 \text{ mJ.K}^{-2}\text{mol}^{-1}$ and points to a semimetallic behaviour of $\text{Lu}_2\text{Ir}_2\text{O}_7$.

Semimetallic character of $\text{Lu}_2\text{Ir}_2\text{O}_7$ was further evidenced by the analysis of the low-temperature specific heat. Considering the relations introduced in section 2.4 and the absence of magnetic contribution (although Ir contribution is present), the specific heat can be described within the Debye formula

$$C_p = C_{el} + C_{latt} = \gamma T + \beta T^3 \quad (4.1)$$

as a sum of electronic and lattice contributions. The linear fit of C_p/T vs T^2 on the

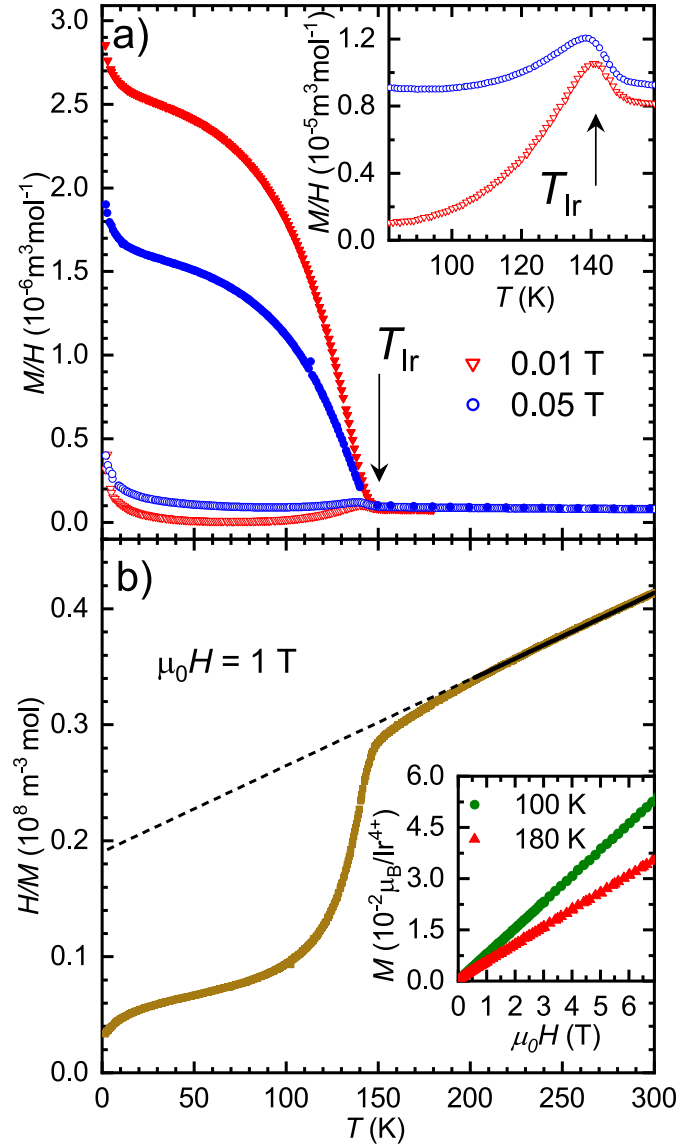


Figure 4.9. *Temperature dependence of magnetization of $\text{Lu}_2\text{Ir}_2\text{O}_7$.* Zero-field cooled (open symbols) and field-cooled (full symbols) magnetization in 0.01 and 0.05 T is presented in panel a). Inset contains details of ZFC magnetization around 140 K. Inverse magnetic susceptibility under an external field of 1 T is shown in panel b). The full black line represents the Curie-Weiss fit to the temperature range 200 - 300 K; the dashed line stands for an extrapolation of the Curie-Weiss fit down to low temperature. An inset of panel b) contains an isothermal magnetization below (100 K) and above (180 K) the temperature of iridium ordering.

left inset in Figure 4.10 leads to the Sommerfeld coefficient $\gamma = 10.2(1) \text{ mJ.K}^{-2}\text{mol}^{-1}$ well in agreement with previously published values [75, 72] and is in agreement with a semimetallic nature of $\text{Lu}_2\text{Ir}_2\text{O}_7$ ground state. Debye temperature ($\theta_D = 350(4) \text{ K}$) calculated from $\beta = 0.50(2) \text{ mJ.K}^{-4}\text{mol}^{-1}$ via expression $\theta_D^3 = 12\pi^4 RN/5\beta$, where $N = 11$ atoms per unit cell, agrees well with previous results on $\text{Lu}_2\text{Ir}_2\text{O}_7$ as well as other $A_2\text{Ir}_2\text{O}_7$ pyrochlores [8, 72, 96].

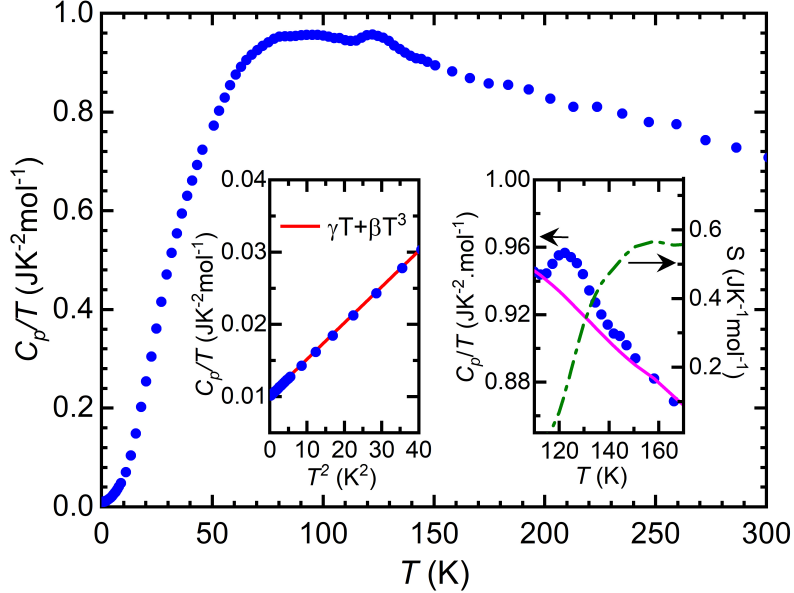


Figure 4.10. *Specific heat of $\text{Lu}_2\text{Ir}_2\text{O}_7$.* The left inset shows a low-temperature evolution of specific heat as C_p/T vs. T^2 with a linear fit (red line) of γ and β parameters. The high- T anomaly around 140 K together with the corresponding entropy (dot-dashed line, right y-axis) is zoomed in the right inset. The pink curve represents the polynomial fit to data above and below the anomaly.

To interpret the thermodynamic measurements of $\text{Lu}_2\text{Ir}_2\text{O}_7$ its electronic structure was calculated using the first-principle density functional theory. Both Lu and Ir ions have a trigonal local symmetry; therefore, it is necessary to use the full potential first-principle methods for accurate electronic properties calculation. The full potential local orbital (FPLO) [97] and full potential augmented plane waves plus local orbital (FPAPW-LO) [98] - WEIN2k code - were employed to solve Kohn-Sham equations. The exchange correlation potential was calculated within the generalized gradient approximation, GGA [99, 100, 101]. The results of structure calculations predict the equilibrium lattice constant less than 0.2% smaller than the experimental value and the minimized oxygen $48f$ position 0.3389 close to the experimental one (see the section 4.1.2 above). The semimetallic ground state of $\text{Lu}_2\text{Ir}_2\text{O}_7$ also follows from the DFT calculations revealing $\gamma_{DFT} = 7.3 \text{ mJ.K}^{-2}\text{mol}^{-1}$ and a small enhancement coefficient $e = \gamma/\gamma_{DFT} - 1.0 = 0.4$, i.e. rather weak electron-phonon interaction. The DOS at the Fermi level and related γ_{DFT} was obtained from relativistic Dirac-Kohn-Sham electronic structure calculations (FPLO code).

Reduction of Ir^{4+} effective magnetic moment μ_{eff} can originate from the frus-

tration of the iridium sublattice or from the itinerant character of $5d$ iridium electrons. A significant amount of iridium-based compounds reveals a μ_{eff} close to the value expected for $J_{eff} = 1/2$ state; however, there are a number of iridium oxides with reduced effective moments, e.g., BaIrO_3 with $\mu_{eff} = 0.276 \mu_B$ [102], weak ferromagnet Sr_2IrO_4 with $\mu_{eff} = 0.5 \mu_B$ [103], $\text{Sr}_3\text{Ir}_2\text{O}_7$ with $\mu_{eff} = 0.69 \mu_B$ having simultaneously very low saturated magnetic moment of $0.04 \mu_B$ [104], insulating antiferromagnet $\text{SrLa}_{10}\text{Ir}_4\text{O}_{24}$ with $\mu_{eff} = 1.11 \mu_B$ [105]. Furthermore, the DFT calculations predict a lower moment on $\text{Lu}_2\text{Ir}_2\text{O}_7$. The spin-polarized scalar relativistic DFT calculations converged to zero spin iridium magnetic moment and to value of $0.308 \mu_B$ with LSDA [99] and GGA [100], respectively (FPLO code). The GGA [101] spin magnetic moment inside Ir sphere is $0.253 \mu_B$, whereas LSDA [99] provides a zero spin magnetic moment (APW+lo code). More details of the $\text{Lu}_2\text{Ir}_2\text{O}_7$ electron structure calculations can be found in our publication [93].

4.2.2 $A_2\text{Ir}_2\text{O}_7$ with $A = \text{Dy}, \text{Er}, \text{Tm}$ and Yb

Inspecting the high-temperature behaviour of $A_2\text{Ir}_2\text{O}_7$, both the magnetization and specific heat data reflect the anomaly caused by the ordering of the iridium sublattice. The splitting between ZFC and FC magnetization curves was found in the case of all analogues at temperature T_{Ir} , which increases from 128 K ($\text{Dy}_2\text{Ir}_2\text{O}_7$) to 143 K ($\text{Yb}_2\text{Ir}_2\text{O}_7$), see Figure 4.11 a - d. The results are well in agreement with the previously published data for $A = \text{Dy}$ [14], Er [9], and Yb [13]. Within the frame of the present work, thulium analogue was synthesised for the first time and the experimental results are published in our paper [84].

ZFC magnetization curves of most iridates reveal a weak anomaly just below the ZFC/FC bifurcation, most notably in the case of $A = \text{Er}$ and Yb and still visible in the case of $A = \text{Dy}$. A similar kink was also observed in the case of lighter rare-earth iridates [3, 8, 10]). Unlike the other compounds, however, the ZFC magnetization of $\text{Tm}_2\text{Ir}_2\text{O}_7$ evolves smoothly in the whole temperature interval. The FC curves of $A = \text{Dy}$ and Er show a step increase with the decreasing temperature, contrary to the case of $A = \text{Tm}$ and Yb where the increase of magnetization is preceded by a bump below the ZFC/FC splitting. The differences could be explained by an interplay between Ir and A sublattices.

Magnetization measurements serve to finalize the phase diagram from [8]. Inspecting the phase diagram, T_{Ir} evolves only slightly with the atomic number of A . The development of T_{Ir} for $A = \text{Sm} - \text{Lu}$ suggests a weak coupling between A and Ir sublattices at temperatures above and around T_{Ir} . On the other hand, the mutual A and Ir interactions are manifested in more complicated case of $\text{Tb}_2\text{Ir}_2\text{O}_7$ where a recent neutron study showed a concomitant ordering of Tb and Ir moments in AIAO structure at T_{Ir} induced by strong Tb - Ir coupling [16]. The second component of Tb moment orders below 10 K, which concludes that rather than iridium sublattice is affected by the rare-earth magnetism, the opposite scenario is more probable, at least at high temperatures. A dominant role of iridium magnetism is also confirmed in the case of $\text{Ho}_2\text{Ir}_2\text{O}_7$ and $\text{Dy}_2\text{Ir}_2\text{O}_7$ compounds, where the AIAO ordering of Ir moments induces the partial ordering of Ho/Dy moments [15, 14]. A weak dependence of T_{Ir} on rare-earth magnetism is clearly demonstrated by the temperature of iridium ordering of non-magnetic $A = \text{Lu}$ and Eu analogues, where T_{Ir} fits into the trend of other rare-earth $A_2\text{Ir}_2\text{O}_7$.

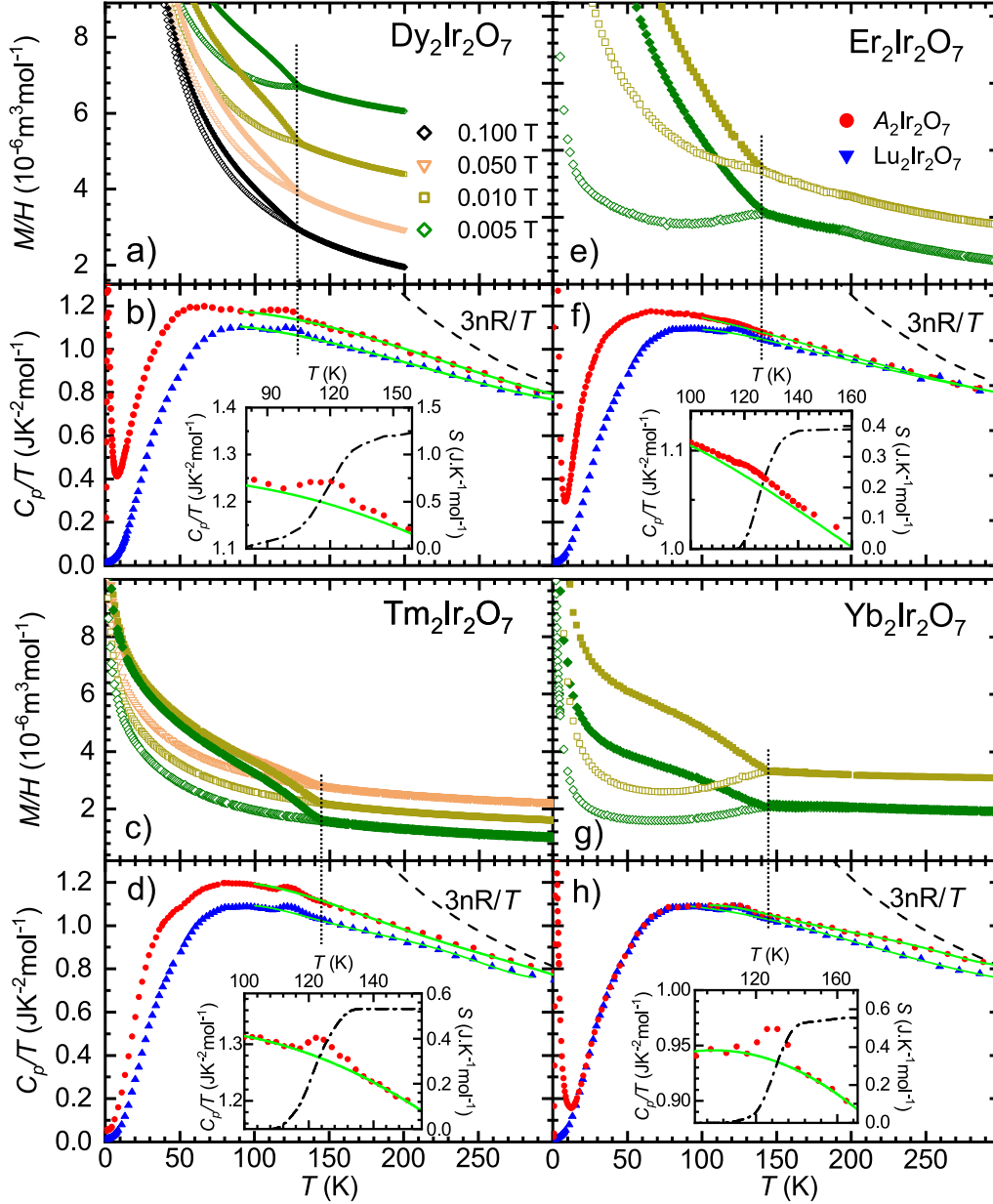


Figure 4.11. *Magnetization and specific heat of $A_2Ir_2O_7$.* ZFC (open symbols) and FC (full symbols) magnetization is presented for selected magnetic fields (a, c, e, g). Specific heat of $A_2Ir_2O_7$ (red circle) and $Lu_2Ir_2O_7$ (blue triangle) is shown in panel b, d, f h. $3nR/T$ limit is depicted in the panels. The insets contain zoomed in specific heat anomaly below T_{Ir} , fit of the data neglecting this anomaly (green line), and entropy connected with the anomaly (dot-dashed line).

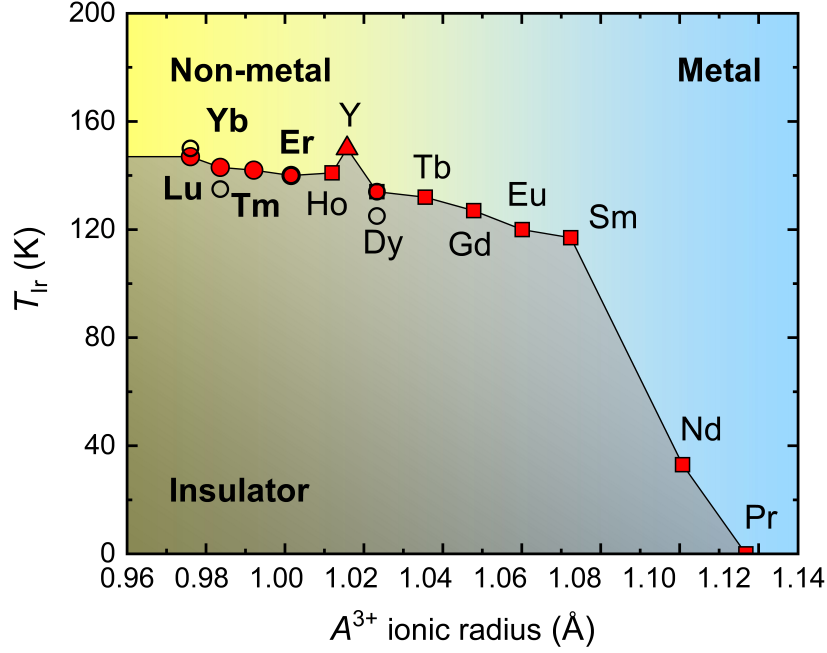


Figure 4.12. *Temperature of Ir ordering in $A_2Ir_2O_7$ dependent on ionic radius of A^{3+} .* Phase diagram from [8] (red squares) was completed by adding so far unreported $Tm_2Ir_2O_7$ and other compounds from present work (red circles). Empty circles represent the T_{Ir} values for respective compounds reported in [9, 13, 14].

$A_2Ir_2O_7$ magnetic susceptibility measured under increasing fields reveals a closing of the ZFC/FC bifurcation eventually results in identical magnetization for both cooling regimes with a linear dependence on temperature well below T_{Ir} , see Figure 4.13 a - d. The temperature dependence of the low temperature susceptibility $M/H(T)$ reveals a difference at T_A (values listed in the Table 4.2) depending on the applied magnetic field in all magnetic $A_2Ir_2O_7$ compounds, see insets in Figure 4.13 a - d. A strongly diverging magnetization in low magnetic fields and low temperatures increases less steeply with increasing magnetic field, and in 7 T, the magnetization is almost saturated. Hence, the magnetic behaviour of $A_2Ir_2O_7$ below T_{Ir} , and more apparently below T_A , is predominantly determined by the magnetism among A^{3+} ions and crystal field acting on them.

The high temperature part of $A_2Ir_2O_7$ inverse susceptibility ($T > 200$ K) was fitted to Curie-Weiss formula (section 2.5 which led to the effective magnetic moment, μ_{eff} , and paramagnetic Curie temperature, Θ_p , listed in the Table 4.2. The effective magnetic moments of $A_2Ir_2O_7$ with $A = Er$ and Tm were found to be close to the value expected for the free rare-earth ions, which agrees well also with the small contribution of iridium sublattice determined from the $Lu_2Ir_2O_7$ measurement. The case of $A = Dy$ and Yb , however, revealed a significantly reduced value of μ_{eff} which was ascribed to the fragmented magnetic state of Dy ions [14] and the competing magnetic phases of Yb ions influenced by the staggered molecular field of the iridium sublattice [13]. The Curie temperature was found negative for all $A_2Ir_2O_7$ pointing to the prevailing antiferromagnetic interactions between magnetic ions.

A subtraction of the $\text{Lu}_2\text{Ir}_2\text{O}_7$ data from the magnetic rare-earth $A_2\text{Ir}_2\text{O}_7$ magnetic susceptibility enabled a partial separation of the iridium sublattice contribution. The difference data were also fitted to the Curie-Weiss formula, which led to the reduced effective moments $\mu_{eff}^{A-\text{Lu}}$ as well as to reduced absolute values of the negative Curie temperature, $\Theta_p^{A-\text{Lu}}$ (values listed in the Table 4.2). However, to interpret the fitted parameters carefully, it is worth taking into account the behaviour of the iridium sublattice in the lutetium analogue. $\text{Lu}_2\text{Ir}_2\text{O}_7$ has the largest negative value of Curie temperature from all studied compounds, the $\text{Lu}_2\text{Ir}_2\text{O}_7$ magnetization data describe just the iridium sublattice contribution, the A - Ir interaction remains unaffected by the subtraction of lutetium analogue and can contribute to $\Theta_p^{A-\text{Lu}}$ values.

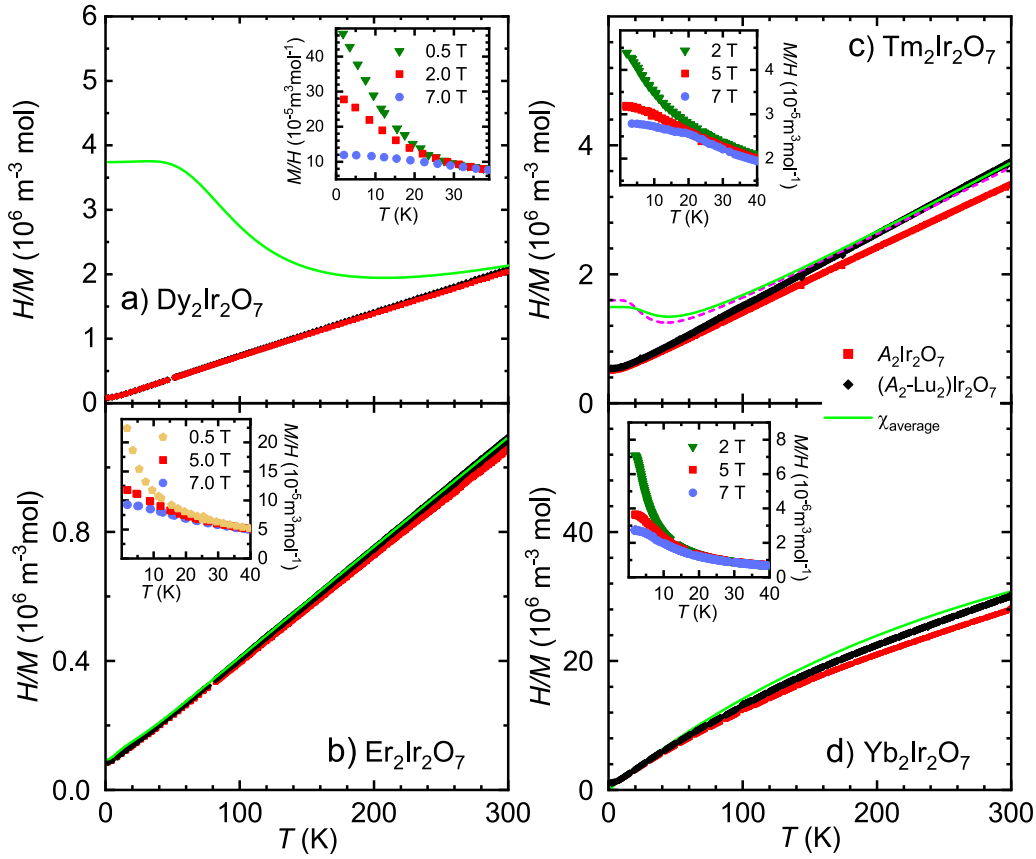


Figure 4.13. Inverse magnetic susceptibility of $A_2\text{Ir}_2\text{O}_7$. $A_2\text{Ir}_2\text{O}_7$ magnetization data (red squares) and the difference $(A_2 - \text{Lu}_2)\text{Ir}_2\text{O}_7$ data (black diamonds) are presented. The averaged inverse susceptibility calculated from CF parameters (green line) is compared to magnetization data. In the case of $\text{Tm}_2\text{Ir}_2\text{O}_7$, also the calculations based on the rescaled CF parameters of erbium analogue are shown (dashed pink line). The insets contain low-temperature $M/H(T)$ data in selected magnetic fields for respective iridates.

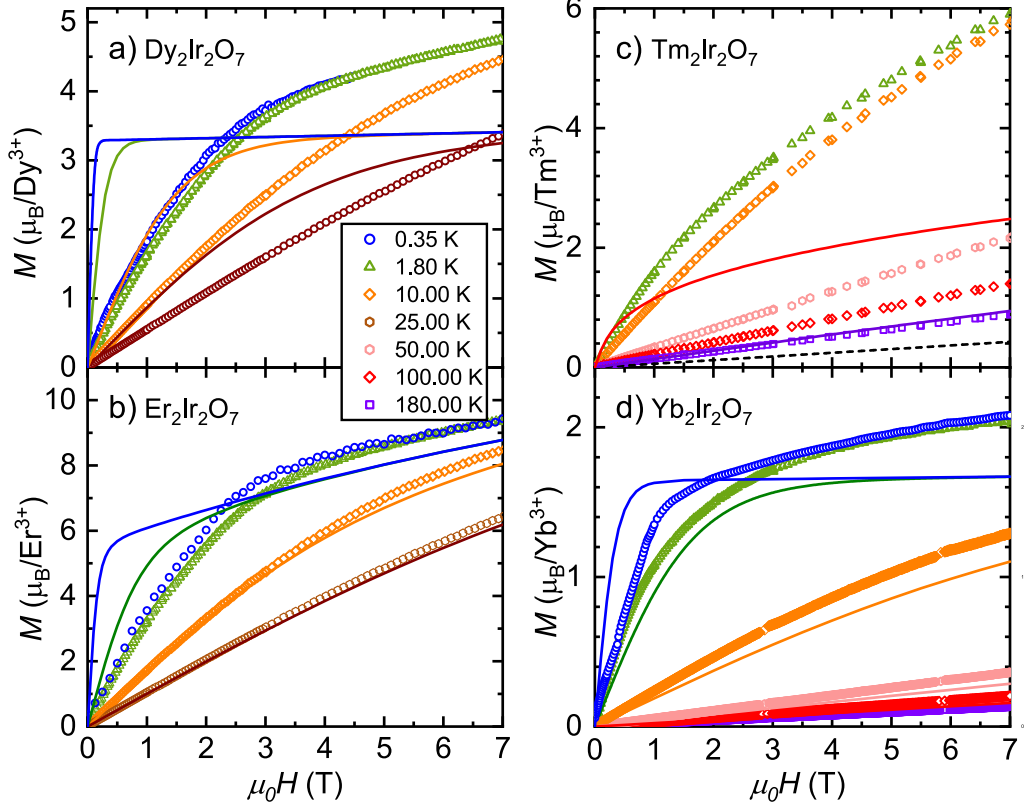


Figure 4.14. Isothermal magnetization of $A_2Ir_2O_7$. The curves of respective colours calculated from CF parameters are compared to experimental data. In the case of $Tm_2Ir_2O_7$, the CF-based mean field calculation of 180 K is represented by a black dashed line. CF calculations including the molecular field constant are shown for 180 and 100 K data (full lines).

Field dependence of $A_2Ir_2O_7$ isothermal magnetization is displayed in Figure 4.14. For all compounds, the magnetization increases with an applied field, attaining the value μ_{7T} in 7 T at the lowest temperature, while still not saturated (Table 4.2). Isothermal magnetization of $Dy_2Ir_2O_7$ reaches the μ_{7T} equal to $4.8(1) \mu_B$, which is about half of the value of Dy^{3+} free ion. Increase of magnetization in higher fields is expected; however, considering the field development, estimation of the saturated value to $5\mu_B$ is still well below the free ion moment. On the other hand, the μ_B of $Er_2Ir_2O_7$ at 0.4 K exceeds the value expected for the Er^{3+} free ion, which is, however, attributed to the present magnetic moment of Ir^{4+} (which can reach $1.74 \mu_B$ for $S = 1/2$). Magnetization will likely saturate at a value higher than $10 \mu_B$. $Tm_2Ir_2O_7$ reveals magnetization in 7 T close to the expected value, and following the trend, it will saturate at the value well above $8 \mu_B$. A different isothermal magnetization development is observed in the case of the ytterbium analogue. Magnetization in 7 T reaches a significantly lower value than that of a free ion and tends to saturate at this value. A reduction of $Yb_2Ir_2O_7$ magnetic moment can be discussed within the frame of the effective $S = 1/2$ description of Yb moments. Competition between ferromagnetic and antiferromagnetic states was proposed to cause strong spin fluctuations at low temperatures, which, together with the molecular field of the iridium sublattice, is responsible for the magnetic moment reduction, experimentally determined to $0.57 \mu_B$ [13].

Ordering of iridium sublattice is also demonstrated in the specific heat of all investigated $A_2\text{Ir}_2\text{O}_7$ compounds as a high-temperature anomaly. The onset of the anomaly corresponds to the temperature of a bifurcation between ZFC and FC magnetization curves, T_{Ir} (Figure 4.11e - h). Such an anomaly was previously reported only for the light A iridate pyrochlores [8]; however, we observed it also in Lu analogue (Figure 4.10, section 4.2.1). The shape of the anomalies is rather broad, which indicates at least partially continuous character of the magnetic transition. In addition, the analysis of the iridium transition anomaly is influenced by the significant phonon contribution. The comparison of the rare-earth magnetism influence on iridium magnetic anomaly does not reveal significant changes between magnetic and non-magnetic A iridate pyrochlores (see data in [8, 7]).

To properly characterize the anomaly at T_{Ir} , the connected entropy was calculated. The specific heat data were fitted by a third-order polynomial function (green line in Figure 4.11) to describe the specific heat at high temperatures excluding the anomaly. Subsequently, the measured and fitted data were subtracted, and the entropy was obtained by integration of the difference data. We are aware of a large experimental error of S_{Ir} ; the calculated value is considered as a lower limit of the iridium transition entropy. The values of S_{Ir} for all investigated analogues are listed in Table 4.2. The calculated entropies for individual $A_2\text{Ir}_2\text{O}_7$ are comparable and also well comparable to the light rare-earth analogues (0.47, 2.00, and 1.40 $\text{J mol}^{-1}\text{K}^{-1}$ for $A = \text{Nd}, \text{Sm},$ and Eu , respectively [8]). No clear evolution of S_{Ir} with A is followed, documenting a small/negligible influence of rare-earth magnetism on the Ir sublattice in the high-temperature region for heavy rare-earth $A_2\text{Ir}_2\text{O}_7$, that is, at least above T_{Ir} , which is also almost insensitive to the A sublattice (Figure 4.12). The entropy values are significantly smaller than the magnetic entropy expected for the Ir^{4+} with $S = 1/2$ ($R \ln(2) = 5.7 \text{ J mol}^{-1}\text{K}^{-1}$), which can be simply ascribed to frustration of magnetic moments or the itineracy of $5d$ electrons [8].

Supposing that the entropy is of purely electronic origin, the electronic specific heat coefficient γ_{Ir} can be estimated as for the case of $\text{Lu}_2\text{Ir}_2\text{O}_7$ in section 4.2.1. The γ_{Ir} values are listed in Table 4.2, the behaviour is far from the metallic $\text{Nd}_2\text{Ir}_2\text{O}_7$ (14 $\text{mJ mol}^{-1}\text{K}^{-2}$ [6]) meaning the investigated $A_2\text{Ir}_2\text{O}_7$ are nonmetallic, as previously confirmed by the electrical resistivity measurements [106]. $\text{Lu}_2\text{Ir}_2\text{O}_7$ with the highest value of γ_{Ir} among the heavy rare-earth pyrochlore iridates could be considered as semimetallic, which was supported also by the DFT calculations and low-temperature specific heat analysis, see section 4.2.1, [93].

Magnetic properties of $A_2\text{Ir}_2\text{O}_7$ were investigated by subtracting a $\text{Lu}_2\text{Ir}_2\text{O}_7$ analogue, which served as an estimation of electron, lattice and iridium contributions. Such an approximation is mostly valid above T_{Ir} as there is no significant interaction between A and Ir magnetic moments. Lowering the temperature, the contributions of the A magnetism and interaction between the two magnetic sublattices, A and Ir, begin to play an important role and possibly influence electronic and lattice-specific heat. Additionally, the phonon contribution is influenced by the rare-earth mass and interatomic distances. Fully conscious of the uncertainties, we calculated C_{mag} for investigated compounds, see Figures 4.22 and 4.15. Before to the subtraction of $\text{Lu}_2\text{Ir}_2\text{O}_7$, the $A_2\text{Ir}_2\text{O}_7$ specific heat data associated with the Ir ordering anomaly was approximated by the polynomial

function (blue lines in Figure 4.11). Utilizing the C_{mag} , the corresponding magnetic entropy S_{mag} was determined according to the relation 2.9.

Several anomalies are followed in magnetic specific heat data: Higher temperature anomalies in $A_2\text{Ir}_2\text{O}_7$ are attributed to the Schottky contribution C_{Schott} and are analysed within the frame of the CF model in the next section. In the low-temperature part of specific heat, the anomalies at T_{LT} in $A_2\text{Ir}_2\text{O}_7$ with Kramers' doublet $A = \text{Dy}$, Er , and Yb are connected with the A sublattice ordering (see Figure 4.15 a - d). A comparison of the $\text{Lu}_2\text{Ir}_2\text{O}_7$ specific heat to other iridates (blue triangles in Figure 4.15) highlights that the anomaly contains only very weak electronic, lattice, and iridium sublattice specific heat contributions. CF origin of the anomalies is excluded based on the CF models presented in section 4.3 with parameters listed in Table 4.3. Evolution of low temperature anomalies with application of the field as well as the analysis of connected S_{mag} (Figure 4.15) further corroborate that the nature of T_{LT} anomalies is determined by the rare-earth magnetism. Individual aspects of the $A_2\text{Ir}_2\text{O}_7$ low-temperature anomalies will be discussed in the following paragraphs.

$\text{Er}_2\text{Ir}_2\text{O}_7$ is dominated by the $T_{LT} = 2$ K anomaly of magnetic origin. The magnetic entropy, the right axis of Figure 4.15, reaches the value of $R \ln(2)$ at the anomaly-onset temperature, which corresponds to the Zeeman splitting of the ground-state doublet. The broadness of the anomaly is not consistent with a standard magnetic phase transition from paramagnetic to ordered state. Instead, it suggests an accretion of magnetic correlations. Such an assumption is corroborated by neutron diffraction experiments. No magnetic reflections related to long-range order and freezing of Er magnetic moments at low temperature were reported for $\text{Er}_2\text{Ir}_2\text{O}_7$ [9]. The anomaly becomes broader and shifts to higher temperature in the applied magnetic field (Figure 4.15 f). Such a field evolution of specific heat would be consistent with long-range ferromagnetic ordering; the magnetic correlations among magnetic moments become stronger in an applied field. However, considering the shape of the anomaly and the negative Curie-Weiss temperature Θ_p , the antiferromagnetic short-range correlations (a spin glass-like state) should be considered instead. To estimate the effect of exchange interactions on the ground-state doublet, a simple model (see [94] for details) was used. The splitting of the erbium doublet and connected specific heat were calculated considering the magnetic field of the order of tesla (ranging from 0.5 to 2.0 T). The best agreement with the measured data was obtained considering the internal field of 0.9 T (black line in Figure 4.15 b). The low-temperature part of the anomaly was well described, while the specific heat at higher temperatures showed larger values than our crude model. Although the agreement is reasonable, the magnetic exchange interactions at low temperatures should be considered more complex; further, the magnetic interactions between Er and Ir sublattices cannot be ruled out.

$\text{Yb}_2\text{Ir}_2\text{O}_7$ reveals an anomaly with onset at 5 K. Compared to the erbium case; the anomaly is broader suggesting a rather continuous development of magnetic correlations. Entropy connected with the anomaly does not reach a value expected for the ground state doublet up to 10 K. It is consistent with a recent study [13] which showed the emergence of ferromagnetic peaks at sub-kelvin temperatures, together with a weak AIAO component of Yb magnetic moments. Comparing the erbium and ytterbium analogues, a different evolution of the

Table 4.2. Magnetic properties of $A_2\text{Ir}_2\text{O}_7$. Total angular momentum J^A and predicted moments, $\mu_s^A (= g_J J^A)$ and $\mu_{eff}^A (= g_J \sqrt{J^A(J^A + 1)})$ of A^{3+} ions (g_J is the Landé factor). The temperature of Ir sublattice ordering, T_{Ir} and temperature at which the magnetic effects on A^{3+} ions set in, T_A . Effective magnetic moment μ_{eff} and paramagnetic Curie temperature Θ_p obtained by fitting the magnetization to the Curie-Weiss formula; also, difference magnetization data A - Lu were fit. Lowest-temperature magnetic moment in 7 T, μ_{7T} . Entropy and electronic coefficient related to the Ir high-temperature specific heat anomaly, S_{Ir} and γ_{Ir} , respectively. T_{LT} stands for the temperature of the low-temperature magnetic anomaly in specific heat.

	$\text{Dy}_2\text{Ir}_2\text{O}_7$	$\text{Er}_2\text{Ir}_2\text{O}_7$	$\text{Tm}_2\text{Ir}_2\text{O}_7$	$\text{Yb}_2\text{Ir}_2\text{O}_7$	$\text{Lu}_2\text{Ir}_2\text{O}_7$
J^A	7.5	7.5	6	3.5	0
μ_s^A (μ_B)	10	9	7	4	0
μ_{eff}^A (μ_B)	10.65	9.58	7.56	4.54	0
T_{Ir} (K)	128(2)	140(2)	142(2)	143(2)	147(2)
T_A (K)	25(2)	30(2)	40(3)	30(3)	
μ_{eff} (μ_B)	10.2(1)	9.12(4)	7.13(3)	4.05(3)	0.88(4)
Θ_p (K)	-13.1(2)	-26(2)	-48(2)	-106(3)	-217(3)
$\mu_{eff}^{A-\text{Lu}}$ (μ_B)	8.9(1)	8.94(4)	6.89(4)	3.88(4)	
$\Theta_p^{A-\text{Lu}}$ (K)	-11.3(2)	-17(1)	-35(1)	-91(1)	
μ_{7T} (μ_B)	4.8(1)	9.4(1)	6.0(1)	2.1(1)	0.05(1)
S_{Ir} ($\text{Jmol}^{-1}\text{K}^{-1}$)	1.26(3)	0.38(3)	0.51(3)	0.54(4)	0.57(3)
γ_{Ir} ($\text{mJmol}^{-1}\text{K}^{-2}$)	9.2(2)	2.7(2)	3.7(2)	3.8(2)	4.1(2)
T_{LT} (K)	1.5(2)	2.0(2)		2.7(2)	

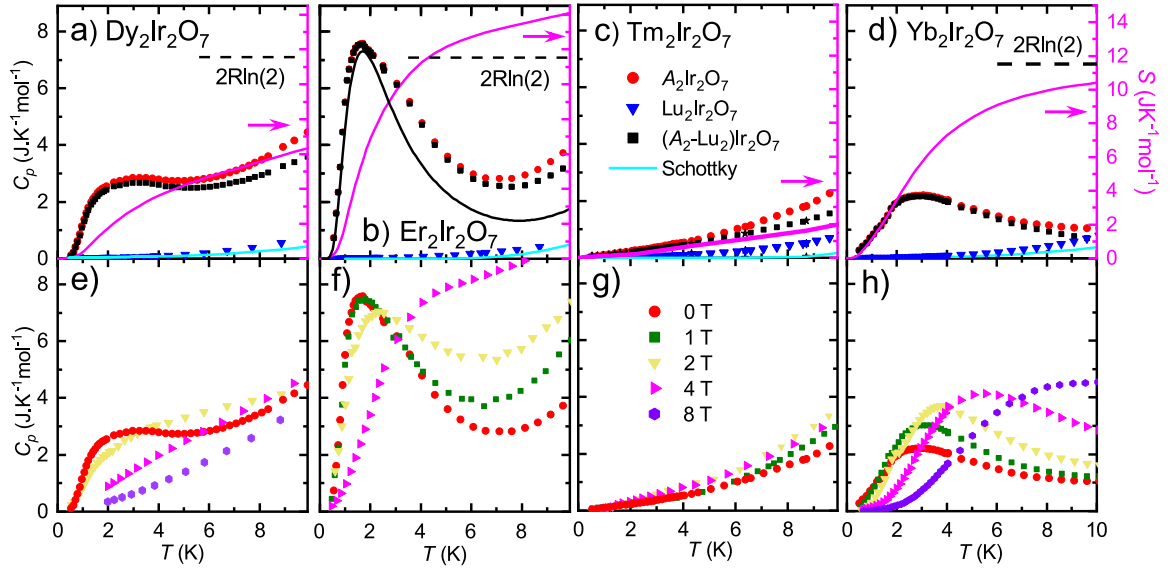


Figure 4.15. *Low temperature specific heat of $A_2Ir_2O_7$.* Panels (a - d) contain specific heat of A and Lu analogues and their difference. Schottky contribution to specific heat calculated from the CF energy scheme is shown as well (blue lines). On the right axis, the entropy calculated from $(A_2 - Lu_2)Ir_2O_7$ data is presented (pink line). Panels (e - h) show temperature evolution of specific heat in selected applied magnetic fields.

higher-temperature parts of the anomalies is followed, that is, an increase for Er and decrease or constant value with increasing temperature for the Yb analogue, well in agreement with the CF scheme (Table 4.3).

$Dy_2Ir_2O_7$ measurement reveals the anomaly centred at 1.5 K. Dysprosium moments are supposed to enter into a magnetically fragmented phase [14] which is accompanied by an anomaly resembling one of the spin-ice materials [27]. However, the peak in $Dy_2Ir_2O_7$ specific heat is significantly broader in comparison with the classical spin-ice compounds, which is caused by the distribution of the local magnetic fields acting on Dy ions. The reduced value of the magnetic entropy is well consistent with the scenario of the magnetically fragmented state and also with the isothermal magnetization measurement (see Figure 4.14 a) with magnetic moments divided into AIAO ordered phase and correlated Coulomb phase. An application of the external field leads to the ground state splitting and shifts the anomaly towards higher temperatures, similar to erbium and ytterbium analogues.

A completely different evolution of low-temperature specific heat is followed in $Tm_2Ir_2O_7$. Below 10 K, its specific heat differs from the $Lu_2Ir_2O_7$ analogue subtly, just by a CF contribution, as presented in Figure 4.15 c). No anomaly at low temperature is expected, contrary to other analogues, because of the non-magnetic ground-state singlet state. The applied magnetic field acts on the first CF excited doublet and splits it, leading to a change in specific heat in the low-temperature region. A similar effect is observed for the Er analogue, contrary to $Yb_2Ir_2O_7$ with the first excited CF state at significantly higher energy (Table 4.3).

For a deeper insight into the magnetization and specific heat properties of $A_2Ir_2O_7$ as well as into the role of iridium sublattice magnetism, the knowledge

of single-ion magnetism of rare-earth ions is highly desirable. To reveal a CF excitation spectra of selected $A_2\text{Ir}_2\text{O}_7$, the inelastic neutron scattering experiment was performed on the $A = \text{Er}$ and Tm . The results are analysed in following section 4.3 together with the mean-field analysis of magnetization and specific heat data.

4.3 Inelastic neutron scattering on $\text{Er}_2\text{Ir}_2\text{O}_7$ and $\text{Tm}_2\text{Ir}_2\text{O}_7$

Complex behaviour of $A_2\text{Ir}_2\text{O}_7$ results from the magnetism of iridium and rare-earth ions as well as their entanglement. Although the $A_2\text{Ir}_2\text{O}_7$ pyrochlores stand in the foreground of scientific interest over, at least, two decades, only a handful of reports on single-ion properties, namely, crystal field excitation (CF), has been presented (the case of $A = \text{Dy}$ [14], Ho [15] and Yb [13]). The knowledge of the CF is, however, essential to correctly understand the physical properties of the compound as well as its ground state. In this chapter, the CF schemes of rare-earth ions in $\text{Er}_2\text{Ir}_2\text{O}_7$ and $\text{Tm}_2\text{Ir}_2\text{O}_7$ are determined using an inelastic neutron scattering technique [94]. The CF eigenenergies and parameters were used to describe the specific heat and DC magnetization data. An excellent agreement between the experiment and CF calculations was obtained, proving a crucial role of erbium/thulium single-ion magnetism in $A_2\text{Ir}_2\text{O}_7$ properties. The inelastic neutron scattering experiment was performed on the time-of-flight spectrometer MARI at the Rutherford Appleton Laboratory (ISIS), Didcot as described in section 2.6.

4.3.1 Crystal field scheme of $\text{Er}_2\text{Ir}_2\text{O}_7$

Ground-state multiplet of Kramers' Er^{3+} ion ($J = 15/2$) is splitted in the crystal field into doublets and quadruplets, depending on point-group symmetry of the atomic position it occupies. As the Wyckoff position of erbium in the $Fd\bar{3}m$ space group is $16c$, the point symmetry is trigonal ($D_{3d}, -3m$). Therefore, the energy spectrum of erbium pyrochlore contains eight CF doublets with one doublet being the ground state. The inelastic neutron scattering experiment disclosed CF excitation scheme of $\text{Er}_2\text{Ir}_2\text{O}_7$ and its development with momentum transfer ($Q = (|Q|)$) and temperature.

Dependence of the energy transfer ΔE on the momentum transfer Q is plotted in Figure 4.16 where several energy regions with magnetic signal are identified. The signal corresponding to three transitions between the ground state and the respective excited states is found at around 5.5, 9, and 20 meV. Much broader magnetic signal is seen between 60 and 75 meV. Finally, a weak magnetic signal is traced at 90 meV. No magnetic excitation is observed at higher energy up to 150 meV. The magnetic origin of the observed signal is unambiguously proven by its Q dependence: The signal becomes weaker with increasing Q following the Q dependence of the magnetic form factor (see chapter 2.6). An example of Q development of the intensity of the first three excitations is shown in Figure 4.17. The inset of Figure 4.17 presents a comparison between Q dependence of the magnetic form factor $F^2(Q)$ and the measured intensity of the first CF excitation. The same Q dependence was followed for all excitations.

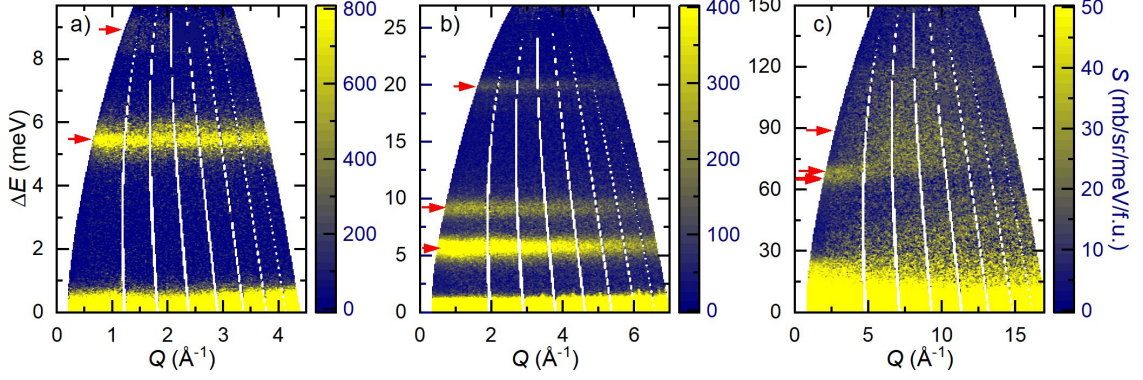


Figure 4.16. Magnetic and lattice excitations in $\text{Er}_2\text{Ir}_2\text{O}_7$. E - Q maps measured with incident energies a) 10 meV, b) 30 meV, and c) 180 meV at 5 K are presented. The arrows mark the magnetic (CF) excitations.

Temperature evolution of its intensity further documents the magnetic origin of the observed excitations. Measured data were analysed constructing so-called Q cuts by integration of the signal in the low- Q region (Figure 4.18). The intensity of magnetic (CF) excitation decreases with increasing temperature due to the substantial thermal population of individual energy levels. Furthermore, thermally populated energy levels allow the neutron to gain energy, leading to both excitations/de-excitations in the neutron-energy-gain (system-energy-loss) part of the spectrum and excitations between excited states. Such excitations are clearly observed in the spectra measured at 60, 100, and 200 K (Figure 4.18). Let us illustrate the influence of the thermal population of energy levels in the low-energy part of the spectrum (focusing on the excitation at 5.5 meV in Figure 4.18 a): The excited state is mostly unpopulated at 5 K - the temperature (i.e., thermal energy; $E = k_B T$) is too small to noticeably populate the energy states. Therefore, the measured spectrum contains a signal only in the neutron-energy-loss part. By increasing the temperature up to 60 K, the energy levels become partially thermally occupied. The excitation in the neutron-energy-gain part of the spectrum is observed in -5.5 meV. A further signal is pronounced at 3.5 meV corresponding to the excitation from the 5.5 - meV state to the 9 - meV state. The respective excitation occurs (at -3.5 meV) in the neutron-energy-gain part of the spectrum. An additional increase of temperature leads to a further thermal population of energy states, i.e., to a decrease of intensity of the 'base-temperature' excitation at 5.5 meV and an increase of the intensity of 'temperature-induced' excitations (-5.5, -3.5, and 3.5 meV). A high enough temperature causes all states to be (partly) thermally populated and all types of (de-)excitations to be manifested.

The CF excitations in $\text{Er}_2\text{Ir}_2\text{O}_7$ are well described within a standard crystal field model. Er^{3+} ions ($J = 15/2$) on 16c Wyckoff position with a trigonal point symmetry (D_{3d} , $-3m$). Therefore, the crystal field Hamiltonian introduced in chapter 2.6 can be written as follows:

$$\hat{H}_{CF} = B_0^2 \hat{O}_0^2 + B_0^4 \hat{O}_0^4 + B_3^4 \hat{O}_3^4 + B_0^6 \hat{O}_0^6 + B_3^6 \hat{O}_3^6 + B_6^6 \hat{O}_6^6. \quad (4.2)$$

B_m^n are the crystal field parameters and \hat{O}_m^n stand for Steven's operators representing the erbium 4 f shell. As the Wyckoff position of rare-earth ions in the

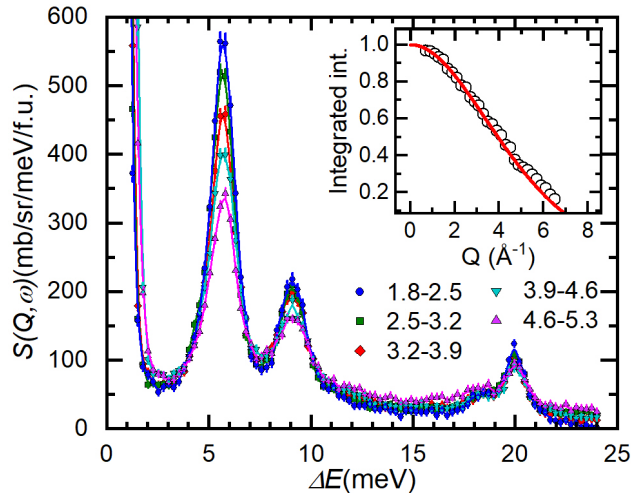


Figure 4.17. *Low-energy CF excitations in $\text{Er}_2\text{Ir}_2\text{O}_7$.* Q cuts of the map measured with $E_i = 30$ meV, representing the development of excitation intensity with increasing Q . The inset compares the Q dependence of the integrated intensity of the first excitation and magnetic form factor of Er^{3+} (tabulated value taken from [107]).

$F d \bar{3} m$ space group is $16c$, the point symmetry is not cubic (leading to some levels being four times degenerated), but trigonal ($D_{3d}, -3m$). Therefore, the energy spectrum of $\text{Er}_2\text{Ir}_2\text{O}_7$ contains eight CF doublets, respectively, with one of the doublet representing the ground state.

Seven transitions from the ground state are expected in the base-temperature energy spectrum of $\text{Er}_2\text{Ir}_2\text{O}_7$. To identify all seven expected CF transitions in the energy spectra is not necessarily straightforward, which is also the case for $\text{Er}_2\text{Ir}_2\text{O}_7$, where a previous investigation identified only four of the seven excitations required to fully fit and characterize the crystal field scheme [108]. Although the number of excitations was low, the CF parameters for $\text{Er}_2\text{Ir}_2\text{O}_7$ were determined in the previous study. However, to unambiguously identify the CF scheme and parameters, all seven excitations have to be accounted for. Three low-energy excitations are clearly observed; the shape of the peaks in Figure 4.18 excludes that they could individually consist of more than one contribution. The region between 60 and 75 meV contains at least two magnetic peaks, one at 65 meV and a second at 69 meV. The peak at 90 meV is relatively broad and of weak intensity. Therefore, one cannot be conclusive that it corresponds to a single excitation. Counting the peaks, one excitation is still missing to reveal a complete expected spectrum for $\text{Er}_2\text{Ir}_2\text{O}_7$. The missing signal was eventually found within the 65 - meV peak, which consists of two contributions. The two peaks close to each other (64.84 and 65.57 meV) cannot be unambiguously distinguished in our data (Figure 4.18 c), including the data measured with 120 meV of incident energy, not shown) due to resolution limitations. However, all the fitting of the region between 60 and 75 meV by three peaks (peak positions were restricted to lie within the interval and to have similar intensities), previous results on other Er-based pyrochlores [109], and our fit of the data to the CF model (consistent with magnetic susceptibility data) confirm such a scenario. The excitation energies obtained by fitting the individual peaks by a Lorentzian function are listed in Table 4.3 and are graphically represented by arrows in Figure 4.16.

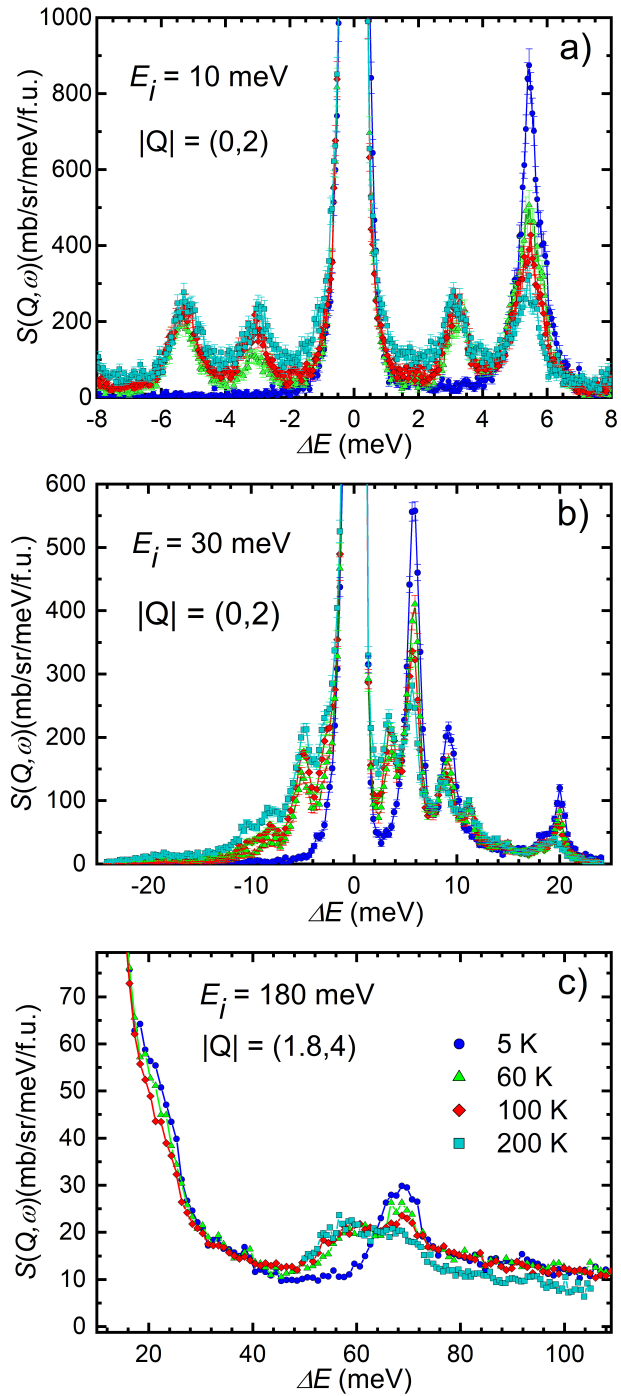


Figure 4.18. *Temperature development of CF excitations in $\text{Er}_2\text{Ir}_2\text{O}_7$.* Q cuts of E - Q maps measured at various listed temperatures, demonstrating a thermal population of the energy states with increasing temperature.

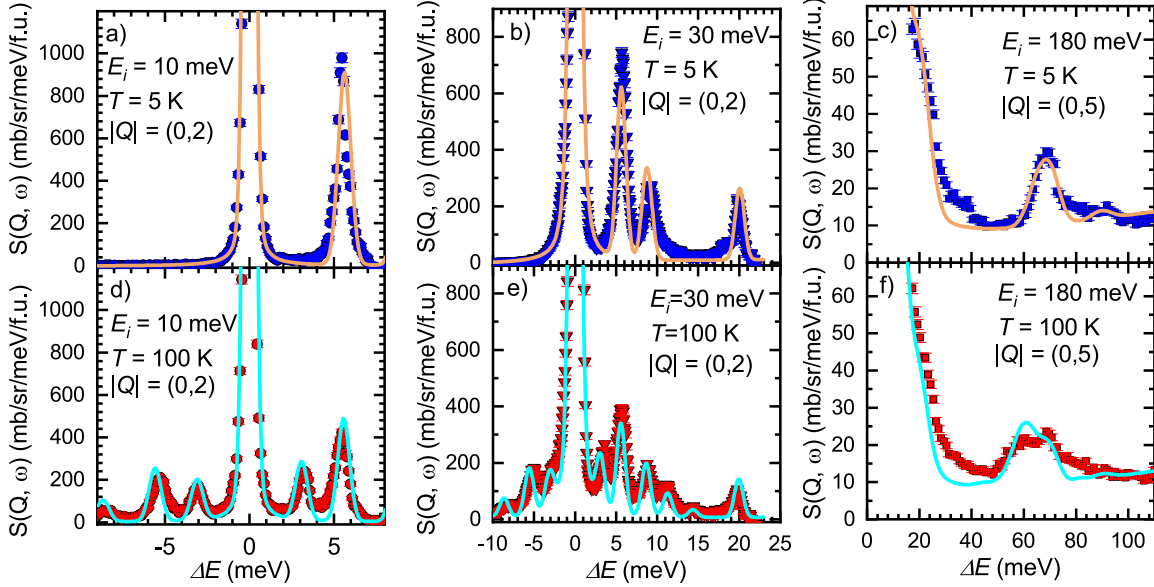


Figure 4.19. *CF Hamiltonian fits to magnetic excitations of $\text{Er}_2\text{Ir}_2\text{O}_7$.* Q cuts of $E - Q$ maps measured at 5 K (top panels) and 100 K (bottom panels). The solid lines represent the fit to the CF Hamiltonian (equation 4.2) resulting in CF excitation energies and parameters listed in Table 4.3.

The measured data were fitted to the model CF Hamiltonian (Equation 4.2) utilizing the previously reported CF parameters for $\text{Er}_2\text{Pt}_2\text{O}_7$ [109] as starting values. First, the fit of 5 - K data - combining three energy spectra measured with initial neutron energies 10, 30, and 180 meV - was done. Subsequently, these parameters were used as starting values to fit the data measured at all temperatures (i.e., 5, 60, 100, and 200 K). We remind the reader that at elevated temperature the intensity of individual excitations changes and simultaneously new excitations, corresponding to transitions between thermally populated energy levels, occur. The fitted spectra are presented in Figure 4.19 and the values of final CF energies and parameters are listed in Table 4.3. Small differences between the parameters obtained by fitting the 5 K spectra only and the parameters refined fitting the spectra at all temperatures demonstrate a good quality of the initial fit as well as the consistency of our experimental data measured at different temperatures.

4.3.2 Lattice and magnetic excitations in $\text{Tm}_2\text{Ir}_2\text{O}_7$

$\text{Tm}_2\text{Ir}_2\text{O}_7$ and $\text{Lu}_2\text{Ir}_2\text{O}_7$ pyrochlores were investigated by means of inelastic neutron scattering similarly as in our previous study of erbium iridate 4.3.1. Below, we provide a concise information on data treatment and analysis, not repeating some of the details discussed in section 2.6 and 4.3.1.

Energy excitations in lutetium analogue were investigated mainly to enable a subtraction of any phonon contribution from $\text{Tm}_2\text{Ir}_2\text{O}_7$ data, and, in turn, a study of magnetic excitations connected to Tm^{3+} ion. The dependence of the energy transfer ΔE on the momentum transfer Q , so-called $E - Q$ map, of $\text{Tm}_2\text{Ir}_2\text{O}_7$, $\text{Lu}_2\text{Ir}_2\text{O}_7$ and their difference for incident energies of 30, 120, and 180 meV at 5 K are plotted in Figure 4.20. To account for the different neutron scattering

cross-sections of Tm and Lu ions, $\text{Lu}_2\text{Ir}_2\text{O}_7$ data were multiplied by the ratio between the total scattering cross-sections of Tm and Lu, which equals to 0.9772, prior the subtraction.

Inspecting difference E - Q maps measured at 5 K, several magnetic excitations are unambiguously identified: signal at around 10, 35 and 55 meV (Figure 4.20). A broader magnetic signal is observed between 70 - 90 meV, and no additional magnetic excitations are detected up to 150 meV. We note that the low-energy excitations in spectra, most prominent peak at around 4 meV, were identified as CF contribution of unreacted Tm_2O_3 . As all CF excitations of thulium oxide are of low-energy (below 11 meV) [110], this parasitic signal did not hamper analysis of our data. We subtracted this Tm_2O_3 signal from difference data creating Figure 4.21.

Low- Q cuts of the subtracted data were closely investigated, searching for magnetic excitations and their evolution with temperature. Four excitations were observed in 5 K spectrum. Free Tm^{3+} ion with $J = 6$ has 13-fold degenerated ground state. In pyrochlore lattice, D_{3d} , $-3m$ point symmetry, the ground state multiplet of thulium ion is split into four doublets and five singlets with one being a ground state. (Contrary to Er ion, Tm is non-Kramers' ion. See section 4.3.1). Hence, 8 excitations are expected in spectra. Determining the CF scheme of $\text{Tm}_2\text{Ir}_2\text{O}_7$ utilizing only 4 excitations in the spectra would, of course, lead to dubious results. Therefore, we created a model CF spectrum, and used its parameters as starting values for a refinement of CF parameters of $\text{Tm}_2\text{Ir}_2\text{O}_7$.

Utilizing the previously determined CF schemes of $\text{Er}_2\text{Ir}_2\text{O}_7$ and $\text{Yb}_2\text{Ir}_2\text{O}_7$ analogues, see section 4.3.1 and reference [13], CF parameters for $\text{Tm}_2\text{Ir}_2\text{O}_7$ were calculated scaling the corresponding Stevens factors of these two analogues – the most natural choice from the viewpoint of atomic numbers of respective ions. See reference [94] for details. The resulting CF parameters and excitation energies are listed in Table 4.3. Significantly different CF schemes are bound to mirror in bulk properties of $\text{Tm}_2\text{Ir}_2\text{O}_7$. Indeed, inspecting the magnetic entropy (Figure 4.22c), the scheme derived from $\text{Yb}_2\text{Ir}_2\text{O}_7$ parameters gives worse agreement than that of $\text{Er}_2\text{Ir}_2\text{O}_7$. First, the entropy increases to the value of $R \ln(3)$ where its slope changes, corresponding to the transition from the ground state singlet to the first excited doublet. Another, much less pronounced, change in the entropy curve is observed at $R \ln(5)$ rather than at $R \ln(4)$, suggesting that the second excited state is a doublet, not a singlet. Also the magnetic susceptibility calculated from Er-re-scaled CF parameters agrees better with measurement, compared to calculations based on Yb model, see reference [84]. In further discussion, $\text{Er}_2\text{Ir}_2\text{O}_7$ based model was used for the analysis of $\text{Tm}_2\text{Ir}_2\text{O}_7$ INS spectra.

The spectra calculated from re-scaled CF parameters indicate low intensity of the high energy excitations, perfectly in agreement with experiment. Inspecting the high-energy region in $E - Q$ maps (Figure 4.20) and Q cuts in Figure 4.21, no defined magnetic signal is found above 60 meV. The model predicts only 3 excitations (ground state singlet, two doublets, and singlet) in low-energy region. Actually, 4 excitations are observed in data (supposedly additional doublet is actually at lower energy than predicted). Refinement of 6 CF parameters from data containing only 4 peaks was highly unstable. Therefore, we performed a simultaneous refinement of not only 30, 120 and 180 meV spectra at 5 K, but also at temperatures 100 and 200 K. Thermal population of the first excited CF

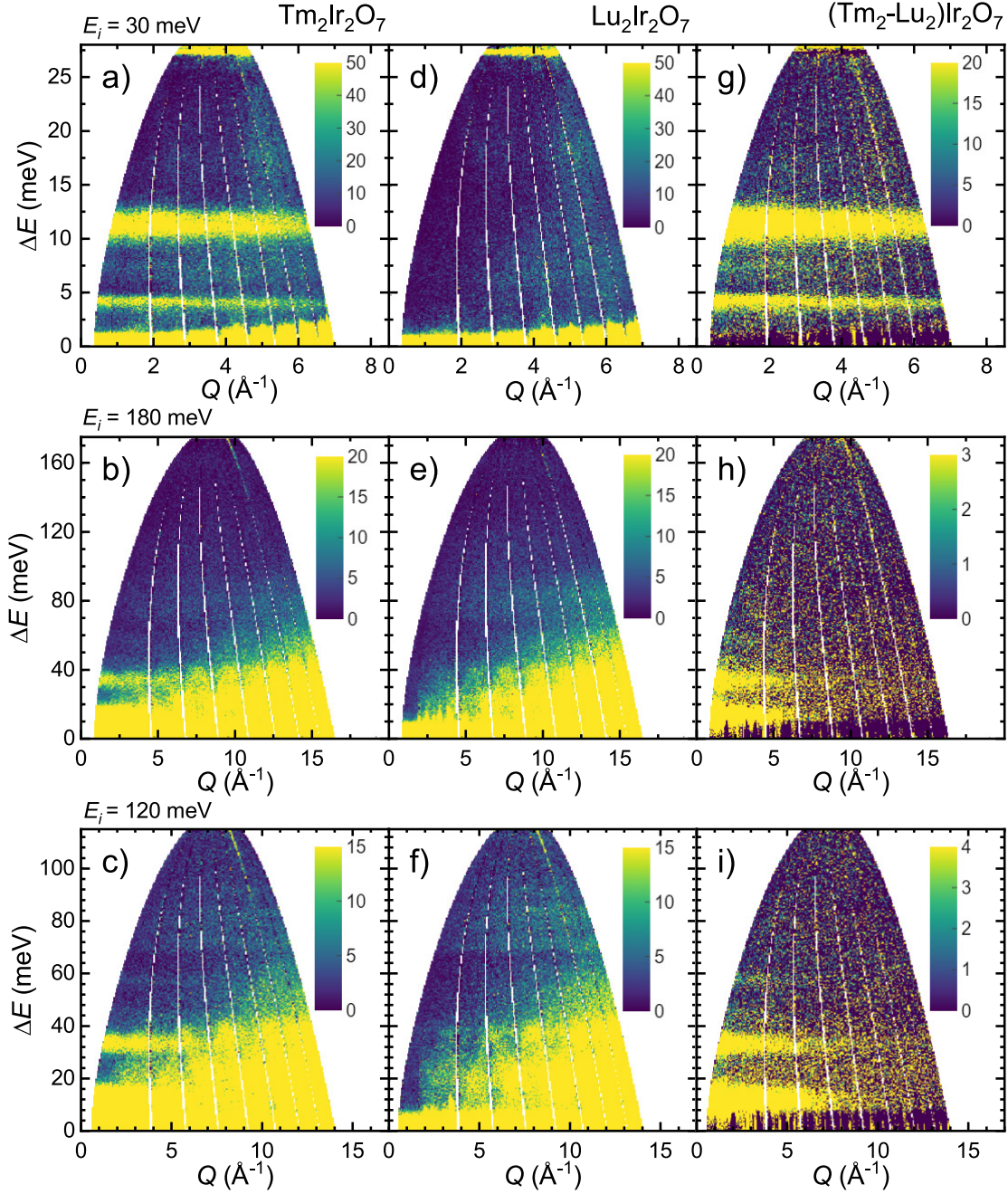


Figure 4.20. *Magnetic and phonon excitations in $Tm_2Ir_2O_7$ and $Lu_2Ir_2O_7$. $E - Q$ maps measured within incident energies 30, 120 and 180 meV at 5 K are presented for $Tm_2Ir_2O_7$ (a - c), $Lu_2Ir_2O_7$ (d - f) and their difference (g - i).*

level at 10.5 meV allows a transition to higher lying levels at 100 and 200 K, resulting in new magnetic excitations at $\sim 23.3, 26.2, 46.0$ meV, and a very weak signal around 62 meV (denoted by orange arrows in Figure 4.21). Of course, also other excitations between partially thermally populated higher-energy levels are allowed, but are expected to be significantly less intense. Tuning the CF parameters to properly describe all the peaks in measured spectra led to a final set of parameters listed in Table 4.3. Fits of data to CF scheme are plotted in Figure 4.21, showing a reasonable agreement with measurement.

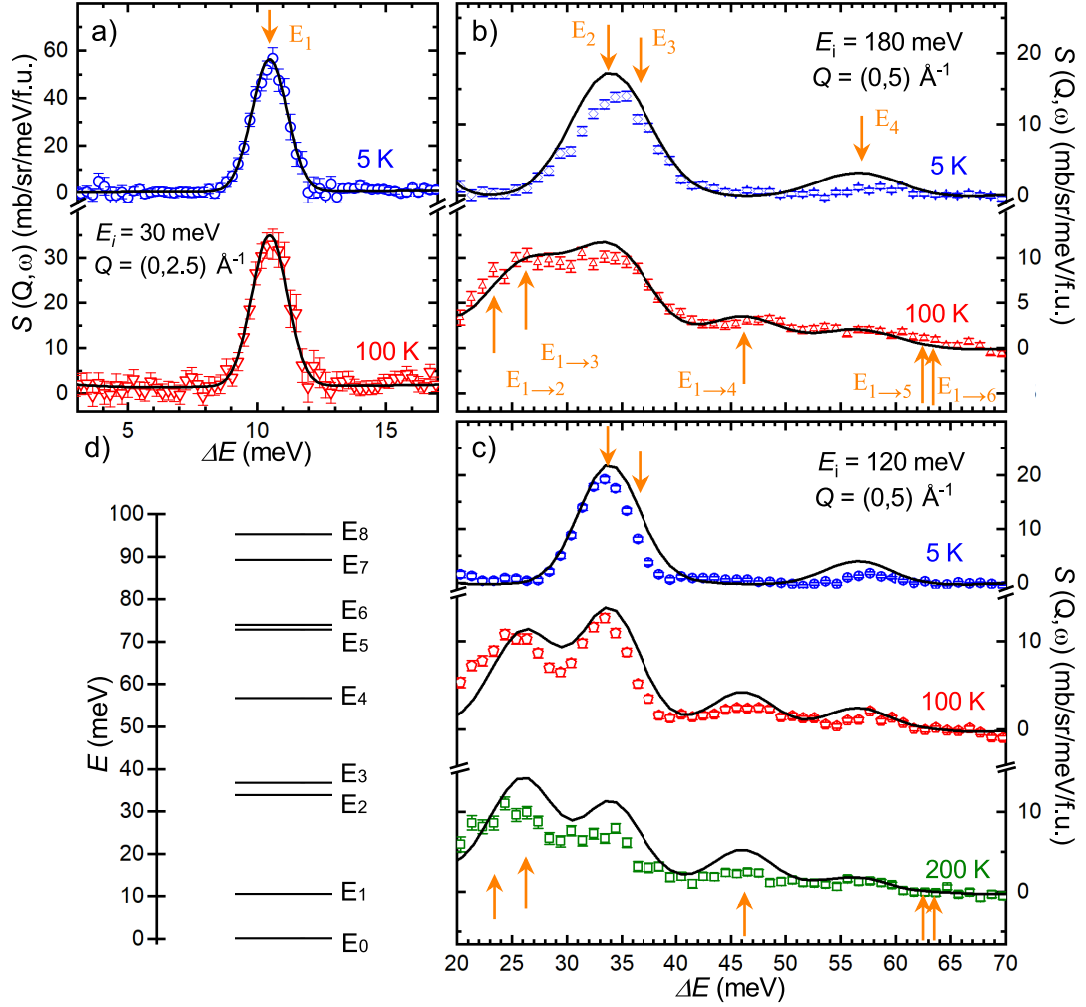


Figure 4.21. *CF Hamiltonian fits to magnetic excitations in $Tm_2Ir_2O_7$.* Q cuts of $E - Q$ maps measured with a) 30, b) 180 (upper part) and c) 120 meV (bottom part) incident energies at 5, 100, and 200 K. Black lines represent the fits to CF model (parameters listed in Table 4.3). Indexed arrows denote a CF excitations' energies, see panel d) and Table 4.3.

Table 4.3. CF parameters of $A_2Ir_2O_7$. CF eigenenergies and parameters in Steven's notation (in unit of meV) of $A_2Ir_2O_7$ determined from INS data ($Dy_2Ir_2O_7$ and $Yb_2Ir_2O_7$ parameters were adopted from [14, 13] and rescaled). Two sets of parameters for $Tm_2Ir_2O_7$ were derived by scaling the CF parameters of Er and Yb analogues by Steven's factors (Er \rightarrow Tm, denoted as $Tm_2Ir_2O_7^{Er}$) and transforming the Wybourne CF parameters to Steven's notation (Yb \rightarrow Tm, signed as $Tm_2Ir_2O_7^{Yb}$). The energies of singlet states for $Tm_2Ir_2O_7$ are marked with symbol (s); the other levels are doublets. The g -tensor components, perpendicular and parallel to local $\langle 111 \rangle$ axes, and their ratio are listed as well.

	$Dy_2Ir_2O_7$	$Er_2Ir_2O_7$	$Tm_2Ir_2O_7$	$Tm_2Ir_2O_7^{Er}$	$Tm_2Ir_2O_7^{Yb}$	$Yb_2Ir_2O_7$
$B_0^2(10^{-2})$	-20.3	7.456	18.277	29.670	36.670	115.240
$B_0^4(10^{-3})$	-2.27	1.886	5.057	6.949	4.228	-55.840
$B_3^4(10^{-2})$	-1.58	1.148	3.184	4.228	4.54	-59.420
$B_0^6(10^{-6})$	8.37	9.720	-31.26	-26.330	143(2)	2333.770
$B_3^6(10^{-4})$	1.20	-1.473	3.873	3.981	143(2)	-567.570
$B_6^6(10^{-4})$	0.683	2.418	-5.89	-6.554	-4.398	348.380
E_0	0	0	0(s)	0(s)	0(s)	0
E_1	29.5	5.581	10.467	8.733	13.733	77.780
E_2	37.0	8.684	33.827(s)	37.646	24.359(s)	111.349
E_3		19.937	36.734	37.935(s)	32.418	151.680
E_4		64.149	56.559	65.429	60.740	
E_5		65.391	72.768(s)	83.915	71.550(s)	
E_6		70.214	73.868	86.147(s)	75.259	
E_7		89.935	89.239(s)	117.112(s)	110.438(s)	
E_8			95.250(s)	121.177(s)	113.829(s)	
g_\perp	19.71	6.28	0	0	0	4.03
g_z	0	3.04	0	0	0	2.32
g_\perp/g_z	19.71	2.1				1.74

4.3.3 Mean field calculations

To calculate the magnetization as a function of magnetic field, DC magnetic susceptibility and magnetic contribution to specific heat as a function of temperature, we employed the microscopic Hamiltonian containing the trigonal crystal field term (see equation 4.2) and the Zeeman term. The Schottky specific heat was calculated according to the equation 2.7 with the energy levels E_i determined from the INS experiment.

The wave functions and eigenenergies of the Er^{3+} ($J = 15/2$) in CF were determined diagonalizing the model Hamiltonian. These were used to compute the desired quantities using our in-house computer codes [111]. The real diagonal matrix of the total angular momentum \hat{J}_z operator and the real symmetric matrix of the off-diagonal \hat{J}_x operator were both transformed by similarity transformation

$$\hat{J}_z^t = Q^T * \hat{J}_z * Q \quad (4.3)$$

and

$$\hat{J}_x^t = Q^T * \hat{J}_x * Q, \quad (4.4)$$

respectively. The matrix Q contains the eigenvectors of the microscopic Hamiltonian in columns and Q^T is the transpose matrix of Q . The magnetization as a function of magnetic field and temperature was obtained as

$$M_{\parallel} = gTr(\hat{J}_z^t * \rho) \quad (4.5)$$

and

$$M_{\perp} = gTr(\hat{J}_x^t * \rho), \quad (4.6)$$

where g is the Landé factor of the ground-state multiplet, ρ is the diagonal density matrix with exponentials $e^{-\frac{E_i}{k_B T}}$ on the main diagonal.

Comparison of magnetic susceptibility $M/H(T)$ with the calculations is displayed in Figure 4.13. CF parameters of $\text{Er}_2\text{Ir}_2\text{O}_7$ and $\text{Tm}_2\text{Ir}_2\text{O}_7$ derived from INS were supplemented by the CF parameters of $\text{Dy}_2\text{Ir}_2\text{O}_7$ and $\text{Yb}_2\text{Ir}_2\text{O}_7$, adopted from references [14, 13]. Mean field description of Tm^{3+} behaviour based on CF of $\text{Tm}_2\text{Ir}_2\text{O}_7$ was confronted with calculations utilizing the rescaled CF parameters of $\text{Er}_2\text{Ir}_2\text{O}_7$ (details can be found in [84]). Magnetization was calculated for two local crystallographic directions; along and perpendicular to the tetrahedron $\langle 111 \rangle$ axes. The two components were powder-averaged, and the averaged values are plotted in Figure 4.13 as green lines. A remarkable agreement between calculations and measurement was observed in the case of $\text{Er}_2\text{Ir}_2\text{O}_7$ and $\text{Yb}_2\text{Ir}_2\text{O}_7$ suggesting that the magnetic behaviour is governed by the rare-earth magnetism well below the T_{Ir} . However, the magnetic behaviour of $\text{Tm}_2\text{Ir}_2\text{O}_7$ and $\text{Dy}_2\text{Ir}_2\text{O}_7$ is reproduced by the calculation rather poorly. To explain the $\text{Tm}_2\text{Ir}_2\text{O}_7$ deviation from the mean-field approach, the ground state of Tm ion should be considered. Tm^{3+} has a non-magnetic singlet ground state which is affected by complex exchange interactions between the induced thulium magnetic moment via the polarization of the ground-state singlet and itinerant iridium moments. The calculations of the magnetization of $\text{Dy}_2\text{Ir}_2\text{O}_7$ indicate a strong anisotropy in the system, the mean-field calculations reproduce just a high-temperature data well above T_{Ir} . The disagreement between the mean-field approximation of the experimental data can be caused by the inappropriate method of simple powder

averaging, however, the MFA of $\text{Er}_2\text{Ir}_2\text{O}_7$ and $\text{Yb}_2\text{Ir}_2\text{O}_7$ data turned out to be sufficient. It suggests that in the case of Dy and Tm analogues more complicated interactions, magnetic frustrations or the influence of the iridium staggered molecular field play an important role.

Similar to the temperature dependence of magnetic susceptibility, the isothermal magnetization was calculated utilizing the CF parameters. The powder average of the magnetization curves in the mean-field approximation is presented as line of respective colour in Figure 4.14. In the case of $\text{Dy}_2\text{Ir}_2\text{O}_7$, the calculations significantly underestimate the experimental magnetization. However, the Ir sublattice moment contributes to the total magnetic response by the value up to $1.74 \mu_B$ for the $S = 1/2$ state of Ir^{4+} . Moreover, the suggested magnetically fragmented state in $\text{Dy}_2\text{Ir}_2\text{O}_7$ ions also predicts a reduced value of dysprosium moment [14].

The calculations of the $\text{Yb}_2\text{Ir}_2\text{O}_7$ magnetic response also underestimate the total magnetization; however, the μ_{7T} at 0.4 K increased by the value of ordered Ir moment is consistent with the mean-field predictions based on the CF scheme published in [13]. The lowest agreement between mean-field approximation and experimental data is found in the case of $\text{Tm}_2\text{Ir}_2\text{O}_7$. An explanation of such a disagreement can be found in the interaction between a non-magnetic Tm ground state and the molecular field. To quantify the value of molecular field acting on Tm ion the following numerical experiment was performed: the molecular field was included in the direction of the external field to microscopic Hamiltonian, the molecular field was calculated self-consistently; $H_{mf} = \lambda' \langle M \rangle$, where λ' and $\langle M \rangle$ are the adjustable molecular field constant and the average magnetization at $T = 180$ K, respectively. This estimate gives a good average value of magnetization at $T = 180$ K (see the purple line in Figure 4.14 c); however, lower temperature (≤ 100 K) data are described rather poorly. Moreover, mean-field calculations including the effect of molecular field predict the ferromagnetic type of metamagnetic transition which is not reproduced by the experimental data. The inadequate description of the magnetization below T_{Ir} points to more complicated interactions exceeding a simple molecular field approximation.

Higher-temperature part of C_{mag} in the case of $A = \text{Er}$ and Yb is well described by the changes in the internal energy of the system, Schottky specific heat (see Table 4.3 and section 4.3). C_{mag} of $\text{Er}_2\text{Ir}_2\text{O}_7$ reveals anomalies centred at 30 K and 240 K which are well described by the Schottky contribution to the specific heat (blue lines in Figure 4.22b) calculated from CF excitation energies. A broad anomaly in $\text{Yb}_2\text{Ir}_2\text{O}_7$ data is centred at 260 K, consistent with the CF excitation spectra, and shows a large splitting between the ground and first excited CF states (see Figure 4.22 d). Inspecting the magnetic entropy of $\text{Er}_2\text{Ir}_2\text{O}_7$ shown in the insets of Figure 4.22 b), four regions can be distinguished: (i) the low-temperature region, where the entropy rises from zero to the value of $R \ln(2)$ with increasing temperature, corresponding to splitting of the ground-state doublet due to magnetic correlations; (ii) the region below 90 K, where the entropy increases significantly up to $R \ln(6)$, demonstrating that the first two CF excitations have not significantly different energies, both lower than ~ 9 meV; (iii) the region below 220 K, with entropy developing almost linearly with temperature up to $R \ln(8)$, pointing to the third excited doublet at energy < 20 meV; and finally (iv) the high-temperature region (> 220 K), exhibiting further entropy

increase, presumably up to the value of $R \ln(16)$ at significantly higher temperature; four CF doublets are expected in the higher-energy region. Our analysis of magnetic entropy is fully consistent with INS data presented in section 4.3.1.

The magnetic entropy of $\text{Tm}_2\text{Ir}_2\text{O}_7$ (see inset in Figure 4.22 c) reveals a step increase to $R \ln(3)$ followed by the change of the slope, which suggests the transition from the ground state singlet to the first excited doublet. Another change in the entropy curve is observed at $R \ln(4)$, which suggests the second excited state is a singlet. At $R \ln(6)$, the increase of magnetic entropy becomes less steep corresponding to the third excited doublet energetically proximal to second excited state. The higher-energy excited states are hard to recognize from magnetic specific heat data. Again, good agreement with INS data (section 4.3.2) is followed.

$\text{Yb}_2\text{Ir}_2\text{O}_7$ magnetic entropy development (inset in Figure 4.22 d) documents the population of the ground state doublet $R \ln(2)$ which is followed by a temperature plateau up to 130 K. At higher temperatures the entropy sharply increases close to the value of $R \ln(4)$ at 300 K, which is a consequence of a broad C_{mag} anomaly, that is, three CF excitations not much separated in energy (CF parameters from [13] listed in Table 4.3).

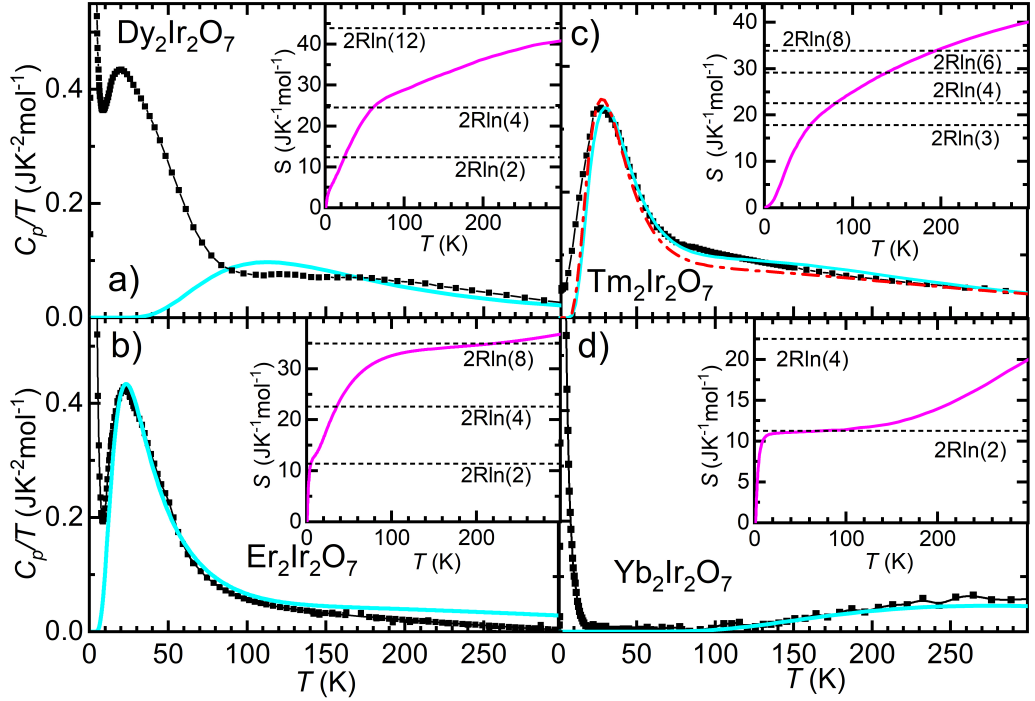


Figure 4.22. Schottky specific heat in $A_2\text{Ir}_2\text{O}_7$. Magnetic contribution to specific heat (black squares) is presented. Solid blue lines represent calculated Schottky specific heat, based on the CF parameters (see Table 4.3). Dashed red line in panel c) corresponds to Schottky specific heat of $\text{Tm}_2\text{Ir}_2\text{O}_7^{\text{Er}}$. The insets contains magnetic entropy calculated from magnetic specific heat (equation 2.9).

Utilizing the Dy excitation scheme derived from CF parameters [14], C_{mag} of $\text{Dy}_2\text{Ir}_2\text{O}_7$ describes the anomaly centred at 240 K (Figure 4.22 a), however, the enhancement of the C_{mag} at ~ 25 K can not be explained by the crystal field excitation of the Dy ions. As the first reason for the disagreement be-

tween the data and the CF model should be considered the use of $\text{Lu}_2\text{Ir}_2\text{O}_7$ as a non-magnetic analogue. To justify the use of $\text{Lu}_2\text{Ir}_2\text{O}_7$ data, the following considerations are made: (i) the iridium magnetic contribution to specific heat is almost identical within the series, which is, to a certain degree, confirmed investigating the specific heat of the upper listed $A_2\text{Ir}_2\text{O}_7$ and (ii) the C_{el} is similar for all rare-earth analogues; the phonon contribution, dependent specially on the atomic properties of Dy and Lu ions (and related lattice differences), could be responsible for observed anomaly. Previously used $\text{Eu}_2\text{Ir}_2\text{O}_7$ data represent a better choice to obtain C_{mag} of dysprosium analogue [14, 112]. Nevertheless, comparing $\text{Eu}_2\text{Ir}_2\text{O}_7$ [8] and $\text{Lu}_2\text{Ir}_2\text{O}_7$ data, no significant difference, focusing mainly on the relevant temperature range, is observed. Considering the anomaly is intrinsic, the explanation could be found in the low-energy high-phonon density of states observed in the neutron scattering data [14]. However, further data on the energy spectrum of $\text{Dy}_2\text{Ir}_2\text{O}_7$ are essential to make a reliable decision on the proposed scenario.

4.4 Powder neutron diffraction of $\text{Tm}_2\text{Ir}_2\text{O}_7$

Anomalies in specific heat and magnetization data of $A_2\text{Ir}_2\text{O}_7$, as well as previous studies on selected members (e.g. $A_2\text{Ir}_2\text{O}_7$ with $A = \text{Nd}, \text{Eu}$ or Tb [79, 113, 16]) suggest a long-range ordering of the iridium magnetic moments. To inspect the magnetic structure in other members of $A_2\text{Ir}_2\text{O}_7$ series, namely $\text{Tm}_2\text{Ir}_2\text{O}_7$, neutron diffraction experiment was performed. Tm ion in $\text{Tm}_2\text{Ir}_2\text{O}_7$ reveals a singlet ground state (4.3.2 and Table 4.3), therefore no long-range magnetic ordering is expected for Tm sublattice. That is, only the magnetic signal of iridium sublattice is investigated. Neutron diffraction experiment on $\text{Tm}_2\text{Ir}_2\text{O}_7$ at temperatures ranging from 0.1 K to room temperature was performed employing D1B at ILL, Grenoble as described in section 2.2.

Inspecting the diffraction pattern recorded at 180 K (Figure 4.23a), well above any magnetic transition, data are described by the pyrochlore structure with the position of Bragg reflection denoted with green ticks and respective (hkl) indices. In addition to $\text{Tm}_2\text{Ir}_2\text{O}_7$, contribution of the copper holder is manifested as two labelled peaks at 74 and 89°. Signal coming from unreacted Tm_2O_3 is marked with asterisks. The volume fraction of oxide is lower than 1.5%.

During cooling, pyrochlore structure of $\text{Tm}_2\text{Ir}_2\text{O}_7$ is preserved down to 0.1 K. Development of pyrochlore lattice parameter is plotted in Figure 4.23 b). A linear decrease of a is followed down to 80 K and it tends to saturate at lower temperature. A thermal expansion of the crystal lattice can be described within a Debye model of lattice vibration. For a cubic material, a development of the lattice parameter with temperature is supposed to follow an expression [114]

$$a = a_0 (1 + I_0 T \phi(\theta_D/T)), \quad (4.7)$$

where a_0 is lattice parameter extrapolated to 0 K ($= 10.145 \text{ \AA}$) and I_0 ($1.02(6) \cdot 10^{-5}$) is proportional to the product of isothermal expansion and Gruneisen parameter. $\phi(\theta_D/T)$ represents a polynomial approximation of Debye integral and can be found in [114]. Debye temperature θ_D deduced from the fit was determined as 380(30) K, which is in good agreement with the Debye temperature calculated for $\text{Lu}_2\text{Ir}_2\text{O}_7$ from the specific heat data ($\theta_D = 350(4) \text{ K}$

in 4.2.1) and further justify the use of lutetium analogue as a good approximation of lattice contribution to specific heat.

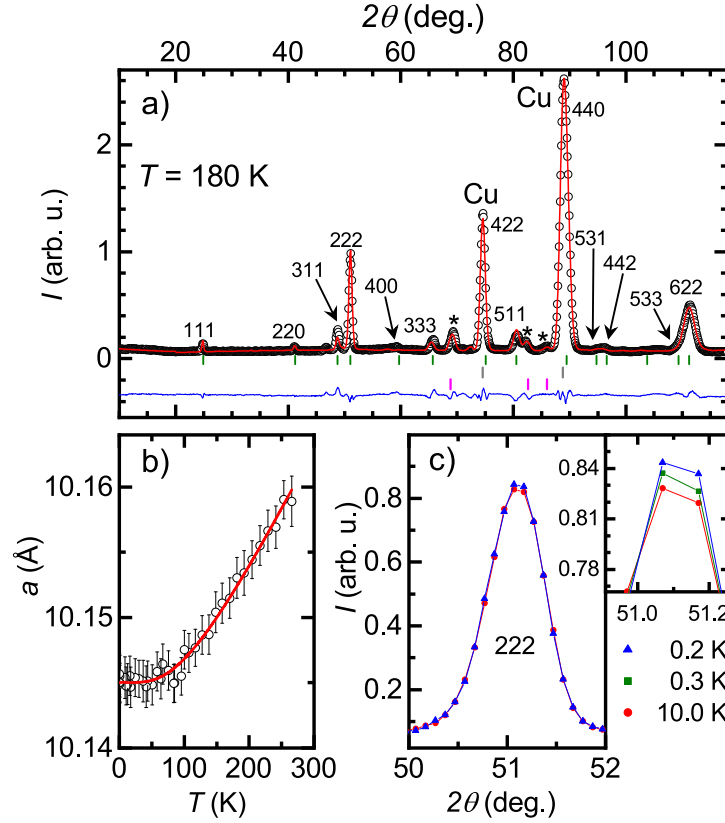


Figure 4.23. *Neutron diffraction on $\text{Tm}_2\text{Ir}_2\text{O}_7$.* a) Neutron diffraction pattern recorded at 180 K, red line stands for a fit to the pyrochlore structure, blue line represents the difference between experimental and calculated data. Positions of Bragg reflections belonging to a pyrochlore phase, copper holder and Tm_2O_3 are denoted by green, grey and pink ticks, respectively; respective peaks are marked by hkl reflections, Cu and by asterisks. Panel b) contains temperature development of the pyrochlore lattice parameter a together with a fit to Debye model of lattice expansion. c) Temperature development of 222 peak of pyrochlore structure ($Fd\bar{3}m$, 227) at 0.2 K (blue) and 10 K (red), and zoomed in detail with additional temperature 0.3 K patterns (green).

Searching for a magnetic signal below $T_{\text{Ir}} = 142$ K, no clear evidence of magnetic ordering was observed. No additional peaks outside of nuclear reflections' positions were tracked out. Focusing on a development of intensity of nuclear peaks, a subtle increase of intensity was followed on (222) reflection. This signal could be ascribed to the AIAO structure of Ir moments, similarly as previously reported for other analogues ($A = \text{Nd}$ [79], Eu [113], Tb [16], Dy [14], Yb [13] and Lu [13]). However, no additional signal was found at other peaks. (We note that no additional magnetic signal was observed in difference patterns subtracting 180 K data from lowest-temperature one.) Therefore, based on measured data, neither AIAO structure, nor any magnetic ordering of Ir sublattice in $\text{Tm}_2\text{Ir}_2\text{O}_7$ can be unambiguously acknowledged. It is worth noting that an analogous experiment of neutron diffraction on $\text{Er}_2\text{Ir}_2\text{O}_7$ was performed using instrument E6 at HZB, Berlin. Similarly to the thulium iridate, no magnetic signal

was observed down to low temperatures. Nevertheless, it is in agreement with the results published in [9].

4.5 μ SR spectroscopy of $\text{Er}_2\text{Ir}_2\text{O}_7$ and $\text{Tm}_2\text{Ir}_2\text{O}_7$

Magnetic correlations can be effectively investigated using μ SR spectroscopy, where muons implanted into the sample serve as a sensitive local probe. Muon spin rotation spectroscopy allows us to study the local magnetic environment at the implanted muon site, even without the perturbation of applying a magnetic field. The probe is sensitive to spin dynamics in the MHz regime. Oscillations in the time response of muon asymmetry are typically observed in an ordered magnetic state and result from muon precessing about the axis of a uniform internal magnetic field.

$\text{A}_2\text{Ir}_2\text{O}_7$ pyrochlores consist of two magnetic sublattices, and two muon implantation sites can be observed. μ SR experiment on $\text{Er}_2\text{Ir}_2\text{O}_7$ was conducted at a pulsed muon source at the Rutherford Appleton Laboratory (RAL, ISIS), Didcot, using the MUSR spectrometer (details of the experiment are given in section 2.8). At all temperatures, there is a strong depolarisation of the implanted muon ensemble (see Figure 4.24b); however, no oscillations in the muon spectra are observed at any temperature. Subsequently, a μ SR experiment on $\text{Er}_2\text{Ir}_2\text{O}_7$ and $\text{Tm}_2\text{Ir}_2\text{O}_7$ was performed using a continuous muon source at the Paul Scherrer Institute, Villigen, on the GPS spectrometer (see section 2.8), which enabled us to measure muon depolarisation with higher time resolution. This was necessary as the observed oscillations are highly damped and so the residual amplitude of the oscillation is almost completely wiped out by the start of the ISIS spectrometer observation window at $\sim 0.2 \mu\text{s}$.

GPS muon asymmetry data for both, $\text{Er}_2\text{Ir}_2\text{O}_7$ and $\text{Tm}_2\text{Ir}_2\text{O}_7$, reveal pronounced oscillations. The oscillations noticeably develop with temperature increasing up to 130 K, and no clear oscillations are observed above T_{tr} . The static local magnetic field at muon stopping site is indicated in both analogues. Selected data and fits of initial muon asymmetry development $A(t)$ are shown in Figures 4.24 and 4.25 for erbium and thulium iridate, respectively.

A single function was used to parameterise the $A(t)$ at all temperatures, incorporating a combination of a slow Lorentzian relaxation characterised by λ_1 and damped oscillating function with oscillating frequency ω_μ , damping λ_2 and phase factor Φ , spectrometer-dependent time invariant characteristic. A time-invariant background contribution, A_b , accounting for muons stopping within the sample holder and certain uncorrelated events also contributes to a total fit function:

$$A(t) = A_1 e^{-\lambda_1 t} + A_2 e^{-\lambda_2 t} \cos(\omega_\mu t + \Phi) + A_b, \quad (4.8)$$

which was also utilized for neodymium iridate pyrochlore [115]. In the case of $\text{Er}_2\text{Ir}_2\text{O}_7$, where both GPS and MUSR data were collected at corresponding temperatures, the fitting was performed simultaneously for both data sets. Fitting the GPS data determines the oscillating frequency and its damping, an incorporation of MUSR data helps to stabilize the slow relaxing component in function 4.8. For $\text{Tm}_2\text{Ir}_2\text{O}_7$ just GPS data were measured and therefore the slow relaxing component is connected with larger uncertainty.

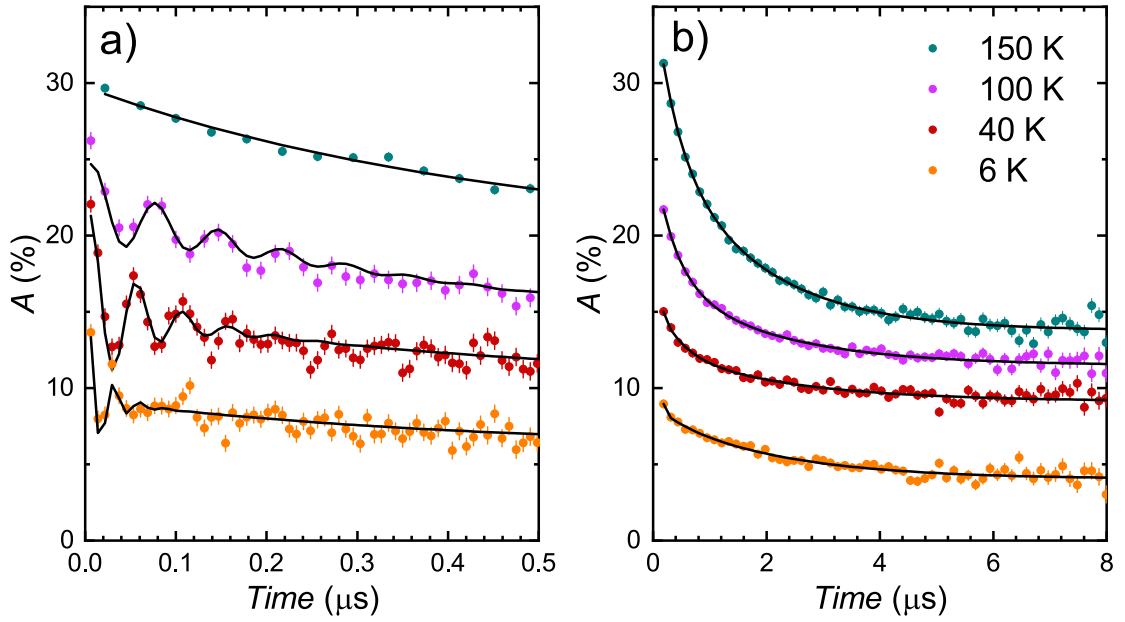


Figure 4.24. μSR spectra of $Er_2Ir_2O_7$. a) GPS and b) MUSR data at selected temperatures; solid-line represents a fit to the two-component function of muon depolarisation (equation 4.8). Data are shifted along the y-axis for better clarity.

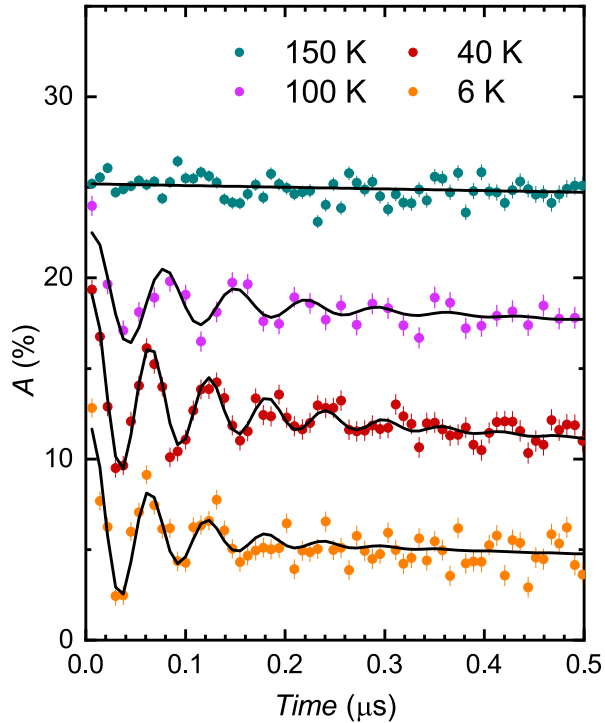


Figure 4.25. μSR spectra of $Tm_2Ir_2O_7$. GPS data below and above T_{Ir} with fits to equation 4.8 (solid black lines). Data for individual temperatures were shifted along y-axis for better quality.

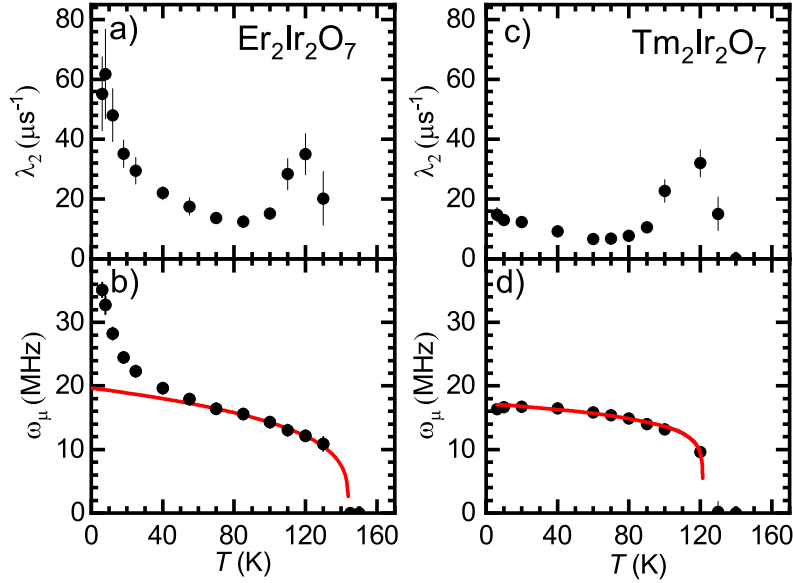


Figure 4.26. Temperature evolution of μ SR fit parameters. Temperature dependence of depolarisation rate λ_2 of oscillating component with frequency ω_μ for $\text{Er}_2\text{Ir}_2\text{O}_7$ and $\text{Tm}_2\text{Ir}_2\text{O}_7$. Red lines represent the fit to the critical behaviour as described in the text.

The temperature dependence of ω_μ for both $\text{Er}_2\text{Ir}_2\text{O}_7$ and $\text{Tm}_2\text{Ir}_2\text{O}_7$ is shown in Figure 4.26 b,d). Oscillations in asymmetry data start to appear below T_{Ir} and the frequency of oscillations increases with decreasing temperature. In the case of thulium iridate, the ω_μ development follows a critical behaviour described with $\omega_\mu \sim (1 - T/T_C)^\epsilon$ [116] (red line in Figure 4.26). The critical exponent ϵ equals to 0.14(2), which is close to the value predicted for 2D Ising spins (= 0.125 [116]). Simultaneously, the damping of oscillations characterised by λ_2 also increases with decreasing temperature (Figure 4.26a). In the case of erbium iridate, the development of oscillation damping and frequency follows thulium analogue down to ~ 70 K; however, lowering the temperature below 70 K causes a rapid increase of oscillating frequency as well as stronger damping of oscillations. This increase in oscillation frequency is a result of an increase in local field strength at the muon site, causing a shorter precession period of the muon's spin about local field direction. Using data down to 70 K, the critical exponent ϵ was determined to be 0.27(4), which exceeds the value for the thulium analogue. However, the relevance of the ϵ comparison is significantly burdened by the restricted temperature range of ω_μ fitting for the erbium analogue. For both analogues, an initial rapid increase of oscillation damping λ_2 below T_{Ir} is rather an artefact of data processing, while the oscillating component of asymmetry disappears quite fast from the signal when a temperature approaches T_{Ir} . Contrary, the low temperature enhancement of λ_2 occurring in both analogues signifies a broader distribution of local fields at muon stopping site within the spectrometer time-window, much stronger for the erbium analogue. This is not at all surprising as at low temperature the large magnetic moments of the erbium ion begin to slow into the spectrometer time-window and depolarise the implanted muons - seen as an increase in λ_2 .

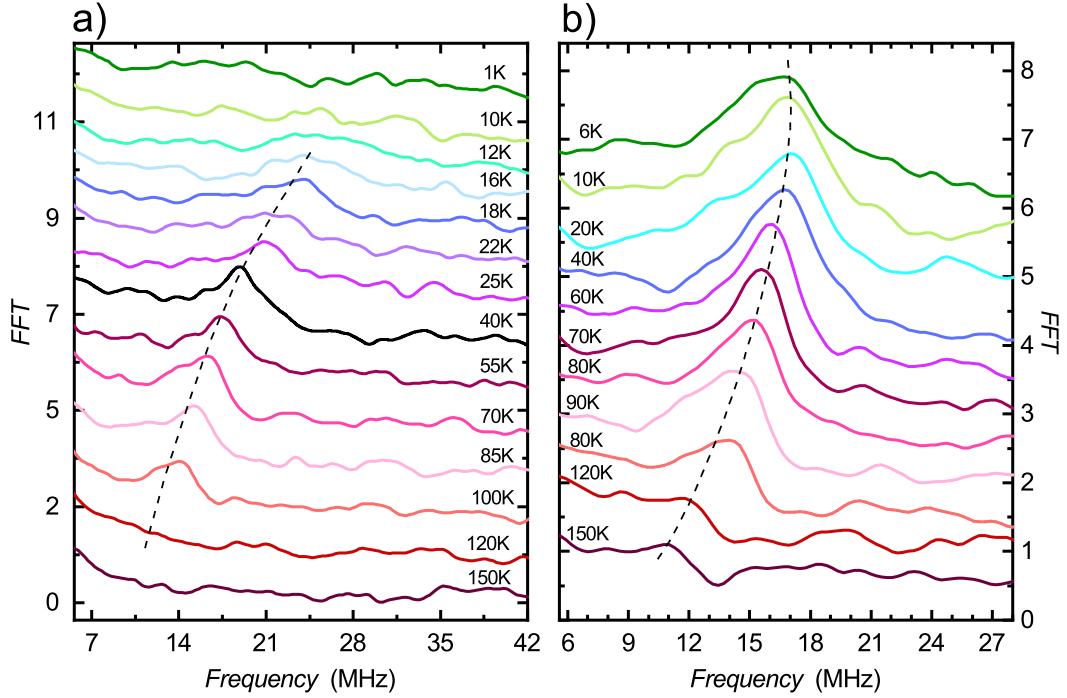


Figure 4.27. Fast Fourier transformation of $A_2Ir_2O_7$ μ SR spectra.

a) $Er_2Ir_2O_7$ and b) $Tm_2Ir_2O_7$ μ SR spectra at selected temperatures. Dashed lines follow the temperature development of peak maximum corresponding to oscillation frequency.

To further investigate the character of the muon oscillations, the fast Fourier transformation (FFT) of the asymmetry data using Mantid software [117] was performed for both $Er_2Ir_2O_7$ and $Tm_2Ir_2O_7$, as shown in Figure 4.27. Due to the significant damping of oscillations in the erbium analogue, the peaks in the FFT data corresponding to the frequency of oscillations are less pronounced than for the thulium analogue, where the damping is weaker. The shift of the FFT maxima follows the ω_μ development in Figure 4.26 b,d; in the case of $Tm_2Ir_2O_7$, the position of the maximum shifts towards higher frequencies up to ~ 70 K and tends to saturate at higher temperatures with significant broadening of the peak shape. It corresponds to the increase of oscillation damping λ_2 and expresses the increasing width of local magnetic fields acting on the muons. A stronger damping, and therefore the increase of the width of local fields distribution, in $Er_2Ir_2O_7$ is accompanied by a shift of the FFT maximum towards higher frequencies with decreasing temperature. An increase of oscillation frequency can be a consequence of the emergence of additional static magnetic field component originating from reduced dynamics of the Er sublattice, correlated with the static Ir sublattice. Such a scenario is, however, not supported by magnetization measurement and mainly by neutron diffraction, which did not reveal any sign of coherent magnetic ordering below ~ 70 K. Instead, an interaction between erbium ions and ordered iridium moments via Er^{3+} polarisation likely causes an increase of ω_μ , which was already proposed for similar observation in $Yb_2Ir_2O_7$ [10] or in $AFeAsO$ systems [118].

4.6 Dynamic response of $A_2\text{Ir}_2\text{O}_7$

4.6.1 AC magnetic susceptibility

Dynamic properties of magnetic moments are effectively studied by means of AC magnetic susceptibility. Complex dynamic magnetic response of $A_2\text{Ir}_2\text{O}_7$ consists of both A^{3+} and Ir^{4+} contributions, each of them at generally different time scales. As was mentioned in section 3, various experiments on $A_2\text{Ir}_2\text{O}_7$ indicate the possible presence of short-range correlated iridium moments coexisting with the long-range ordered state. Such a system may exhibit nontrivial dynamic properties resulting from weakly bounded moments, and the studies of the AC response are highly desirable. The measurement of $A_2\text{Ir}_2\text{O}_7$ ($A = \text{Dy}, \text{Er}, \text{Tm}$ and Yb) together with non-magnetic rare-earth analogue $\text{Lu}_2\text{Ir}_2\text{O}_7$ provides the possibility to partially separate the iridium-iridium interactions from the entanglement with rare-earth magnetism. An experimental setup of AC measurement is described in section 2.7. AC susceptibility data at selected frequencies for all investigated compounds are plotted in Figure 4.28a - e. Data in arbitrary units are normalized for better comparison.

Due to the Kramers-Kronig relations between the real and imaginary parts of AC susceptibility (see 2.26), any change of $\chi'(T)$ curvature is accompanied by a dominant maximum in $\chi''(T)$. For all $A_2\text{Ir}_2\text{O}_7$, the change from negative to positive curvature in the real part of susceptibility $\chi'(T)$ occurs at ~ 70 K for 10 kHz frequency. The temperature of the transition $T_{max}(\nu)$, which is associated with the maximum in $\chi''(T)$, strongly evolves with frequency. With decreasing frequency, a significant shift of $T_{max}(\nu)$ towards lower temperatures is observed for all oxides together with a broadening of the anomaly in $\chi''(T)$ leading to an increase of the experimental error of $T_{max}(\nu)$. Since the main feature of the $\text{Lu}_2\text{Ir}_2\text{O}_7$ AC response corresponds to the magnetic rare-earth $A_2\text{Ir}_2\text{O}_7$, the origin of the AC susceptibility maxima is supposed to be the dynamics of iridium moments.

Besides high-temperature anomalies, e.g. $T_{max} = 70$ K at 10 kHz in the case of $\text{Er}_2\text{Ir}_2\text{O}_7$, similar for all investigated pyrochlores, another anomaly at low temperatures is tracked out, see Figure 4.28. Similar anomaly is observed for Yb member. $\chi'(T)$ of these two analogues reveals a significant upturn at 10 and 6 K, respectively, which exhibit just a subtle frequency dependence. While the high temperature anomaly dominates the $\chi''(T)$, the low temperature feature is pronounced to a lower extent. $\chi'(T)$ of $\text{Lu}_2\text{Ir}_2\text{O}_7$, $\text{Tm}_2\text{Ir}_2\text{O}_7$ and $\text{Dy}_2\text{Ir}_2\text{O}_7$ remains constant below 20 K in the whole frequency range. The low-temperature enhancement of $\chi'(T)$ for $A = \text{Er}$ and Yb is therefore ascribed to the contribution of the rare-earth magnetic ground state contrary to the case of non-magnetic A analogues. The constant low-temperature $\chi'(T)$ of $\text{Dy}_2\text{Ir}_2\text{O}_7$ points to the absence of low-temperature dynamics, possibly due to the freezing of both Dy and Ir moments above ~ 20 K.

Considering a significant shift of $T_{max}(\nu)$ in the investigated frequency range (see Figure 4.29 a - d), the temperature dependence of the relaxation time τ is discussed in the frame of spin glass systems. Four generally considered models have been utilized. The frequency dependence of the freezing temperature T_{max} demonstrated as a maximum in χ''_{AC} can be used for the spin glass system char-

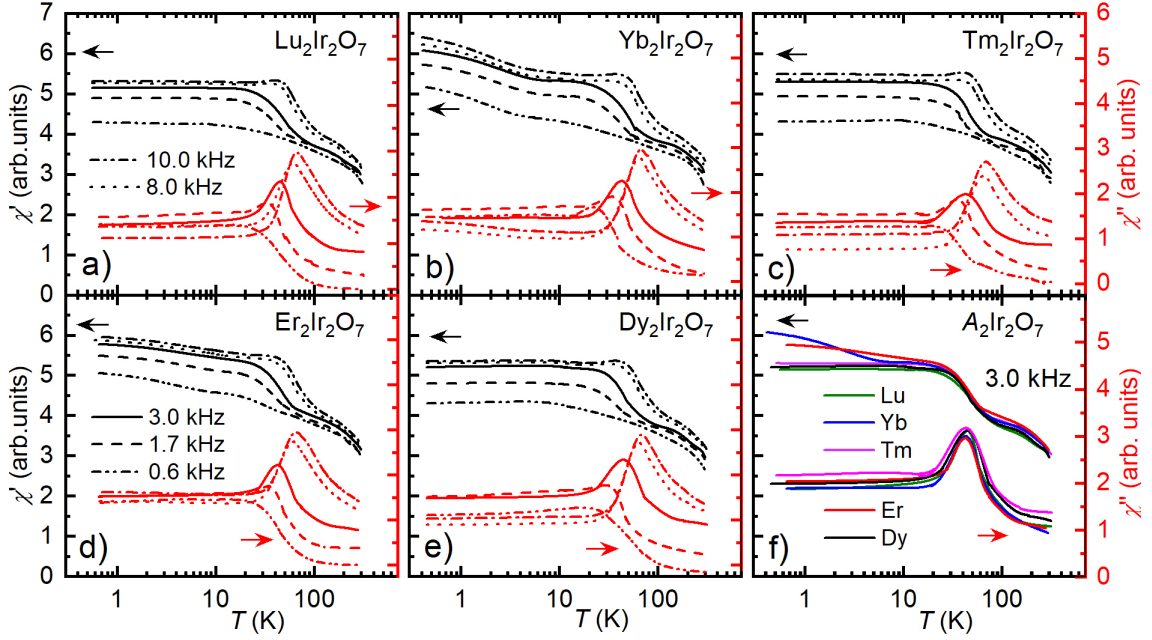


Figure 4.28. AC susceptibility of $A_2Ir_2O_7$. The representative curves of $\chi'(T)$ (black curves, left axes) and $\chi''(T)$ (red curves, right axes) part of AC susceptibility for $A_2Ir_2O_7$ iridates in the frequency range 0.6 - 10.0 kHz. Panel f) contains a comparison of $A_2Ir_2O_7$ response at 3.0 kHz.

acterisation. δT_{max} is given by the relation $\delta T_{max} = \frac{d \ln(T_{max})}{d \ln(\nu)}$; however, due to the typical small shift of T_{max} with frequency, δT_{max} can be determined as

$$\delta T_{max} = \frac{\Delta T_{max}}{T_{max} \Delta \log(\nu)}. \quad (4.9)$$

Typical spin-glass systems are characterised by δT_{max} ranging from 0.001 to 0.1 [119]. To characterise a spin glass behaviour, the $T_{max}(\nu)$ shift per decade of frequency, δT_{max} , is determined as a slope of $T_{max}(\nu)$ vs $\log(\nu)$, see Figure 4.29 a-d. Analysing the frequency dependence of T_{max} shift, similar for all of the studied $A_2Ir_2O_7$ compounds, an analogous behaviour of T_{max} is observed in the frequency interval from 3 kHz to 10 kHz. Nevertheless, the values of $T_{max}(\nu)$ are slightly lower for the lutetium iridate. The resulting values of δT_{max} were determined over two frequency ranges: 0 - 3 kHz and 3 - 10 kHz. The δT_{max} values lay between 44(2) and 59(1) in the frequency range 3 - 10 kHz, see Table 4.4. In comparison with typical spin glass systems ($\delta T_{max} = 0.005$ for CuMn [120]), insulating spin glasses ($\delta T_{max} = 0.027$ for NaSrMn₂F₇ [121]) or spin-ice materials ($\delta T_{max} = 0.18$, Dy₂Ti₂O₇, [122]), the $A_2Ir_2O_7$ values of δT_{max} are two orders of magnitude larger, suggesting a rather different character of spin correlations. Simultaneously, the δT_{max} parameter has a similar value for $A_2Ir_2O_7$ (Table 4.4) which mirrors the dominating role of Ir⁴⁺ correlations in the investigated temperature-frequency range. The linear fits of the low frequency range 0 - 3 kHz of $T_{max}(\nu)$ lead to lower values of δT_{max} lying between 5 and 17, that is, still two orders of magnitude larger than metallic or insulating spin glass materials.

The second model describes the spin system consisting of magnetic particles without mutual interactions. Such a system can be found in e.g. *superparamagnets* or *single - molecule magnet* compounds [64, 123].

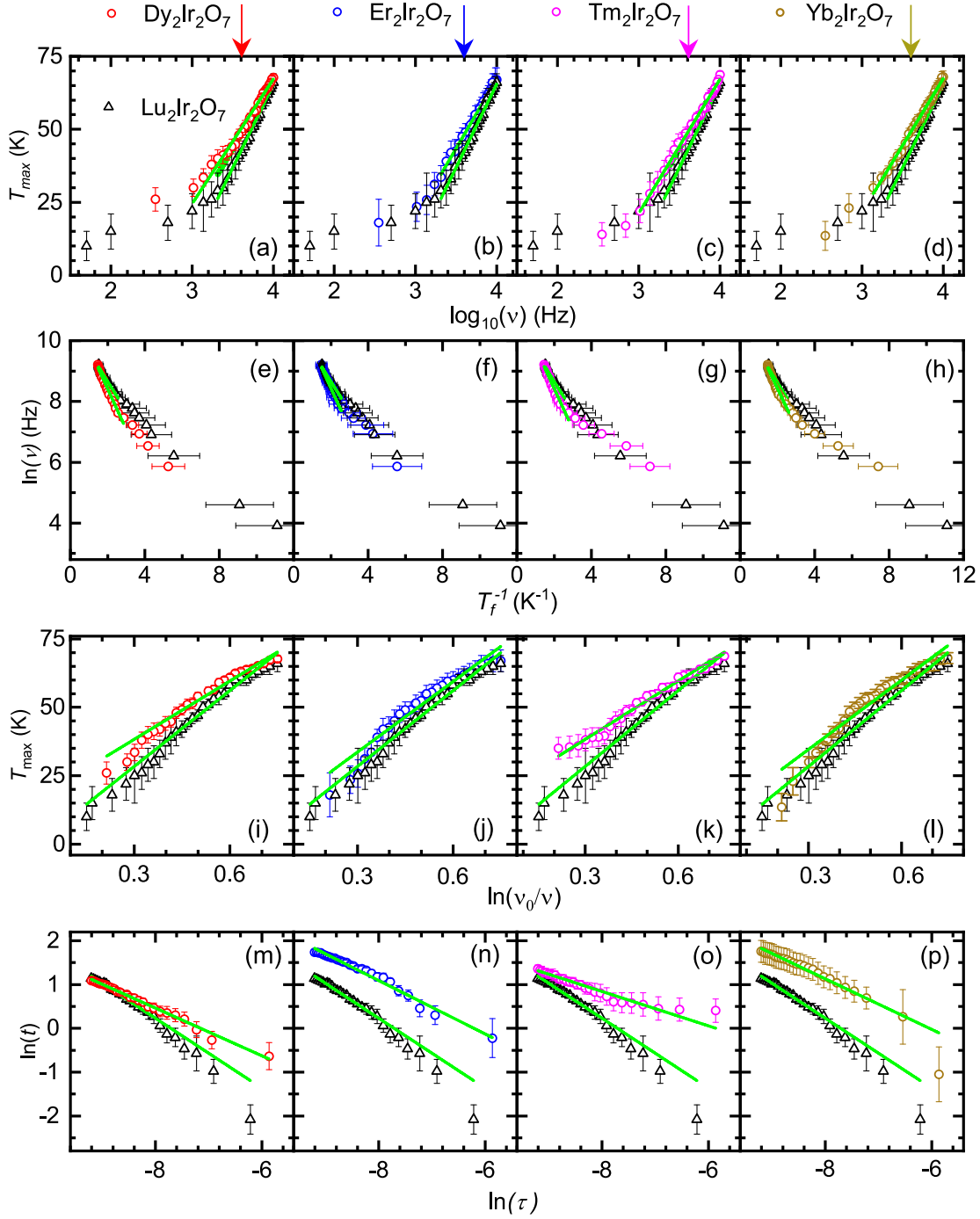


Figure 4.29. AC susceptibility anomaly viewed by spin dynamics models. Frequency dependence of the high-temperature anomaly in AC susceptibility data, T_{max} , of individual $A_2\text{Ir}_2\text{O}_7$. Red, blue, purple, and yellow circles stand for $A = \text{Dy}, \text{Er}, \text{Tm}$ and Yb . Black triangles represent the $\text{Lu}_2\text{Ir}_2\text{O}_7$ data. Green lines are fits to the frequency dependence of the freezing temperature (first row, a - d), Arrhenius law (second row, e - h), Vogel-Fulcher law (third row i - l), and power-law (fourth row m - p).

Due to the absence of magnetic interactions, the formation of magnetic domains is suppressed. The magnetic anisotropy separates the spin orientations by the energy barrier E_a , and the excitations are realized by the thermally activated spin flipping. The temperature dependence of the spin relaxation τ can be described by the Arrhenius law

$$\tau(T) = \tau_0 e^{\frac{E_a}{k_B T}}, \quad (4.10)$$

where τ_0 denotes the characteristic time for spin reversal known as *attempt time* (ranging from 10^{-11} s to hours or longer period [64]). An interacting system is described by a characteristic frequency ν_0 and activation flipping energy E_a . Measured data were fitted using a linearized form of the Arrhenius law: $\ln(\nu) = \ln(\nu_0) - \frac{E_a}{k_B} \frac{1}{T_{max}}$ (Figure 4.29 e - h). Fitting the data in 3 - 10 kHz interval, the activation energy $\frac{E_a}{k_b}$ for $A_2\text{Ir}_2\text{O}_7$ was determined to fall into the interval 82(5) - 108(5) K and characteristic frequency values $\nu_0 \sim 30$ kHz (see Table 4.4). Energies of the barriers are comparable with the temperatures of the anomalies at high frequencies. However, the intrinsic frequencies are unusually low. While the high-frequency data (3 - 10 kHz) are well fitted by Arrhenius law, T_{max} anomalies in lower frequencies deviate from a linear dependence, which could be a signature of a more complex dynamical processes occurring in the $A_2\text{Ir}_2\text{O}_7$ oxides with both magnetic and nonmagnetic rare-earth cations.

To take into account the development of correlation length as a temperature is approaching the freezing point from above, a third model of power-law scaling can be used. The frequency dependence of the relaxation time is written as [119]

$$\tau = \tau_0 \left(\frac{T_{max}(\nu) - T_g}{T_g} \right)^{-z\nu'} \quad (4.11)$$

where $z\nu'$ is a dynamical exponent of the critical slowing down. For the spin-glass systems, typical values of $z\nu'$ lie between 1 - 20 [124]. Data were fitted to its linearized form $\ln(\tau) = \ln(\tau_0) - z\nu' \ln\left(\frac{T_{max} - T_{SG}}{T_{SG}}\right)$, see Figure 4.29 m-p. The relaxation time τ is equal to ν^{-1} , the characteristic relaxation time τ_0 , freezing temperature T_{SG} as $\nu \rightarrow \infty$ and dynamical critical exponent $z\nu'$ characterise the system. For typical spin glasses, $z\nu'$ lies between 4-12 [124]. For all compounds T_{SG} was estimated to lay between 11 K and 35 K based on the extrapolation of $T_{max}(\nu)$ towards the lowest frequencies, see Table 4.4. The values of $z\nu'$ resulting from a linear fit of the power-law fall between 0.49(2) and 0.57(1) for all $A_2\text{Ir}_2\text{O}_7$. These values are an order of magnitude lower than for classical spin glasses. τ_0 ranges from 0.02 to 0.05 s (see Table 4.4), which does not fit into a classical atomic time scale (10^{-5} - 10^{-10} s).

Interactions between spins leading to their freezing can be also described using the empirical Vogler-Fulcher law originally proposed to account for an increasing viscosity of supercooled liquids when approaching the glass transition. Within a Vogel-Fulcher law, relaxation-time development is described as [125]

$$\tau = \tau_0 e^{\frac{E_a}{k_B(T-T_0)}}, \quad (4.12)$$

where E_a and τ_0 stand for the activation energy and characteristic relaxation time, a parameter reflecting the interaction between magnetic moments. To fit the data, 4.12 is modified into the linearized form: $T_{max} = \frac{E_a}{k_B} \frac{1}{\ln(\nu_0/\nu)} + T_0$, where

T_0 is the Vogel-Fulcher temperature, in atomic structural glasses called the *ideal glass* temperature and also understood as a measure of intercluster interaction and ν_0 stands for the intrinsic relaxation frequency of the system. Attempts to fit all T_0 , E_a and ν_0 parameters were performed, the results found the Vogel-Fulcher temperature to be zero. The unphysical behaviour led us to use a standard method of fixing ν_0 at physically reasonable value and perform the fit of E_a and T_0 . The value of ν_0 was selected to be equal to 40 kHz, significantly lower than typical values of metallic spin glasses (1013 Hz) or spin cluster materials (107 Hz). The choice of a higher value of ν_0 again leads to a zero value of T_0 . The activation energies reach 70(2) - 91(3) K and the Vogel-Fulcher temperatures range from 1.5 - 19 K for $A_2\text{Ir}_2\text{O}_7$ (see Table 4.4). The data reveal a significant deviation from the standard Vogel-Fulcher behaviour, see Figure 4.29 m-p, thus the scenario of interacting spin clusters can be excluded.

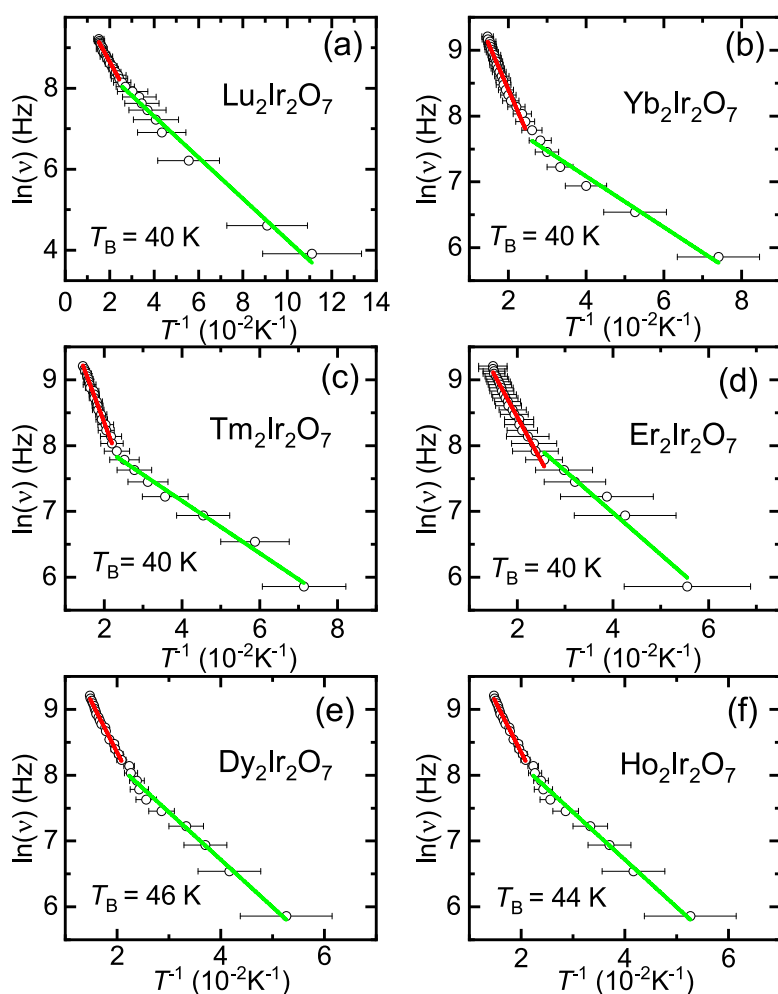


Figure 4.30. Arrhenius plots of $A_2\text{Ir}_2\text{O}_7$ AC susceptibility. Two frequency domains of $T_{max}(\nu)$ behaviour fitted by Arrhenius law at high (red line) and low-frequencies (green line) for all $A_2\text{Ir}_2\text{O}_7$.

Comparison of T_{max} with Arrhenius law and δT_{max} linear fits reveals a tendency of $T_{max}(\nu)$ to follow a linear evolution with two different slopes for high- and low-frequency regions, which are separated by the boundary at T_B . The similarity of the $A_2\text{Ir}_2\text{O}_7$ AC susceptibility development implies a comparable values of T_B

being ~ 40 K for all studied compounds, except for dysprosium analogue which T_B equals to 46(2) K (see Table 4.4). Arrhenius law was applied separately on the high- and low- frequency parts of $T_{max}(\nu)$ (red and green lines in Figure 4.30) and two respective sets of activation energies E_a^h and E_a^l were obtained (see Table 4.4). The E_a^h values of $A_2\text{Ir}_2\text{O}_7$ lay between 100 - 160 K, whereas the E_a^l falls within the interval 40 - 70 K (Table 4.4). The successful description of $T_{max}(\nu)$ behaviour considering two sets of parameters suggest that two mechanisms of spin relaxation with different flipping energies are present. Such a situation is rare, however, a similar two-slope character of spin relaxation was observed in the case of frustrated 2D organo-metallic triangular antiferromagnet with spin freezing below 2 K, where weakly bounded spins on the antiferromagnetic domain walls are responsible for the AC susceptibility response in two regimes [126].

Table 4.4. Parameters of spin glass models for $A_2\text{Ir}_2\text{O}_7$. δT_{max} stands for the shift of the maximum's temperature per decade of frequency, E_a/k_B represents the barrier energy of thermally activated behaviour typical for superparamagnets with ν_0 as a characteristic frequency of the system (Arrhenius law). T_0 is the Vogler-Fulcher temperature and E_a/k_B^* is the activation energy of the respective clusters. T_{SG} represents a spin glass temperature in the limit of short time-scale ($\nu \rightarrow \infty$), $z\nu'$ denotes the critical coefficient and τ_0 is the characteristic relaxation time in model of the critical behaviour near the spin glass transition (power-law). T_B divides the AC susceptibility response into the low- and high-frequency part characterised by the activation energies E_a^l and E_a^h

	Dy ₂ Ir ₂ O ₇	Er ₂ Ir ₂ O ₇	Tm ₂ Ir ₂ O ₇	Yb ₂ Ir ₂ O ₇	Lu ₂ Ir ₂ O ₇
$\delta T_{max}(\nu)^{0-3.2\text{kHz}}$	11(2)	12(2)	5(1)	36.670	10(2)
$\delta T_{max}(\nu)^{3.2-10\text{kHz}}$	45(2)	47(1)	44(1)	46(2)	59(2)
$E_a/k_B(\text{K})$	92(5)	82(3)	90(6)	4.54	108(3)
$\nu_0(\text{kHz})$	42.65(3)	40.13(2)	22.6(3)	143(2)	30.61(2)
$T_0(\text{K})$	17(2)	6.6(8)	19(2)	9.1(8)	1.5(5)
$E_a/k_B^*(\text{K})$	71(3)	90(3)	70(2)	84(4)	91(3)
$T_{SG}(\text{K})$	17(2)	11(1)	35(1)	12(1)	17.2(8)
$z\nu'$	0.43(1)	0.48(2)	0.46(1)	0.48(3)	0.74(1)
$\tau_0(\text{s})$	0.058(2)	0.051(1)	0.052(1)	0.058(2)	0.0031(1)
$T_B(\text{K})$	46(2)	40(2)	40(3)	40(2)	40(2)
$E_a^h/k_B(\text{K})$	156(4)	134(3)	158(4)	136(5)	100(3)
$E_a^l/k_B(\text{K})$	72(3)	64(5)	40(2)	39(3)	50(2)

A handful of iridium domain wall studies in $A_2\text{Ir}_2\text{O}_7$ were published despite considerable scientific interest in iridium based pyrochlores. The investigation of magnetic domain structure and domain wall states in $\text{Nd}_2\text{Ir}_2\text{O}_7$ revealed highly conductive domain walls in the bulk insulating state by magnetoresistance measurement [81]. The local magnetotransport performed on $\text{Eu}_2\text{Ir}_2\text{O}_7$ revealed the size of the magnetic domains $\sim 1 \mu\text{m}$ [127]; the bulk measurement under ZFC/FC

conditions confirmed the field inversion asymmetric behaviour of the isothermal magnetization emerging below AIAO Néel temperature, as well as the shift of Hall resistivities along the FC directions supporting the scenario of FM/AFM exchange bias on the domain walls [82]. The marginal attention was paid to the domain structure of the others $A_2\text{Ir}_2\text{O}_7$ compounds, namely the vertical shift of $\text{Y}_2\text{Ir}_2\text{O}_7$ isothermal magnetization below the ordering temperature, which was interpreted as a coexistence of the ferromagnetic and antiferromagnetic components [128] or as a result of free spins freezing on the magnetic domain walls [73]. Isothermal magnetization studies of $\text{Lu}_2\text{Ir}_2\text{O}_7$ [75] and $\text{Sm}_2\text{Ir}_2\text{O}_7$ [72], both reveal remanent magnetization after cooling under an applied field, which was again explained as a freezing of the spins from the domain walls.

4.6.2 Isothermal magnetization of $A_2\text{Ir}_2\text{O}_7$

Motivated by the AC susceptibility results, the scenario of domain walls with weakly correlated spins responsible for the χ_{AC} behaviour was tested by isothermal magnetization measurements above and below the temperature of iridium ordering T_{Ir} for all $A_2\text{Ir}_2\text{O}_7$ compounds. To illustrate the arrangement of domain wall spins and their flipping mechanism, the AIAO/AOAI iridium domains are shown in Figure 4.31, which was constructed based on the idea published in the publication on $\text{Eu}_2\text{Ir}_2\text{O}_7$ [82].

According to the scenario proposed in [82], the AIAO/AOAI domain wall interface produces two kinds of magnetic moments with different correlations in comparison with Ir deep inside the magnetic domain. Two iridium tetrahedra at the domain boundary consist of spin triangles parallel to the domain wall (grey arrows), which are supposed to be weakly bounded and are understood as rotatable spins. Iridium moments in the centre of domain-boundary tetrahedra (purple arrows) are ferromagnetically coupled along the external field direction, carry an uncompensated net magnetic moment and are considered as pinned spins.

Behaviour of domain wall spins under different cooling regimes, introduced in [82], will be described in the following text. After the zero-field cooling below the T_{Ir} , the distribution of magnetic domains is random and both pinned and free spins do not produce any remanent magnetization M_{sh} . During ZFC $M(H)$ measurement, an increasing external field causes the orientation of the rotatable spins in the field direction. Magnetization of pinned spins is averaged to zero because of the random distribution of domains. Decreasing the external field to zero, non-zero M_{sh} is ascribed to the rotatable spins still pointing in the direction of a previously applied field, an additional negative field H_C is needed to push the $M(H)$ to zero. Further application of the negative external field orients the rotatable spins parallel to the field direction, the isothermal magnetization curve ends at a zero field where the negative value of magnetization results from the rotatable spin oriented in the direction of the negative field.

Application of the external field during cooling influences the domain population and the initial magnetization of pinned spins. Both rotatable and pinned moments contribute to the non-zero value of remanent magnetization at 0 T, see Figure 4.31b. After the field increases up to 7 T and is lowered back to 0 T, a hysteresis is not observed, evidencing the unchanged moment's state. The value

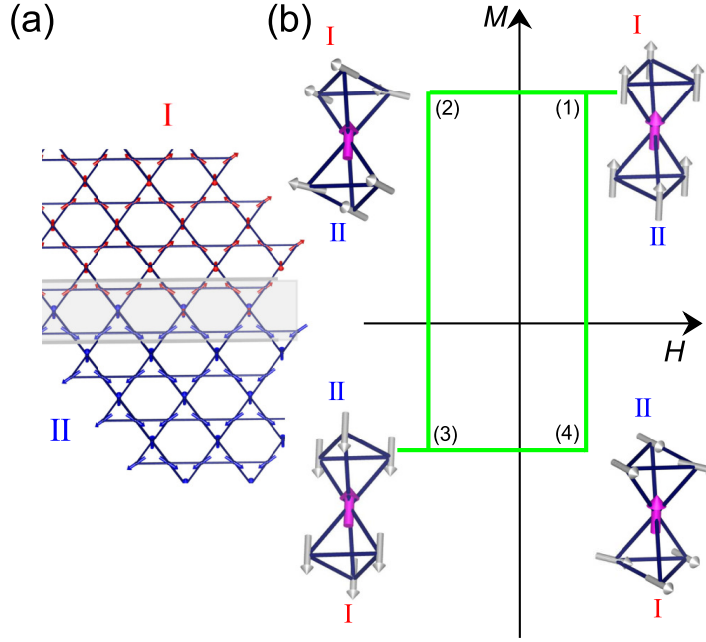


Figure 4.31. Sketch of AIAO/AOI domain walls. a) The $A_2\text{Ir}_2\text{O}_7$ iridium sublattice viewed along $\langle 111 \rangle$ direction with AIAO (red) and AOAI (blue) magnetic domains. b) Arrangement of iridium domain wall spins during the ZFC/FC $M(H)$ cycles; purple and grey arrows denote the pinned and rotatable spins, respectively. Figure was constructed based on the idea proposed for $\text{Eu}_2\text{Ir}_2\text{O}_7$ [82].

of remanent magnetization is enlarged by the pinned moments due to the preferential domain population. Furthermore, the enhanced value of the coercive field is needed to induce zero magnetization of the sample. Application of the maximal reversal field leads to the reorientation of rotatable spins; the H_C upon increasing field still persists due to the presence of pinned spins; however, it is lowered compared to the measurement with decreasing field.

The -7 T FC protocol increases the domain population oppositely to that described in the previous paragraph. Since the application of positive field preceded the application of the negative field during the $M(H)$ measurement, the remanent magnetization at field increase is lower compared to that measured at decreasing field because pinned spins preserve the orientation imposed by the negative cooling field. The zero magnetization is reached at the positive coercive field and has a lower value under the field decreasing because the rotatable spins were already reoriented under the maximum positive field of 7 T.

$A_2\text{Ir}_2\text{O}_7$ isothermal magnetization $M(H)$ was measured under three different cooling protocols, as is described in section 2.5. Representative isothermal magnetization curves of $A_2\text{Ir}_2\text{O}_7$ at 70 K are presented in Figure 4.32, where black, red and blue points represent the ZFC, 7 T FC and -7 T FC magnetization curves, respectively. The isothermal dependence of magnetization at 70 K reveals a state of iridium moments well below the magnetic ordering (~ 140 K) as well as sufficiently above the temperature of rare-earth correlations T_A introduced in preceding sections. The shift of zero-field magnetization M_{Sh} is observed for all studied compounds as well as the presence of coercive field H_C . Such an asymmet-

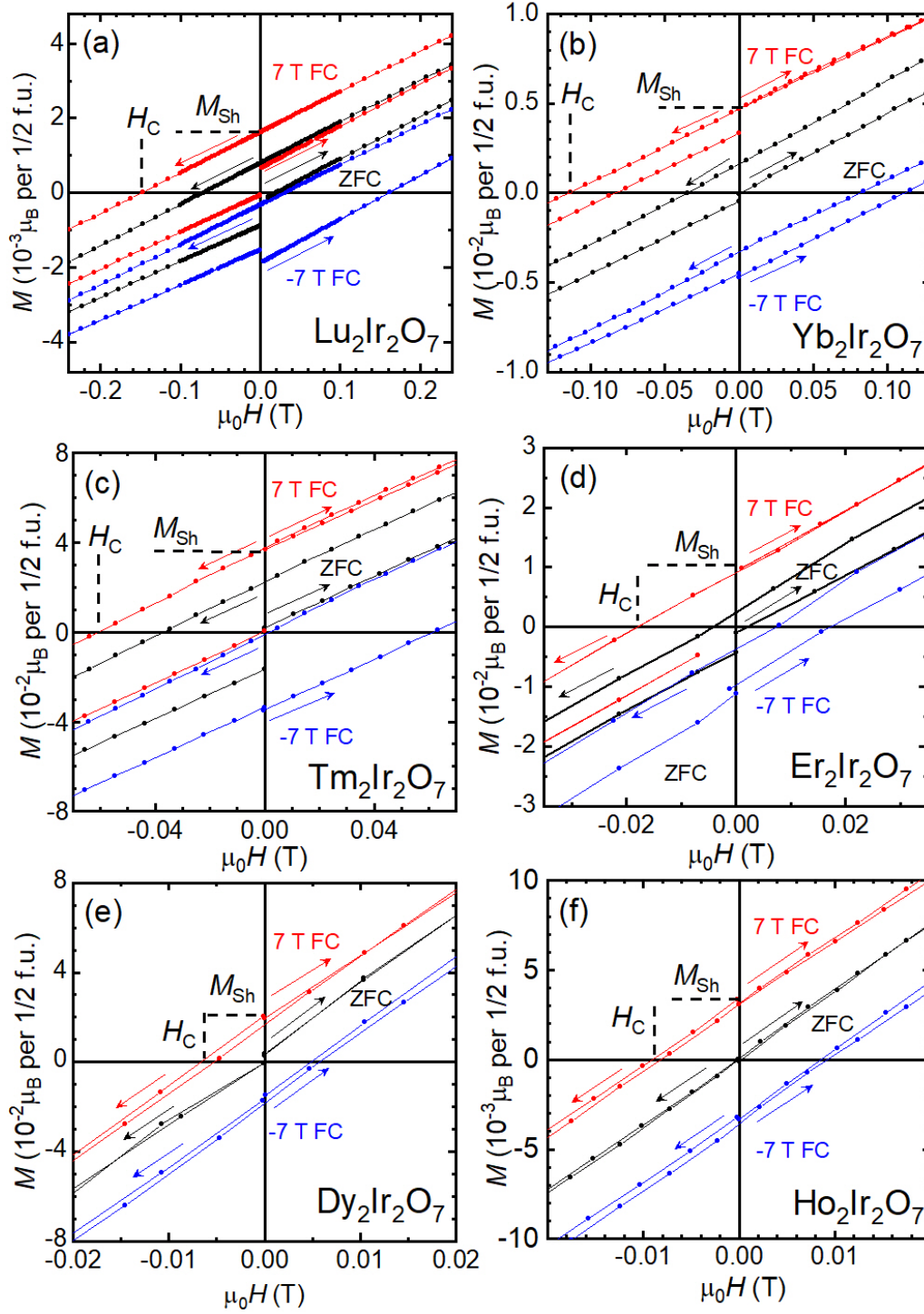


Figure 4.32. *Magnetization of $A_2\text{Ir}_2\text{O}_7$ measured under ZFC/FC regimes.* The $M(H)$ magnetization measured at 70 K under ZFC, 7 T FC and -7 T FC regimes. Respective arrows indicate the field application procedure. The vertical and horizontal dashed lines denote the M_{Sh} and H_C used for construction of Figure 4.33.

ric magnetization behaviour corresponds with the frame sketched in Figure 4.31.

Asymmetry of isothermal magnetization corresponds to the characteristics of AFM/FM exchange bias behaviour and can be described within the introduced model of domain wall spins. The similar shift of magnetization and the emergence of the coercive field suggest the presence of weakly bounded, rotatable spins for all $A_2\text{Ir}_2\text{O}_7$ ($A = \text{Dy} - \text{Lu}$) compounds; however, the development of the magnetic hysteresis differs. The cases of $\text{Dy}_2\text{Ir}_2\text{O}_7$ and $\text{Ho}_2\text{Ir}_2\text{O}_7$ show small values of $M(H)$ hysteresis in comparison with $A = \text{Lu}$, Yb , Tm and Er . Hysteresis of $M(H)$ vanishes below 40 K and above 100 K in the case of $A = \text{Yb}$, Tm and Er . The magnetization of pinned spins responsible for a magnetic hysteresis is significantly lowered for $\text{Ho}_2\text{Ir}_2\text{O}_7$ and $\text{Dy}_2\text{Ir}_2\text{O}_7$ possibly due to the entanglement with the rare-earth magnetism.

Temperature developments of the magnetization shift M_{Sh} and coercive field H_C are plotted in Figure 4.33. The non-monotonic dependence of H_C is traced for all analogues. It increases below the T_{Ir} , yielding a peak around 70 K and decreases for further decreasing temperature. The enhancement of the H_C can be a sign of the possible coupling between FM domain-wall spins and bulk AFM domains, most pronounced in lutetium analogue and well suppressed in erbium compound. The shift of magnetization M_{Sh} increases below T_{Ir} and saturates in the case of $A = \text{Dy}$, Ho and Lu . Contrary, M_{Sh} of $A = \text{Er}$, Tm and Yb compounds increases with decreasing temperature without any sign of plateau.

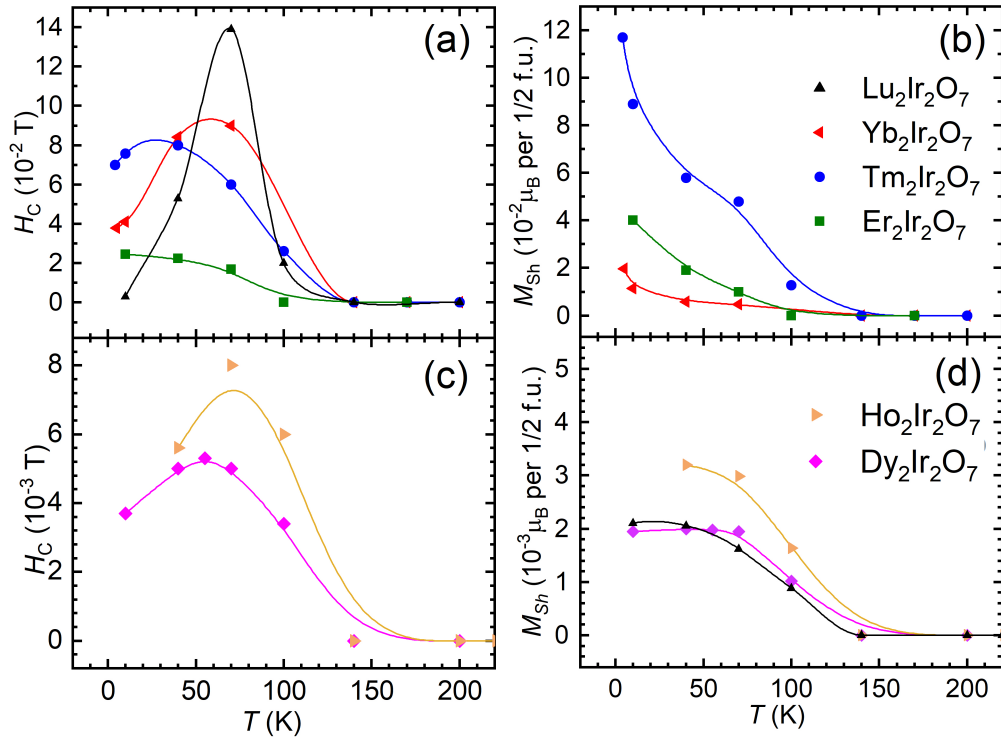


Figure 4.33. *Coercive field and remanent magnetization for $A_2\text{Ir}_2\text{O}_7$.* H_C and M_{Sh} temperature evolution for $A_2\text{Ir}_2\text{O}_7$ ($A = \text{Dy} - \text{Lu}$), lines are guide the eye.

Based on our AC and DC susceptibility measurements, the emergence of irid-

ium domain wall spins appears to be universal for light rare-earth, non-magnetic rare-earth and also magnetic heavy rare-earth $A_2\text{Ir}_2\text{O}_7$. Principally identical behaviour of AC and DC susceptibility suggests a robust character of iridium magnetism within the whole series, however, the influence of rare-earth sublattice imprints in the differences of the magnetization parameters. Since the formation of magnetic domains is also influenced by the crystallinity of the sample, the values of M_{sh} and H_C can be sample dependent (note two orders of magnitude difference of M_{sh} in the case of $\text{Y}_2\text{Ir}_2\text{O}_7$ from [128] and [73]). Our samples were prepared under identical conditions, x-ray analysis and electron scanning microscopy confirmed a comparable size of pyrochlore crystallites (see section 4.1.2). Therefore, the evaluation of $M(H)$ parameters is consistent, at least within this study. The development of iridium sublattice dynamic properties with rare-earth ions probed by AC susceptibility is also documented by the DC magnetization measurement which allows to quantify the relative amount of the iridium domain-wall dynamic and frozen spins.

5. Discussion and conclusions

A sample synthesis is a first step in the experimental investigation of material. A significant effort was dedicated to this task in the present work. Establishing a successful preparation route applicable to a specific material is a non-trivial and time-demanding task, namely in the case of $A_2\text{Ir}_2\text{O}_7$ pyrochlore iridates.

The majority of $A_2B_2O_7$ oxides are supposed to melt congruently [129] and are standardly prepared in high amount and good quality. Naturally, there are exceptions, where a synthesis must be stabilized by various chemicals to enable a growth of desired compositions [92]. Another obstacle is often the high reaction or melting temperature of A and B elements or oxides. E.g. ZrO_2 has a very high melting temperature (2988 K) and is chemically stable during heating [130]. Either a sol-gel method and co-precipitation reaction [131], or furnace enabling the use of extremely high temperature are required to prepare the desired polycrystals or even single crystals [132]. Another difficulty arises from the low vapour pressure of some of the constituent elements and oxides, preventing the synthesis under ambient conditions. The application of high pressures in a closed reaction vessel is needed to produce polycrystalline samples of $A_2B_2O_7$ with B representing Pb [133], Pt [134], V [135] or Mn [136]. Hydrothermal synthesis methods, where the reaction vessel contains an aqueous solution of starting materials and mineralizing agent also enable crystallisation of some $A_2B_2O_7$ at lower temperatures [137]. To prevent evaporation of material or components is also possible to employ a proper dissolvent as a flux, e.g., KF or CsCl [92].

Synthesis of $A_2\text{Ir}_2\text{O}_7$ oxides is significantly hindered by a high evaporation rate and low temperature of decomposition of IrO_2 oxide, in comparison with its relatively stable co-precursor A_2O_3 . In the present work, we just focused on the pyrochlore iridate synthesis from a (slightly off-) stoichiometric mixture of initial IrO_2 and A_2O_3 oxides. Although, also other preparation routes were reported; e.g. $\text{Bi}_2\text{Ir}_2\text{O}_7$ was grown from NaBiO_3 and IrCl_3 by hydrothermal synthesis [138]; we consider that of a mixing of initial oxides as the cleanest one, not potentially contaminating the final products with other elements.

The attempts to synthesize $A_2\text{Ir}_2\text{O}_7$ employing solid state reaction and molten salt flux growth methods were done (see section 4.1). The most commonly utilized solid state synthesis revealed a strong temperature development of the pyrochlore phase formation, as well as its decomposition during the process. In the case of Er analogue, the pyrochlore phase starts to be formed at 900°C , the most efficient temperature reaction is found to be 1000°C . However, also a significant portion of unreacted Er_2O_3 remains in the material as highly volatile IrO_2 oxide decomposes/evaporates. A number of attempts were performed to counter the loss of IrO_2 during the preparation process, basically adding additional oxide to the content. Eventually, by optimizing the $\text{Er}_2\text{O}_3 : \text{IrO}_2$ ratio and reaction temperature and time, we were able to synthesize almost pure $\text{Er}_2\text{Ir}_2\text{O}_7$ sample; only very few percent of Er_2O_3 remained in the product. Unfortunately, unreacted erbium oxide was not eliminated by further adding the IrO_2 , or varying temperature of the reaction. Although we consider solid state reaction as a valid route to prepare $A_2\text{Ir}_2\text{O}_7$, also reflecting previous studies [7, 8, 10, 79], we conclude that it does not lead to phase pure samples and other methods should be employed instead,

or in combination with.

To counter a high temperature of the pyrochlore phase formation with simultaneously non-negligible loss of IrO_2 , the CsCl assisted flux growth of $\text{A}_2\text{Ir}_2\text{O}_7$ was performed. Optimizing the preparation process for the specific compound is essential, especially a choice of the reaction temperature is crucial. At low temperature, a preferential formation of IrO_2 single crystals was observed. At high temperature, an additional off-stoichiometric $A\text{-Ir-O}$ phase (same crystal structure, larger lattice parameter) was formed. The formation of a pyrochlore-like phase with higher A content is consistent with conclusions on the solid state reaction, and was observed recently also in light rare-earth iridate $\text{Eu}_2\text{Ir}_2\text{O}_7$ [90]. The reaction temperature of about 800°C was found to enable preparation of phase-pure $\text{A}_2\text{Ir}_2\text{O}_7$ with $A = \text{Dy} - \text{Lu}$. We highlight a reproducibility of the preparation process; repeating the reaction in flux and intermediately regrinding the mixture/products enable preparation of not only $\text{A}_2\text{Ir}_2\text{O}_7$ with various A , but also their synthesis in relatively large volume (several grams; necessary for, e.g., neutron scattering experiments) with a high degree of homogeneity.

Synthesized samples were thoroughly characterized by x-ray diffraction, energy dispersive x-ray spectroscopy, magnetization and specific heat measurements. The content of constituent elements in the samples was confirmed to be stoichiometric in all $\text{A}_2\text{Ir}_2\text{O}_7$ (Table 4.1), although oxygen content could not be precisely determined based on EDX and XRD. The compounds were confirmed to crystallize in a pyrochlore structure, space group $Fd\bar{3}m$, n. 227 with origin 2. A development of lattice parameter a and fraction coordinate x of oxygen Wyckoff position $48f$ ($x, 1/8, 1/8$) with the atomic radius of rare-earth element is followed (Table 4.1): The lattice parameter decreases with an atomic number of A , according to expectations - lanthanide contraction of atomic/ionic radius. The change of A atom size, simultaneously, influences the oxygen interatomic distances and angles, i.e. the 8-coordinate oxygen cage around A and octagonal cage around Ir. As the other atomic coordinates are fixed by lattice symmetry (oxygen on $8b$ Wyckoff position has no free parameter.), x represents the measure of cages-distortion. The difference in x -value from ideal $3/8$ causes the cages deformation and therefore a strong anisotropy in atomic distances and, in turn, the anisotropy of electronic properties. x in $\text{A}_2\text{Ir}_2\text{O}_7$ slightly increases with atomic number of A , leading to less distorted O cages and hence weaker anisotropy in the system.

The bifurcation between zero-field cooled and field-cooled magnetization curves of $\text{A}_2\text{Ir}_2\text{O}_7$ together with a high-temperature anomaly in specific heat serves as a signature of the ordering of iridium sublattice. While the specific heat anomaly is relatively broad, ranges over approximately 30 K, the magnetization data enable relatively accurate determination of ordering temperature T_{Ir} . Synthesizing all heavy rare-earth members of the series, including previously unreported $\text{Tm}_2\text{Ir}_2\text{O}_7$, and investigating their physical properties allowed us to consistently complete the phase diagram previously reported by Matsuhira et al. [8]. T_{Ir} develops with ionic radius of A subtly. Almost linear increase of ordering temperature with increasing atomic number of A is followed (Figure 4.12). The increase of T_{Ir} can be ascribed to the shortening of interatomic distances in the material, and, in turn, to the less deformed oxygen octahedra around Ir^{4+} ions. The influence of

magnetism of the rare-earth ion on T_{Ir} seems to be negligible, at least for heavy rare-earth part of the series. A tentative conclusion can be drawn: The magnetism of A^{3+} ion for, at least, $A = \text{Sm} - \text{Lu}$ does not have a (significant) impact on the ordering of the iridium sublattice. However, vice versa, the ordering of iridium moments and connected molecular field, could have a significant impact on the rare-earth ordering. E.g., $\text{Tb}_2\text{Ir}_2\text{O}_7$ reveals the AIAO ordering below T_{Ir} of not only Ir sublattice, but also Tb sublattice [16].

Further investigating the magnetization properties of heavy $A_2\text{Ir}_2\text{O}_7$, a negative Curie-Weiss temperature was determined for all members. The value of θ_p , the lowest value for $\text{Lu}_2\text{Ir}_2\text{O}_7$ ($= -217$ K) resulting from the strong antiferromagnetic correlations between iridium moments, increases with increasing ionic radius of A (Table 4.2). Such evolution of θ_p suggests weaker antiferromagnetic correlations between rare-earth moments enlarging the lattice. Nevertheless, the situation is likely more complicated, as complex ordering/ground states were reported for these materials, e.g., fragmented states in $\text{Dy}_2\text{Ir}_2\text{O}_7$ [14] and $\text{Ho}_2\text{Ir}_2\text{O}_7$ [15], or competition of phases - ferromagnetic and AIAO induced by Ir sublattice - in $\text{Yb}_2\text{Ir}_2\text{O}_7$ [13]. The antiferromagnetic correlations are corroborated by the isothermal magnetization measurements. No signs of ferromagnetic ordering were observed in the data.

The correlations between rare-earth ions are demonstrated at low temperatures, inspecting the specific heat data. Pyrochlores with $A = \text{Dy}, \text{Er}$ and Yb , that is, those with magnetic ground state, reveal the low temperature anomaly in C_{mag} , which is attributed to the magnetic correlations between rare-earth ions with magnetic doublet as a ground state (Figure 4.15). Considering the results of the inelastic neutron scattering experiments, the CF origin of the anomalies is excluded. The magnetic entropy connected with the anomalies reach the value of $R \ln(2)$ at the anomalies onset, therefore, the Zeeman splitting of the ground state doublet stands behind the low temperature anomalies. The observed shapes of the anomalies are not consistent with the standard magnetic transition to ordered state, instead, rather an accretion of magnetic correlations is proposed. An application of the external magnetic field shifts the anomalies towards higher temperatures; not typical for simple antiferromagnetic ordering.

Other features and anomalies in magnetization and specific heat data - field-dependent magnetization change in Figure 4.13 and anomalies in the temperature evolution of the magnetic contribution to specific heat in Figure 4.22 - were described in the frame of a standard crystal field model.

Excitation spectra of $\text{Er}_2\text{Ir}_2\text{O}_7$ and $\text{Tm}_2\text{Ir}_2\text{O}_7$ were examined by inelastic neutron scattering. An estimation of the phonon part of the spectra was based on the measurement of $\text{Lu}_2\text{Ir}_2\text{O}_7$ with non-magnetic Lu^{3+} . Rare-earth ions' Wyck-off position is not cubic, which is the space symmetry of the pyrochlore lattice, but trigonal point symmetry. The ground state multiplets of Kramers' Er^{3+} ion ($J = 15/2$) and non-Kramers' Tm^{3+} ion ($J = 6$) in crystalline environment, hence, split into eight doublets, and into 5 doublet and 4 singlet states, respectively. The measured spectra were described by a model crystal field Hamiltonian; crystal field parameters are listed in Table 4.3. We highlight that the excitation scheme of $\text{Er}_2\text{Ir}_2\text{O}_7$ resembles the one of isostructural $\text{Er}_2\text{Pt}_2\text{O}_7$ [109], and is similar to other analogues with $B = \text{Ge}, \text{Ti}$ and Sn [109]. The effect of the magnetic iridium cations on the erbium CF scheme is thus rather weak. Instead, the cubic

cage of oxygens around Er determines the CF acting on it - a very similar crystallographic parameters of isostructural $B = \text{Ir}$ and Pt . Much less information on $\text{Tm}_2\text{B}_2\text{O}_7$ pyrochlores was reported. Nevertheless, the energy of the first excitation in $\text{Tm}_2\text{Ti}_2\text{O}_7$ pyrochlore ($= 10.64$ meV, [139]) matches that of thulium iridate ($= 10.6$ meV). The complete CF spectra of $\text{Tm}_2\text{B}_2\text{O}_7$ are not accessible. The influence of iridium magnetism cannot be conclusively excluded. However, one can assume that Ir magnetic sublattice plays a rather moderate role on the Er/Tm CF scheme, which is actually not surprising considering highly localized $4f$ electrons and their small overlap with Ir $5d$ orbitals. Instead, the CF acting on rare-earth ions is predominantly determined by the nearest neighbour oxygen anions.

Determined CF schemes were confronted with the magnetization and specific heat data. A local single-ion CF anisotropy dictated by the distorted oxygen cage around A Wyckoff position has a planar character - perpendicular component (\perp to tetrahedron $\langle 111 \rangle$ axes) contributes more to the systems' magnetization than the parallel component (z) for investigated analogues. As the measurements were performed on the polycrystalline samples, the magnetic susceptibility was calculated as a powder-average of the crystallographic directions. The inverse magnetic susceptibilities of $\text{Er}_2\text{Ir}_2\text{O}_7$ and $\text{Yb}_2\text{Ir}_2\text{O}_7$ in Figure 4.13 are well described by the calculations (CF parameters for ytterbium iridate were adopted from [13]). On contrary, the magnetic susceptibility of thulium iridate is reproduced down to ~ 150 K, and at lower temperature, mean field approximation fails to describe the data. Rather poor agreement of mean field $M(T)$ calculations for dysprosium iridate (CF parameters adopted from [14]) was ascribed to the Ising-like character of Dy moments which point along $\langle 111 \rangle$ local axis [14].

Mean field approximation systematically underestimates the isothermal magnetization response for all compounds (Figure 4.14). Nevertheless, it is explained by the iridium contribution which is not included in the calculations. The experimental data are, hence, sufficiently in agreement with calculations based on respective CF parameters. $\text{Tm}_2\text{Ir}_2\text{O}_7$ data, on the other hand, are described rather poorly by pure CF model. To explain the disagreement between the experiment and calculations based on the CF Hamiltonian, the presence of strong molecular field was tested. An inclusion of the molecular field in the direction of the external field was added to microscopic Hamiltonian. The average magnetization was calculated self-consistently at $T = 180$ K (purple line in Figure 4.14 c), describing the data. However, applying this approach (using the same molecular field constant) leads to a strong deviation between experiment and calculations at lower temperature. A more complicated behaviour originating from the interactions between the non-magnetic thulium ground state and staggered field of iridium moments is anticipated.

A perfect agreement between the measured magnetic contribution to specific heat and the Schottky contribution calculated from CF eigenenergies is illustrated in Figure 4.22. We note the low-temperature anomaly in C_{mag} of $\text{Dy}_2\text{Ir}_2\text{O}_7$, which is not described by CF scheme. We ascribe this anomaly to a more complex behaviour of this analogue, namely, fragmented monopole state of Dy ions [14], and possibly non-trivial interaction between dysprosium and iridium moments.

To further investigate the higher-temperature behaviour of $A_2\text{Ir}_2\text{O}_7$, connected with Ir-sublattice, we performed measurements of AC magnetic susceptibility, μSR experiment, and neutron diffraction experiment on two representatives of the series $\text{Er}_2\text{Ir}_2\text{O}_7$ and $\text{Tm}_2\text{Ir}_2\text{O}_7$.

In order to study a magnetic ordering from the microscopical point of view, the experiment of μSR was performed on erbium and thulium iridate. It revealed an appearance of spontaneous muon spin rotation below T_{Ir} which unambiguously confirms the long-range magnetic ordering of Ir^{4+} . Moreover, the development of the oscillations described by the damped oscillations pointed to the difference between erbium and thulium iridate behaviour and significant entanglement of the iridium and erbium magnetism. The observed early time oscillations are in agreement with the previous results on $A_2\text{Ir}_2\text{O}_7$ ($A = \text{Nd}, \text{Eu}, \text{Sm}, \text{Yb}$ or Y [115, 77, 76, 10]. An additional increase of oscillating frequency with decreasing temperature confirmed for erbium analogue was also detected in the case of magnetic Kramers' Nd and Yb pyrochlores which further supports the idea of iridium and rare-earth magnetism entanglement.

As the μSR experiment undoubtedly proved an emergence of the magnetic ordering below T_{Ir} for $\text{Er}_2\text{Ir}_2\text{O}_7$ and $\text{Tm}_2\text{Ir}_2\text{O}_7$, the magnetic structure of iridium sublattice was investigated by neutron diffraction. Magnetic signal in $\text{Tm}_2\text{Ir}_2\text{O}_7$ with non-magnetic Tm^{3+} ion is expected to originate solely in iridium sublattice. The experiment did not reveal any new magnetic reflections emerging below T_{Ir} outside the nuclear reflections. Only a slight increase of intensity on (222) peak with decreasing temperature was detected, in agreement with expected AIAO antiferromagnetic structure of Ir moments. The present results point to the limited sensitivity of neutron diffraction to the small magnetic moment carried by Ir^{4+} , however, does not exclude the AIAO magnetic ordering of iridium sublattice.

Moreover, the shape of the high temperature specific heat anomaly accompanying the ordering of iridium sublattice is rather broad, suggesting partial dynamic behaviour of the iridium moments. Therefore, the dynamical properties of $A_2\text{Ir}_2\text{O}_7$ were studied by means of the AC magnetic susceptibility. For all A , the AC response showed a strongly frequency dependent maxima shifting from 70 K at 10 kHz towards lower temperatures with decreasing frequency. The unusual developments of the maxima were analysed within the frame of traditional spin glass systems; however, the resulting parameters for various spin glass models are far from the physically reasonable values. Therefore, a different interpretation of the AC response is proposed [82, 126]: iridium moments form two types of antiferromagnetic domains, i.e. AIAO and AOAI. The interface between the domains contains two kinds of spins, which can be distinguished on the basis of their correlations with the spins inside the domain (Figure 4.31). The weakly bounded spins are supposed to respond to the AC magnetic field. The strongly bounded spins, which are ferromagnetically coupled with the domains, are predicted as well within the domain wall scenario.

The investigation of the magnetization under different cooling protocols revealed the presence of the two kinds of spins. The appearance of the remanent magnetization during different field-cooling cycles were confirmed for magnetic and also non-magnetic rare-earth pyrochlore iridates below T_{Ir} (see Figures 4.33). The remanent magnetization is caused by ferromagnetically coupled spins and also, after the application of external field, by the polarized free spins. The present

study of ferromagnetic/antiferromagnetic bias-like behaviour in pyrochlore iridates seems consistent within the series, however, the differences between individual compounds can be traced. Decreasing temperature below T_{Ir} , the shift of magnetization becomes more pronounced in all analogues. However, the shift of $A = \text{Dy, Ho}$ and Lu members tends to saturate at temperatures below 40 K. A weaker influence of the Dy and Ho spins is also deduced comparing their magnetization curves with non-magnetic $\text{Lu}_2\text{Ir}_2\text{O}_7$ analogue data. A similar evolutions are observed. Inspecting the development of the coercive field with temperature in individual members, a pronounced maximum is followed. It can be ascribed to the interfacial pinning of the ferromagnetic component on the domain walls boundaries [82]. Present results on polycrystalline samples are supported by recent studies on $\text{Nd}_2\text{Ir}_2\text{O}_7$ and $\text{Eu}_2\text{Ir}_2\text{O}_7$ single crystals and thin films [81, 82]. Presence of two magnetic domains and properties connected to the walls between them, hence, seem to be universal for rare-earth pyrochlore iridates.

Despite a thorough investigation of $A_2\text{Ir}_2\text{O}_7$ magnetic properties, a number of possible exotic properties remains hidden. Based on the theoretical predictions, $A_2\text{Ir}_2\text{O}_7$ are supposed to host a non-trivial electronic states [3]. Their successful evidence can be made by measurement of electron structure on single crystalline samples, synthesis of which is still lacking for a significant part of $A_2\text{Ir}_2\text{O}_7$. The CsCl flux method enables the preparation of single crystals of μm size, which is still small size for many desired techniques. Searching for a suitable flux is part of the current scientific effort including our continuing experiments. The studies of heavier rare-earth pyrochlores in their single crystalline form can also significantly expand the knowledge about unconventional behaviour of rare-earth magnetism on frustrated lattice under the influence of staggered iridium molecular field. In this direction, a number of studies are still to be done. With a contribution of present work, attractive electron properties of iridium domain walls such as its high conductivity in the insulating state [81] and possible contribution to giant magnetoresistance [6] seem to be common to the pyrochlore iridate family. Moreover, the domain wall effects and a delicate interplay between iridium and rare-earth magnetism, which is a weak effect in DC properties, can be effectively studied using weakly bounded domain wall spins and their dynamical response. A full understanding and parametrization of the rare-earth and iridium interaction based on the sensitive domain wall spin remain a future task.

Bibliography

- [1] M. A. Subramanian, G. Aravamudan and G. V. Subba Rao. Oxide pyrochlores - a review. *Prog. Solid st. Chem.*, 15(2):55–143, 1983.
- [2] M. J. Harris, S. T. Bramwell, P. C. W. Holdsworth and J. D. M. Champion. Liquid-Gas Critical Behavior in a Frustrated Pyrochlore Ferromagnet. *Phys. Rev. Lett.*, 81:4496–4499, 1998.
- [3] W. Witzak-Krempa, G. Chen, Y. B. Kim, L. Balents. Correlated quantum phenomena in the strong spin-orbit regime. *Annu. Rev. Condens. Matter Phys.*, 5(1):57–82, 2014.
- [4] F. Wilczek. Two Applications of Axion Electrodynamics. *Phys. Rev. Lett.*, 58:1799–1802, 1987.
- [5] Y. Tokiwa, J. J. Ishikawa, S. Nakatsuji and P. Gegenwart. Quantum criticality in a metallic spin liquid. *Nat. Mater.*, 13(4):356–359, 2014.
- [6] K. Matsuhira, M. Tokunaga, M. Wakeshima, Y. Hinatsu and S. Takagi. Giant magnetoresistance effect in the metal-insulator transition of pyrochlore oxide $Nd_2Ir_2O_7$. *J. Phys. Soc. Japan*, 82(2):023706, 2013.
- [7] K. Matsuhira, M. Wakeshima, R. Nakanishi, T. Yamada, A. Nakamura, W. Kawano, S. Takagi and Y. Hinatsu. Metal-insulator transition in pyrochlore iridates $Ln_2Ir_2O_7$ ($Ln = Nd, Sm, \text{ and } Eu$). *J. Phys. Soc. Japan*, 76(4):043706, 2007.
- [8] K. Matsuhira, M. Wakeshima, Y. Hinatsu and S. Takagi. Metal-Insulator Transitions in Pyrochlore Oxides $Ln_2Ir_2O_7$. *J. Phys. Soc. Japan*, 80(9):094701, 2011.
- [9] E. Lefrancois, V. Simonet, R. Ballou, E. Lhotel, A. Hadj-Azzem, S. Kodjikijan, P. Lejay, P. Manuel, D. Khalyavin and L. Chapon. Anisotropy-Tuned Magnetic Order in Pyrochlore Iridates. *Phys. Rev. Lett.*, 114:2427202, 2015.
- [10] S. M. Disseler, Ch. Dhital, A. Amato, S. R. Giblin, C. de la Cruz, S. D. Wilson and M. J. Graf. Magnetic order in the pyrochlore iridates $A_2Ir_2O_7$ ($A = Y, Yb$). *Phys. Rev. B*, 86:014428, 2012.
- [11] S. Nakatsuji, Y. Machida, Y. Maeno, T. Tayama, T. Sakakibara, J. van Duijn, L. Balicas, J. N. Millican, R. T. Macaluso and J. Y. Chan. Metallic Spin-Liquid Behavior of the Geometrically Frustrated Kondo Lattice $Pr_2Ir_2O_7$. *Phys. Rev. Lett.*, 96:087204, 2006.
- [12] A. B. Sushkov, J. B. Hofmann, G. S. Jenkins, J. Ishikawa, S. Nakatsuji, S. Das Sarma and H. D. Drew. Optical evidence for a Weyl semimetal in pyrochlore $Eu_2Ir_2O_7$. *Phys. Rev. B*, 92:241108, 2015.
- [13] H. Jacobsen, C. D. Dashwood, E. Lhotel, D. Khalyavin, P. Manuel, R. Stewart, D. Prabhakaran, D. F. McMorrow and A. T. Boothroyd. Strong

- quantum fluctuations from competition between magnetic phases in a pyrochlore iridate. *Phys. Rev. B*, 101:104404, 2020.
- [14] V. Cathelin, E. Lefrancois, J. Robert, P. C. Guruciaga, C. Paulsen, D. Prabhakaran, P. Lejay, F. Damay, J. Ollivier, B. Fak, L. C. Chapon, R. Ballou, V. Simonet, P. C. W. Holdsworth and E. Lhotel. Fragmented monopole crystal, dimer entropy and Coulomb interactions in $Dy_2Ir_2O_7$. *Phys. Rev. Res.*, 2:032073(R), 2020.
- [15] E. Lefrancois, V. Cathelin, E. Lhotel, J. Robert, P. Lejay, C. V. Colin, B. Canals, F. Damay, J. Ollivier, B. Fak, L. C. Chapon, R. Ballou and V. Simonet. Fragmentation in spin ice from magnetic charge injection. *Nat. Comm.*, 8(209):1–6, 2017.
- [16] H. Guo, C. Ritter and A. C. Komarek. Magnetic structure of $Tb_2Ir_2O_7$ determined by powder neutron diffraction. *Phys. Rev. B*, 96:144415, 2017.
- [17] H. Haken and H. Ch. Wolf. *Atomic and quantum physics*. Springer-Verlag Berlin Heidelberg, 1984.
- [18] J. Klíma and B. Velický. *Kvantova mechanika II*. Karolinum, 2018.
- [19] A. Abragam and B. Bleaney. *Electron paramagnetic resonance of transition ions*. Clarendon press - Oxford, 1970.
- [20] S. J. Moon, H. Jin, K. W. Kim, W. S. Choi, Y. S. Lee, J. Yu, G. Cao, A. Sumi, H. Funakubo, C. Bernard and T. W. Noh. Dimensionality-Controlled Insulator-Metal Transition and Correlated Metallic State in 5d Transition Metal Oxides $Sr_{n+1}Ir_nO_{3n+1}$ ($n = 1, 2, \text{ and } \infty$). *Phys. Rev. Lett.*, 101:226402, 2014.
- [21] B. J. Kim, S. J. Moon, J.-Y. Kim, B.-G. Park, C. S. Leem, J. Ju, T. W. Noh, C. Kim, S. -J. Oh, J. -H. Park, V. Durairaj, G. Cao and E. Rotenberg. Novel $J_{eff}=1/2$ Mott State Induced by Relativistic Spin-Orbit Coupling in Sr_2IrO_4 . *Phys. Rev. Lett.*, 101:076402, 2008.
- [22] J. M. Ziman. *The physics of metals*. Cambridge University Press, 1969.
- [23] K. Ogasawara, S. Watanabe, Y. Sakai, H. Toyoshima, T. Ishii, M. G. Brik and I. Tanaka. Calculations of complete $4f^n$ and $4f^{n-1}5d^1$ energy level schemes of free trivalent rare-earth ions. *Jpn. J. Appl. Phys.*, 43(5A):L611–L613, 2004.
- [24] G. H. Wannier. Antiferromagnetism. The Triangular Ising Net. *Phys. Rev.*, 79(2):357, 1950.
- [25] K. H. J. Buschow. *Handbook on Magnetic Materials*, volume 13. 2001.
- [26] A. P. Ramirez. Strongly Geometrically Frustrated Magnets. *Ann. Rev. Matt. Sci.*, 24(1):453–480, 1994.
- [27] S. T. Bramwell and M. J. P. Gingras. Spin ice state in frustrated magnetic pyrochlore materials. *Science*, 294(5546):1495–1501, 2001.

- [28] L. Pauling. The structure and entropy of ice and of other crystals with some randomness of atomic arrangement. *J. Am. Chem. Soc.*, 57(12):2680–2684, 1935.
- [29] A. P. Ramirez, A. Hayashi, R. J. Cava, R. Siddharthan and B. S. Shastry. Zero-point entropy in 'spin ice'. *Nature*, 399(6734):333–335, 1999.
- [30] S. T. Bramwell, M. J. Harris, B. C. den Hertog, M. J. P. Gingras, J. S. Gardner, D. F. McMorrow, A. R. Wildes, A. L. Cornelius, J. D. Champion, R. G. Melko and T. Fennell. Spin Correlations in $Ho_2Ti_2O_7$: A Dipolar Spin Ice System. *Phy. Rev. Lett.*, 87:047205, 2001.
- [31] L. Savary and L. Balents. Quantum Spin liquids: a review. *Rep. Prog. Phys.*, 80(1):016502, 2017.
- [32] P. W. Anderson. Resonating valence bonds: A new kind of insulator? *Mat. Res. Bull.*, 8(2):153–160, 1973.
- [33] C. Castelnovo, R. Moessner and S. L. Sondhi. Magnetic monopoles in spin ice. *Nature*, 451:42–45, 2008.
- [34] M. J. P. Gingras and P. A. McClarty. Quantum spin ice: a search for gapless quantum spin liquids in pyrochlore magnets. *Rep. Prog. Phys.*, 77:056501, 2014.
- [35] E. Belin-Ferre. *Basics of Thermodynamics and Phase Transitions in Complex Intermetallics*. World Scientific Publishing, 2008.
- [36] F. Bassani, G. L. Liedl and P. Wyder. Phases and Phase Equilibrium. In *Encyclopedia of Condensed Matter Physics*, pages 263–272. Academic, Oxford, 2005.
- [37] C. Sun and D. Xue. Crystallization: A phase Transition Process Driving by Chemical Potential Decrease. *J. Cryst. Growth*, 470:27–32, 2017.
- [38] J. W. Gibbs. *On the Equilibrium of Heterogeneous Substances*. Number 2. Academy, 1874.
- [39] H. Schmalzried. *Solid state reactions*. Springer, Boston, MA, 1976.
- [40] R. Merkle and J. Maier. On the Tammann-Rule. *Z. Anorg. Allg. Chem.*, 631:1163–1166, 2005.
- [41] S. L. Kang, J. Park, S. Ko and H. Lee. Solid-State Conversion of Single Crystals: The Principle and the State-of-the-Art. *J. Am. Ceram. Soc.*, 98:347–360, 2014.
- [42] H. J. Scheel and T. Fukuda. *Crystal growth technology*. John Wiley and Sons Ltd, The Atrium, Southern Gate, Chichester, 2003.
- [43] R. Roy. Acceleration the Kinetics of Low-temperature Inorganic Syntheses. *J. Solid State Chem.*, 111:11–17, 1994.

- [44] A. Rabenau. The role of hydrothermal synthesis in preparative chemistry. *Angew. Chem. Int. Engl.*, 24:1026–2040, 1985.
- [45] G. Dhanaraj, K. Byrappa, V. Prasa and M. Dudley. *Springer Handbook of Crystal Growth*. Number 1. Springer-Verlag Berlin Heidelberg, 2010.
- [46] R. A. Laudise and J. W. Nielsen. Hydrothermal crystal growth. *Solid State Phys.*, 12:149–222, 1961.
- [47] D. E. Sands. *Introduction to Crystallography*. Dover Publications, 1975.
- [48] A. T. Boothroyd. *Principles of Neutron Scattering from Condensed Matter*. Oxford University Press, 2020.
- [49] D. L. Bish and J. E. Post. *Modern powder diffraction*. De Gruyter, 1989.
- [50] R. Carvajal. Recent advances in magnetic structure determination by neutron powder diffraction + FullProf. *Physica B: Condensed Matter*, 192:55–56, 1993.
- [51] R. Egerton. *Physical principles of electron microscopy*. Springer, 2008.
- [52] B. J. Inkson. *Materials characterization using nondestructive evaluation (NDE) methods*. Elsevier Science and Technology, 2016.
- [53] Bruker Nano GmbH. Bruker quantax eds user manual. <http://emc.missouri.edu/wp-content/uploads/2016/01/Bruker-Quantax-EDS-User-Manual.pdf>, 2015.
- [54] B. M. Askerov and M. Cankurtaran. Isobaric Specific Heat and Thermal Expansion of Solids in the Debye Approximation. *Phys. Stat. Sol*, 185:341–348, 1994.
- [55] N. W. Ashcroft and N. D. Mermin. *Solid State Physics*. Cengage Learning, 2011.
- [56] *Physical Property Measurement System: Heat Capacity Option User’s Manual*. 11 edition, 2004.
- [57] A. Wipf. *Mean Field Approximation*. In: *Statistical Approach to Quantum Field Theory*. Springer, Berlin, Heilderberg, 2013.
- [58] Quantum design. Magnetic Property Measurement System: MPMS7 User’s Manual. [https://mmrc.caltech.edu/MPMS/Manuals/QD\\$%\\$20HWD\\$%\\$20Ref.pdf](https://mmrc.caltech.edu/MPMS/Manuals/QD$%$20HWD$%$20Ref.pdf), 2004.
- [59] J. Clarke. The use of superconducting junctions in magnetometry. *Rev. de Phys. Appl.*, (5):32–36, 1970.
- [60] C. Patrignani. Review of Particle Physics. *Chinese Phys. C*, 2016.
- [61] F. S. Varley. Neutron Scattering Length and Cross-sections. *Neutron News*, 3(3):29–37, 1992.

- [62] K. H. Andersen. Resolution function of time-of-flight spectrometer MARI. *Nucl. Instrum. Methods. Phys. Res. A*, 371:472–479, 1996.
- [63] J. Taylor, O. Arnold, J. Bilheaux, A. Buts, S. Campbell, M. Doucet, N. Draper and R. Fowler. Mantid, A high performance framework for reduction and analysis of neutron scattering data. *Bulletin of the American Physical Society*, 57(1):, 2012.
- [64] D. Gatteschi, R. Sessoli and J. Villain. *Molecular nanomagnets*. Oxford University Press, 2006.
- [65] J. Ziman, F. Bassani and G. Caglioti. *Theory of Condensed Matter*, 1968.
- [66] A. Yaounac and P. Dalmas de Reotier. *Muon Spin Rotation, Relaxation, and Resonance: Applications to Condensed Matter*. Oxford, 2011.
- [67] P. J. Baker, A. D. Hillier, J. S. Lord and S. R. Giblin. MuSR Manual. https://www.isis.stfc.ac.uk/Pages/musr_manual.pdf, 2011.
- [68] D. J. S. Findlay. ISIS — Pulsed Neutron and Muon Source. *Proceedings of PAC07, IEEE*, pages 695–699, 2007.
- [69] A. Amato, H. Luetkens, K. Sedlak, A. Stoykov and R. Scheuermann. The new versatile general purpose surface-muon instrument (GPS) based on silicon photomultipliers for μ SR measurements on a continuous-wave beam. *Rev. Scient. Instr.*, 88:1–10, 2017.
- [70] F. X. Zhang, M. Lang and R. C. Ewign. Atomic disorder in $Gd_2Zr_2O_7$ pyrochlore. *Appl. Phys. Lett.*, 106:191902, 2015.
- [71] V. V. Popov, A. P. Menushenkov, A. A. Yaroslavtsev, Y. V. Zubavichus, B. R. Gayanov, A. A. Yastrebtsev, D. S. Leshchev and R. V. Chernikov. Fluorite-pyrochlore phase transition in nanostructured $Ln_2Hf_2O_7$ (Ln=La-Lu). *J. Alloys. Compd.*, 689:669–679, 2016.
- [72] N. Taira, M. Wakeshima and Y. Hinatsu. Magnetic properties of iridium pyrochlores $R_2Ir_2O_7$ (R = Y, Sm, Eu and Lu). *J. Phys.: Condens. Matter*, 13(23):5527–5533, 2001.
- [73] M. C. Shapiro, S. C. Riggs, M. B. Stone, C. R. de la Cruz, S. Chi, A. A. Podlesnyak and I. R. Fisher. Structure and magnetic properties of the pyrochlore iridate $Y_2Ir_2O_7$. *Phys. Rev. B*, 85:214434, 2012.
- [74] M. Z. Hasan and C. L. Kane. Colloquium: Topological insulators. *Rev. Mod. Phys.*, 82:3045–3067, 2010.
- [75] W. C. Yang, W. K. Zhu, H. D. Zhou, L. Ling, E. S. Choi, M. Lee, Y. Losovyj, Ch. Lu and S. X. Zhang. Robust pinning of magnetic moments in pyrochlore iridates. *Phys. Rev. B*, 96:094437, 2017.
- [76] R. Asih, A. Noraina, S. S. Mohd-Tajudin, K. Matsuhira, H. Guo, M. Wakeshima, Y. Hinatsu, T. Nakano, Y. Nouze, S. Sulaiman, M. I. Mohamed-Ibrahim, P. K. Biswas and I. Watanabe. Magnetic moments

- and ordered states in pyrochlore iridates $Nd_2Ir_2O_7$ and $Sm_2Ir_2O_7$ studied by muon-spin relaxation. *J. Phys. Soc. Japan*, 86(2):024705, 2017.
- [77] S. Zhao, J. M. Mackie, D. E. MacLaughlin, O. O. Bernal, J. J. Ishikawa, Y. Ohta and S. Nakatsuji. Magnetic transition, long-range order, and moment fluctuations in the pyrochlore iridate $Eu_2Ir_2O_7$. *Phys. Rev. B*, 83:180402, 2011.
- [78] S. M. Disseler. Direct evidence for the all-in/all-out magnetic structure in the pyrochlore iridates from muon spin relaxation. *Phys. Rev. B*, 89:140413, 2014.
- [79] H. Guo, C. Ritter and A. C. Komarek. Direct determination of the spin structure of $Nd_2Ir_2O_7$ by means of neutron diffraction. *Phys. Rev. B*, 94:161102, 2016.
- [80] Y. Yamaji and M. Imada. Metallic interface emerging at magnetic domain wall of antiferromagnetic insulator: Fate of extinct Weyl electrons. *Phys. Rev. X*, 4:021035, 2014.
- [81] E. Y. Ma, Y-T. Cui, K. Ueda, S. Tang, K. Chen, N. Tamura, P. M. Wu, J. Fujioka, Y. Tokura and Z-X. Shen. Mobile metallic domain walls in an all-in-all-out magnetic insulator. *Science*, 350:538–541, 2015.
- [82] L. Xy, G. Gong, Ch. Zhao, X. Song, S. Yuan and Z. Tian. Asymmetric magnetization reversal behaviors driven by exchange coupling between all-in-all-out magnetic domains and domain walls in a $Eu_2Ir_2O_7$ single crystal. *J. Phys. Chem. C*, 124(41):22656–22662, 2020.
- [83] K. Vlášková, R. H. Colman and M. Klicpera. Synthesis of $Er_2Ir_2O_7$ pyrochlore iridate by solid-state-reaction and CsCl flux method. *Mater. Chem. Phys.*, 258:123868, 2021.
- [84] M. Klicpera, K. Vlášková and M. Diviš. Characterization and magnetic properties of heavy rare-earth $A_2Ir_2O_7$ pyrochlore iridates, the case of $Tm_2Ir_2O_7$. *J. Phys. Chem. C*, 124:20367–20376, 2020.
- [85] L. Fan, Y. Xie and X. Y. Shu. Fabrication of Pyrochlore $Gd_2Zr_2O_7$ by High Temperature Solid State Reaction. *Adv. Mat. Res.*, 1061:87–90, 2015.
- [86] N. P. Raju and E. Gemlin. Magnetic specific heat and spin-glass-like ordering in the pyrochlores: $RE_2Mo_2O_7$ (RE=Y, Sm, Gd, Ho). *J. Therm. Anal.*, 40:341–347, 1993.
- [87] Y. C. Zhou and M. N. Rahaman. Hydrothermal synthesis and sintering of ultrafine CeO_2 powders. *J. Mater. Res.*, 8:1680–1686, 1993.
- [88] H. Jehn and R. Volker. Iridium Losses During Oxidation. *Platinum Metals Rev.*, 22:321–339, 1978.
- [89] D. R. Lide. *CRC handbook of chemistry and physics*, volume 85. CRC press, 2004.

- [90] P. Telang, K. Mishra, A. K. Sood and S. Singh. Dilute stuffing in the pyrochlore iridate $Eu_2Ir_2O_7$. *Phys. Rev. B*, 97:013022, 2018.
- [91] R. J. Aldus, T. Fennel, P. P. Deen, E. Ressouche, G. C. Lau, R. J. Cava and S. T. Bramwell. Ice Rule Correlations in Stuffed Spin Ice. *New J. Phys.*, 15:013022, 2013.
- [92] J. N. Millican, R. T. Macaluso, S. Nakatsuji, Y. Machida, Y. Maeno and J. Y. Chan. Crystal growth and structure of $R_2Ir_2O_7$ ($R = Pr, Eu$). *Mater. Res. Bull.*, 42:928–934, 2007.
- [93] M. Klicpera, K. Vlášková and M. Diviš. Low-temperature properties of pyrochlore $Lu_2Ir_2O_7$. *J. Magn. Magn. Mater.*, 506(166793):1–6, 2020.
- [94] K. Vlášková, P. Proschek, M. Diviš, D. Le, R. H. Colman and M. Klicpera. Magnetic properties and crystal field splitting of the rare-earth pyrochlore $Er_2Ir_2O_7$. *Phys. Rev. B*, 102:054428, 2020.
- [95] K. Vlášková, M. Diviš and M. Klicpera. The magnetic behaviour of $Dy_2Ir_2O_7$ – beyond the mean field approximation. *J. Magn. Magn. Mater.*, 538:168220, 2021.
- [96] K. Blacklock and H. W. White. Specific heats of the pyrochlore compounds $Eu_2Ir_2O_7$ and $Lu_2Ir_2O_7$. *J. Chem. Phys.*, 72:2191–2193, 1980.
- [97] K. Koepernik and H. Eschrig. Full-potential nonorthogonal local-orbital minimum-basis band-structure scheme. *Phys. Rev. B*, 59:1743–1757, 1999.
- [98] K. Schwarz, P. Blaha and G. K. H. Madsen. Electronic structure calculations of solids using the WIEN2k package for material sciences. *Comp. Phys. Comm.*, 147:71–76, 2002.
- [99] J. P. Perdew and Y. Wang. Accurate and simple analytic representation of the electron-gas correlation energy. *Phys. Rev. B*, 45:13244–13249, 1992.
- [100] J. P. Perdew, A. Ruzsinszky, G. I. Csonka, O. Vydrov, G. E. Scuseria, L. A. Constantin, X. Zhou and K. Burke. Restoring the Density-Gradient Expansion for Exchange in Solids and Surfaces. *Phys. Rev. Lett.*, 100:136406, 2008.
- [101] Z. Wu and R. E. Cohen. More accurate generalized gradient approximation for solids. *Phys. Rev. B*, 73:235116, 2006.
- [102] J. Zhao, L. Yang, Y. Yu, F. Li, R. Yu and Ch. Jin. Structural and Physical Properties of the 6M $BaIrO_3$: A New Metallic Iridate Synthesized under High Pressure. *Inorg. Chem.*, 48:4290–4294, 2009.
- [103] G. Cao, J. Bolivar, S. McCall, J. E. Crow and R. P. Guertin. Weak ferromagnetism, metal-to-nonmetal transition, and negative differential resistivity in single-crystal Sr_2IrO_4 . *Phys. Rev. B*, 57:R11039–R11042, 1998.

- [104] G. Cao, Y. Xin, C. S. Alexander, J. E. Crow, P. Schlottmann, M. K. Crawford, R. L. Harlow and W. Marshall. Anomalous magnetic and transport behavior in the magnetic insulator $Sr_3Ir_2O_7$. *Phys. Rev. B*, 66:214412, 2002.
- [105] Q. Zhao, C. C. Stoumpos, T. H. Han, H. Li and J. F. Mitchell. New Insulating Antiferromagnetic Quaternary Iridates $MLa_{10}Ir_4O_{24}$ ($M = Sr, Ba$). *Scient. Rep.*, 5:1–8, 2015.
- [106] D. Yanagishima and Y. Maeno. Metal-nonmetal changeover in pyrochlore iridates. *J. Phys. Soc. Japan*, 70:2880–2883, 2001.
- [107] A. J. Freeman and J. P. Desclaux. Dirac-Fock studies of some electronic properties of rare-earth ions. *J. Magn. Magn. Mater.*, 12:11–21, 1979.
- [108] E. Lefrancois. Synthesis and study of iridium oxide compounds for entangled spin-orbit physics. https://www.ill.eu/fileadmin/user_upload/ILL/1_About_ILL/List_of_PhD_thesis/These_Lefrancois_E.pdf, 2006.
- [109] J. Gaudet, A. M. Hallas, A. I. Kolesnikov and B. D. Gaulin. Effect of chemical pressure on the crystal electric field states of erbium pyrochlore magnets. *Phys. Rev. B*, 97(024415):1–11, 2018.
- [110] K. A. McEwen, U. Steigenberger and J. Jensen. Spin waves, phonons, and crystal-field excitations in thulium. *Phys. Rev. B*, 43:3298–3310, 1991.
- [111] G. J. Bowden, D. P. Bunbury and M. A. H. McCausland. Crystal fields and magnetic anisotropy in the molecular field approximation. I : General considerations. *J. Phys. C: Solid St. Phys*, 4(13):1840–1854, 1971.
- [112] K. Matsuhira, M. Wakeshima, Y. Hinatsu and Ch. Sekine. Slow dynamics of Dy pyrochlore oxides $Dy_2Sn_2O_7$ and $Dy_2Ir_2O_7$. *J. Phys. Conf. Ser.*, 320(012050):1–7, 2011.
- [113] H. Sagayama, D. Uematsu, T. Arime, K. Sugimoto and E. O. Farrell. Determination of long-range all-in-all-out ordering of Ir^{4+} moments in a pyrochlore iridate $Eu_2Ir_2O_7$ by resonant x-ray diffraction. *Phys. Rev. B*, 87(100403(R)):1–4, 2013.
- [114] F. Sayetat, P. Fertey and M. Kessler. An easy method for the determination of Debye temperature from thermal expansion analyses. *J. Appl. Cryst.*, 31:121 – 127, 1998.
- [115] H. Guo, K. Matsuhira, I. Kawasaki, M. Wakeshima, Y. Hinatsu, I. Watanabe and Zhu-an Xu. Magnetic order in the pyrochlore iridate $Nd_2Ir_2O_7$ probed by muon spin relaxation. *Phys. Rev. B*, 88(060411(R)):1–5, 2013.
- [116] C. Domb. *The Critical Point: A Historical Introduction To The Modern Theory Of Critical Phenomena*. CRC Press, 1996.

- [117] O. Arnold, J. C. Bilheux, J. M. Borreguero, A. Buts, S. I. Campbell, L. Chapon, M. Doucet, N. Draper, R. Ferraz Leal, M. A. Gigg, V. E. Lynch, A. Markvardsen, D. J. Mikkelson, R. L. Mikkelson, R. Miller, K. Palmen, P. Parker, G. Passos, T. G. Perring, P. F. Peterson, S. Ren, M. A. Reuter, A. T. Savici, J. W. Taylor, R. J. Taylor, R. Tolchenov, W. Zhou and J. Zikovsky. Mantid-Data analysis and visualization package for neutron scattering and mSR experiments. *Nuclear Instruments and Methods in Physics Research Section A: Accelerators, Spectrometers, Detectors and Associated Equipment*, 764:156–166, 2014.
- [118] H. Maeter, H. Luetkens, Yu. G. Pashkevich, A. Kwadrin, R. Khasanov, A. Amato, A. A. Gusev, K. V. Lamonova, D. A. Chervinskii, R. Klingeler, C. Hess, G. Behr, B. Büchner, and H.-H. Klauss. Interplay of rare earth and iron magnetism in RFeAsO (R=La, Ce, Pr, and Sm): Muon-spin relaxation study and symmetry analysis. *Phys. Rev. B*, 80, 2009.
- [119] K. Binder and A. P. Young. Spin glasses: Experimental facts, theoretical concepts and open questions. *Rev. Mod. Phys.*, 58:801–976, 1986.
- [120] C. A. M. Mulder, A. J. Van Duynveldt and J. A. Mydosh. Susceptibility of the CuMn spin-glass: frequency and field dependences. *Phys. Rev. B*, 23, 1981.
- [121] M. B. Sanders, J. W. Krizan, K. W. Plumb, T. M. McQueen and R. J. Cava. $NaSrMn_2F_7$, $NaCaFe_2F_7$, and $NaSrFe_2F_7$: novel single crystal pyrochlore antiferromagnets. *J. Phys. Condens. Matter*, 29:045801, 2017.
- [122] J. Synder, J. S. Slusky, R. J. Cava and P. Schiffer. How spin ice freezes. *Nature*, 413:48–51, 2001.
- [123] S. J. Blundell and F. L. Pratt. TOPICAL REVIEW: Organic and molecular magnets. *J. Phys. Condens. Matter*, 16(24):R771–R828, 2004.
- [124] J. A. Mydosh. Spin-glasses : An experimental introduction. 1993.
- [125] M. Balanda. AC susceptibiliy Studies of Phase Transitions and Magnteic Relaxation: Conventional, Molecular and Low-Dimensional Magnets. *Acta Phys. Pol.*, 124, 2013.
- [126] E. Lhotel, V. Simonet, J. Ortloff, B. Canals, C. Paulsen, E. Suard, T. Hansen, D. J. Price, P. T. Wood, A. K. Powell and R. Ballou. Domain-Wall Spin Dynamics in Kagome Antiferromagnets. *Phys. Rev. Lett.*, 107:257205, 2011.
- [127] T. C. Fujita, M. Uchida, Y. Kozuka, S. Ogawa, A. Tsukazaki, T. Arima and M. Kawasaki. All-in-all-out magnetic domain size in pyrochlore iridate thin films as probed by local magnetotransport. *Appl. Phys. Lett.*, 108:022402, 2016.
- [128] H. Liu, W. Tong, L. Ling, S. Zhang, R. Zhang, L. Zhang, L. Pi, Ch. Zhang and Y. Zhang. Magnetic order, spin dynamics and transport properties of the pyrochlore iridate $Y_2Ir_2O_7$. *Solid State Commun.*, 179:1–5, 2014.

- [129] A. V. Radha and A. Navrotsky. Thermochemistry of lanthanum zirconate pyrochlore. *J. Mater. Res.*, 24:3350 – 3357, 2009.
- [130] J. Sun, Z. Hu, J. Li, H. Zhang and C. Sun. Thermal and mechanical properties of fibrous zirconia ceramics with ultra-high porosity. *Ceram. Int.*, 8:11784–93, 2014.
- [131] J. Torres-Rodriguez, V. Gutierrez-Cano, M. Menelaou, J. Kastyl, J. Cihlar, S. Tkachenko, J. A. Gonzáles, J. Kalmár, I. Fabián, I. Lázár, L. Čelko and J. Kaiser. Rare-earth zirconate $Ln_2Zr_2O_7$ (Ln : La, Nd, Gd and Dy) powders, xerogels, and aerogels: preparation, structure, and properties. *Inorg. Chem.*, 58:14467 – 14477, 2019.
- [132] K. Vlášková, R. H. Colman, P. Proschek, J. Čapek and M. Klicpera. Evidence for spin-glass ground-state in defect-fluorite $Er_2Zr_2O_7$ single crystals. *Phys. Rev. B*, 100(214405):1–9, 2019.
- [133] A. M. Hallas, A. M. Arevalo-Lopez, A. Z. Sharma, T. Munsie, J. P. Attfield, C. R. Wiebe and G. M. Luke. Magnetic frustration in lead pyrochlores. *Phys. Rev. B*, 91:104417, 2015.
- [134] H. Hoekstra and F. Gallagher. Synthesis of some pyrochlore-type oxides of platinum (IV) at high pressure. *Inorg. Chem.*, 7, 1968.
- [135] A. A. Haghighirad, F. Ritter and W. Assmus. Crystal growth of $A_2V_2O_7$ ($A = Y, Er$ and Dy) pyrochlores using high pressure. *Cryst. Growth Des.*, 8:1961 – 1965, 2008.
- [136] Y. Shimakawa, Y. Kubo, N. Hamada, J. D. Jorgensen, Z. Hu, S. Short, M. Nohara and H. Takagi. Crystal structure, magnetic and transport properties and electronic band structure of $A_2Mn_2O_7$ ($A = Y, In, Lu$ and Tl). *Phys. Rev. B*, 52:1249 – 1254, 1999.
- [137] W. Peng, B. Hu, C. Yan, W. W. Hu, L. Guo, H. M. Yuan and S. Feng. Hydrothermal synthesis and characterization of pyrochlore titanate $R_2Ti_2O_7$ ($R = Gd, Tb$ and Dy). *Chem. Res. Chinese Univ.*, 27:161 – 165, 2011.
- [138] K. Sardar, S. C. Ball, D. B. Sharman, D. Thompsett, J. M. Fisher, R. A. P. Smith, P. K. Biswas, M. R. Lees, R. J. Kashtiban, J. Sloan and R. I. Walton. Bismuth iridium oxide oxygen evolution catalyst from hydrothermal synthesis. *Chem. Mater.*, 24:4192 – 4200, 2012.
- [139] M. P. Zinkin, M. J. Harris, Z. Tun, R. A. Cowley and B. M. Wanklyn. Lifting of the ground-state degeneracy by crystal-field interactions in the pyrochlore $Tm_2Ti_2O_7$. *J. Phys. Condens. Matt.*, 8:193 – 197, 1996.

List of Figures

1.1	Generic phase diagram of electron states in $A_2\text{Ir}_2\text{O}_7$	7
1.2	Splitting of electron energy levels in $4f$ and $5d$ compounds.	9
1.3	Arrangement of magnetic moments on pyrochlore lattice.	11
3.1	Crystal structure of $A_2\text{Ir}_2\text{O}_7$ compounds.	29
4.1	Synthesis of $\text{Er}_2\text{Ir}_2\text{O}_7$ by solid state reaction.	34
4.2	Analysis of diffraction pattern peaks of $\text{Er}_2\text{Ir}_2\text{O}_7$	36
4.3	Solid state reaction with excess of IrO_2	37
4.4	Diffraction peaks of $\text{Er}_2\text{Ir}_2\text{O}_7$ prepared with excess of IrO_2	38
4.5	$\text{Er}_2\text{Ir}_2\text{O}_7$ prepared by CsCl flux.	40
4.6	Products of $\text{Er}_2\text{Ir}_2\text{O}_7$ CsCl flux growth.	41
4.7	$\text{Er}_2\text{Ir}_2\text{O}_7$ CsCl flux growth at 800°C	42
4.8	X-ray diffraction patterns of $A_2\text{Ir}_2\text{O}_7$ prepared by CsCl flux.	43
4.9	Temperature dependence of magnetization of $\text{Lu}_2\text{Ir}_2\text{O}_7$	47
4.10	Specific heat of $\text{Lu}_2\text{Ir}_2\text{O}_7$	48
4.11	Magnetization and specific heat of $A_2\text{Ir}_2\text{O}_7$	50
4.12	T_{Ir} in $A_2\text{Ir}_2\text{O}_7$ dependent on ionic radius of A^{3+}	51
4.13	Inverse magnetic susceptibility of $A_2\text{Ir}_2\text{O}_7$	52
4.14	Isothermal magnetization of $A_2\text{Ir}_2\text{O}_7$	53
4.15	Low temperature specific heat of $A_2\text{Ir}_2\text{O}_7$	57
4.16	Magnetic and lattice excitations in $\text{Er}_2\text{Ir}_2\text{O}_7$	59
4.17	Low-energy CF excitations in $\text{Er}_2\text{Ir}_2\text{O}_7$	60
4.18	Temperature development of CF excitations in $\text{Er}_2\text{Ir}_2\text{O}_7$	61
4.19	CF Hamiltonian fits to magnetic excitations of $\text{Er}_2\text{Ir}_2\text{O}_7$	62
4.20	Magnetic and phonon excitations in $\text{Tm}_2\text{Ir}_2\text{O}_7$ and $\text{Lu}_2\text{Ir}_2\text{O}_7$	64
4.21	CF Hamiltonian fits to magnetic excitations in $\text{Tm}_2\text{Ir}_2\text{O}_7$	65
4.22	Schottky specific heat in $A_2\text{Ir}_2\text{O}_7$	69
4.23	Neutron diffraction on $\text{Tm}_2\text{Ir}_2\text{O}_7$	71
4.24	μSR spectra of $\text{Er}_2\text{Ir}_2\text{O}_7$	73
4.25	μSR spectra of $\text{Tm}_2\text{Ir}_2\text{O}_7$	73
4.26	Temperature evolution of μSR fit parameters.	74
4.27	Fast Fourier transformation of $A_2\text{Ir}_2\text{O}_7$ μSR spectra.	75
4.28	AC susceptibility of $A_2\text{Ir}_2\text{O}_7$	77
4.29	AC susceptibility anomaly viewed by spin dynamics models.	78
4.30	Arrhenius plots of $A_2\text{Ir}_2\text{O}_7$ AC susceptibility.	80
4.31	Sketch of AIAO/AOAI domain walls.	83
4.32	Magnetization of $A_2\text{Ir}_2\text{O}_7$ measured under ZFC/FC regimes.	84
4.33	Coercive field and remanent magnetization for $A_2\text{Ir}_2\text{O}_7$	85

List of Tables

4.1	Structural parameters and stoichiometry of $A_2\text{Ir}_2\text{O}_7$	43
4.2	Magnetic properties of $A_2\text{Ir}_2\text{O}_7$	56
4.3	CF parameters of $A_2\text{Ir}_2\text{O}_7$	66
4.4	Parameters of spin glass models for $A_2\text{Ir}_2\text{O}_7$	81

Symbols and Abbreviations

α	isobaric thermal expansivity
β	coefficient of low-temperature phonon specific heat ($= \frac{1944.3}{\Theta_D}$)
γ	Sommerfeld coefficient of electron specific heat
ϵ	critical coefficient for μ SR oscillation
κ	isothermal compressibility
λ	wavelength
λ'	molecular field constant
λ_i	depolarisation rates of muons
Λ	strength of spin-orbit coupling
μ_0	vacuum permeability
μ_{7T}	magnetic moment at lowest temperature at 7 T
μ_B	Bohr magneton
μ_{eff}	effective magnetic moment
μ_i	chemical potential
$\hat{\boldsymbol{\mu}}_l$	operator of orbital magnetic momentum
$\hat{\boldsymbol{\mu}}_s$	operator of spin magnetic momentum
ν	frequency of AC susceptibility response
σ	neutron cross-section
Ω	solid angle
ω_μ	frequency of muon spin rotation
τ	relaxation time
τ_μ	muon lifetime
θ_B	Bragg angle
Θ_p	paramagnetic Curie temperature
Θ_D	Debye temperature
Θ_{CW}	Curie-Weiss temperature
χ'	real part of AC susceptibility
χ''	imaginary part of AC susceptibility

a	lattice parameter
\mathbf{a}^*	reciprocal lattice vector
A	rare-earth ion
AIAO	all-in-all-out magnetic ordering
b	neutron scattering length
\mathbf{B}	magnetic field induction
$B_J(x)$	Brillouin function
B_l^m	crystal field parameters
c	speed of light in vacuum
c	molar concentration
$c_{i\sigma}^+, c_{j\sigma}$	creation and annihilation fermionic operators
C	Curie constant
C_{el}	electron specific heat
C_{mag}	magnetic specific heat
C_{ph}	phonon specific heat
C_p	isobaric specific heat
C_V	izochoric specific heat
CF	crystal field
d_{hkl}	distance between (hkl) planes
e	charge of electron
e^{-2W}	Debye-Waller factor
EDX	energy dispersive x-ray analyser
E_i	energy level
F	Helmholtz free energy
f_j	x-ray atomic scattering factor
F_{hkl}	Structure factor
\mathbf{G}	reciprocal vector
G	Gibbs free energy
g_0	gyromagnetic ratio of electron
H	intensity of external magnetic field
H_C	coercive field
J	total angular momentum
J_{eff}	effective momentum
k_B	Boltzmann constant
\mathbf{l}	orbital momentum of electron
\mathbf{L}	total orbital momentum

m_e	electron mass
m_l	orbital quantum number
m_s	spin quantum number
m_n	neutron mass
M	magnetization
M_{sh}	shift of magnetization
N_F, N_B	number of events on forward and backward detectors
N_A	Avogadro's constant
n	order of diffraction
\hat{O}_l^m	Steven's operators
$P(t)$	muon depolarization function
Q	scattering angle
r	radial vector
R	universal gas constant
r_0	classical radius of electron
\mathbf{s}	spin momentum of electron
\mathbf{S}	total spin momentum
$S(T)$	entropy
$S(Q, \omega)$	neutron scattering function
$S_{mag}(Q, \omega)$	magnetic neutron scattering function
SOC	Spin-orbit coupling
T_A	temperature of M/H variation
T_B	temperature of changing activation energy
t_{ij}	hopping integral
T_{Ir}	temperature of iridium ordering
T_{max}	temperature of maxima in χ''
T_{LT}	temperature of low-temperature magnetic anomaly
U	Hubbard repulsion
U_B	energy of magnetic moment in magnetic field
$V(r)$	radial electrostatic potential
Z	atomic number

List of publications

The results presented in this thesis have been published in peer reviewed journals cited below:

M. Klicpera, K. Vlášková, M. Diviš
Characterisation and magnetic properties of heavy rare-earth $A_2\text{Ir}_2\text{O}_7$ pyrochlore iridates, the case of $\text{Tm}_2\text{Ir}_2\text{O}_7$
J. Phys. Chem. C, 124, 20367 - 20376, 2021
doi:10.1021/acs.jpcc.0c04847

K. Vlášková, M. Diviš, M. Klicpera
The magnetic behaviour of $\text{Dy}_2\text{Ir}_2\text{O}_7$ - beyond the mean-field approximation
J. Magn. Magn. Mat., 538, 168220, 2021
doi:10.1016/j.jmmm.2021.168220

M. Klicpera, K. Vlášková, R. H. Colman, P. Proschek, A. Hoser
Spin-Glass State in Defect-Fluorite $\text{Er}_2\text{Zr}_2\text{O}_7$
Act. Phys. Pol., 137, 5, 2020
doi:10.12693/APhysPolA.137.750

K. Vlášková, P. Proschek, J. Pospíšil, M. Klicpera
Low-temperature study of an $\text{Er}_2\text{Ti}_2\text{O}_7$ single crystal synthesized by floating zone technique and simplified feed rod preparation route
J. Cryst. Growth, 546, 125783, 2020
doi:10.1016/j.jcrysgro.2020.125783

K. Vlášková, B. Vondráčková, S. Daniš, M. Klicpera
High Temperature study on $\text{Er}_2\text{Ti}_2\text{O}_7$ Single Crystal
Act. Phys. Pol., 137, 5, 2020
doi:10.12693/APhysPolA.137.753

K. Vlášková, R. H. Colman, M. Klicpera
Synthesis of $\text{Er}_2\text{Ir}_2\text{O}_7$ pyrochlore iridate by solid-state-reaction and CsCl flux method
Mat. Chem. Phys., 258, 123868, 2021
doi:10.1016/j.matchemphys.2020.123868

M. Klicpera, K. Vlášková, M. Diviš
Low-temperature properties of pyrochlore $\text{Lu}_2\text{Ir}_2\text{O}_7$
J. Magn. Magn. Mat., 506, 166793, 2020
doi:10.1016/j.jmmm.2020.166793

K. Vlášková, P. Proschek, M. Diviš, D. Le, R. H. Colman, M. Klicpera
Magnetic properties and crystal field splitting of the rare-earth pyrochlore $\text{Er}_2\text{Ir}_2\text{O}_7$
Phys. Rev. B, 102, 054428, 2020
doi:10.1103/PhysRevB.102.054428

K. Vlášková, R. H. Colman, P. Proschek, J. Čapek, M. Klicpera
Evidence for spin-glass ground state in fluorite-defect $\text{Er}_2\text{Zr}_2\text{O}_7$ single crystals
Phys. Rev. B, 100, 214405, 2019
doi:10.1103/PhysRevB.100.214405